Polarimetric SAR for the monitoring of agricultural crops

Lucio Mascolo

Università degli Studi di Cagliari

Dipartimento di Ingegneria Elettrica ed Elettronica

A thesis submitted for the degree of

PhilosophiæDoctor (PhD) in Electronic and Computer Engineering

Curriculum ING-INF/02

Advisor: Prof. Giuseppe Mazzarella

PhD Course Coordinator: Prof. Fabio Roli

Final exam academic year 2013–2014

Università degli Studi di Cagliari
Dipartimento di Ingegneria Elettrica ed Elettronica

Polarimetric SAR for the monitoring of agricultural crops

Lucio Mascolo

A thesis submitted for the degree of
PhilosophiæDoctor (PhD)
in
Electronic and Computer Engineering
Curriculum ING-INF/02

Advisor
Prof. Giuseppe Mazzarella

PhD Course Coordinator
Prof. Fabio Roli

Università degli Studi di Cagliari, Cagliari, Italy

Abstract

The monitoring of agricultural crops is a matter of great importance. Remote sensing has been unanimously recognized as one of the most important techniques for agricultural crops monitoring. Within the framework of active remote sensing, the capabilities of the Synthetic Aperture Radar (SAR) to provide fine spatial resolution and a wide area coverage, both in day and night time and almost under all weather conditions, make it a key tool for agricultural applications, including the monitoring and the estimation of phenological stages of crops. The monitoring of crop phenology is fundamental for the planning and the triggering of cultivation practices, since they require timely information about the crop conditions along the cultivation cycle. Due to the sensitivity of polarization of microwaves to crop structure and dielectric properties of the canopy, which in turn depend on the crop type, retrieval of phenology of agricultural crops by means of polarimetric SAR measurements is a promising application of this technology, especially after the launch of a number of polarimetric satellite sensors.

In this thesis C-band polarimetric SAR measurements are used to estimate phenological stages of agricultural crops. The behavior of polarimetric SAR observables at different growth stages is analyzed and then estimation procedures, aimed at the retrieval of such stages, are defined.

The second topic on which this thesis is focused on is the land cover types discrimination by means of X-band multi-polarization SAR data.

Contents

List of Figures

LIST OF FIGURES

LIST OF FIGURES

List of Tables

LIST OF TABLES

1

Introduction

Agricultural crops are among the most important sources of food for terrestrial living species. As a consequence, their monitoring, which includes the monitoring of their growth stages, discrimination among various crop types and crop yield estimation, turns out to be fundamental. Monitoring growth stages of crop and observing their conditions is of primary importance since it allows farmers to properly trigger the cultivation practice during the growing season. Distinguishing among different crop types, and hence crop discrimination, allows mapping the boundaries of the parcels in order to identify agriculture land-uses and quantify the extent of each cultivated crop. The estimation of crop yield is also an important matter, since information on potential crop yield at an early stage is a great benefit for farmers, but also for countries that mainly rely on agricultural production

On these purposes, the use of remote sensing is essential. Within this framework, the capabilities of the Synthetic Aperture Radar (SAR) to provide fine spatial resolution and a wide area coverage, both in day and night time and almost under all weather conditions, make it a key tool for the observation of agricultural crops. In the special case of SAR polarimetry, such applications are based on the known sensitivity of polarization of microwaves to crop structure (size, shape, and orientation of leaves, stalks, and fruits), dielectric properties of the canopy (related to the water content), and the physical properties of the underlying soil (roughness and moisture). Crop structure and plant water content vary as a function of crop type, growth stage and crop condition. As a matter of fact, different crops types, or the same type at different growth stages, produce different polarimetric signatures, which can be identified in the acquired images and used to properly address the issues of growth stages monitoring, crops discrimination and the estimation of important dates that characterize the growing season.

1. INTRODUCTION

The main objective of this thesis is the exploiting of polarimetric SAR data for the monitoring and the estimation of penological stages of agricultural crops. In particular, onion and oat fields present in Barrax, Spain, are analyzed. Ground truth information about crop growth stages is provided by the ESA-funded Agricultural bio/geophysical retrieval from frequent repeat pass SAR and optical imaging (AgriSAR) field campaign conducted in the Barrax area in 2009. By taking full benefit of time series of C-band full polarimetric SAR measurements, collected during the ground campaign, a physical interpretation of the behavior of various polarimetric observables at different growth stages is provided and, in a successive step, based on this interpretation, supervised estimation procedures are derived to retrieve such stages.
Regarding onion, the estimation of their growth stage by means of polarimetric SAR data has been first addressed in this study. Experimental results demonstrate that meaningful polarimetric parameters turn out to be fundamental for the phenology retrieval.
Concerning oat, an appreciable sensitivity of the polarimetric observables to the growth stages allows obtaining high estimation accuracies. This important result is in contrast with recent literature studies, carried out on different test sites, and hence leads to the conclusions that this sort of analysis has to be adapted locally to each test site.

The second objective of the thesis deals with a surface-type discrimination in coastal zones characterized by various land cover types, including vegetated and cultivated areas, by exploiting both single- and incoherent dual-polarization X-band SAR data.
In a first study, land is discriminated from sea by using single polarization SAR images for coastline extraction purposes.
In successive study, incoherent dual-polarization SAR data are used for a sea/vegetation/urban discrimination. Results show that, apart form the different performances of the single- and dual-polarization approaches, high sea state conditions significantly affect the discrimination.

This thesis is organized as follows. In Chapter 2, basic concepts on radar polarimetry are reviewed and the polarimetric SAR observables used in the thesis are described.
In Chapter 3 a detailed analysis of polarimetric observables evaluated over two crop types, i.e. onion and oat, during the growing season, is provided and tailored estimation procedures are defined to estimate the phenological stages. Regarding onion, its growth stages are estimated for the first time while, for oat, he procedure turns out to be effective.
Finally, in Chapter 4 different land cover types are discriminated by procedures based on single-polarization and incoherent dual-polarization data analysis.

2

Polarimetric SAR observables

2.1 Single-polarization SAR observables

Let us consider single-polarization imaging radar illuminating a distributed target, such as a forested area. In this case, the backscattering behavior of the imaged scene is characterized by the Normalized Radar Cross Section (NRCS), also known as *scattering coefficient* [1]. If we denote with p the polarization of the illuminating electric field $\mathbf{E}^I$ and with q the polarization of the scattered electric field $\mathbf{E}^S$, the polarization dependent scattering coefficient is given by [1, 2]

$$\sigma^0_{\mathrm{qp}} = \frac{4\pi r^2}{A} \frac{\langle |\mathbf{E}_{\mathrm{q}}{}^S|^2 \rangle}{|\mathbf{E}_{\mathrm{p}}{}^I|^2} \quad , \tag{2.1}$$

where r is the distance between the target and the antenna, A is the illuminated area and $\langle \cdot \rangle$ denotes the ensemble average. σ^0_{qp} is a dimensionless quantity and represents the meaningful observable derived from single-polarization measurements. It depends on various parameters including operating frequency, incidence and scattering directions and both geometrical and dielectric properties of the imaged scene [1].

In the backscattering case, e.g. when dealing with SAR systems, σ^0_{qp} is referred as *backscattering coefficient*. Due to the dependence of the scattering/backscattering coefficient on both geometrical and dielectric properties of the target, this parameter has been widely employed in literature for agriculture applications, such as crop observation and soil moisture estimation.

2.2 Polarimetric SAR observables

Single-polarization radar systems allows describing the scattering properties of a distributed target by means of the scattering or backscattering coefficient. However, the dependence of this observables on polarization is experienced only through the intensities of the incident and scattered radiations [1]. Hence, in order to take full benefit of the polarization of electromagnetic fields in the description of the scattering process, more sophisticated imaging radar systems have to be employed. These systems are referred as *polarimetric* radars.
In this section the basic principles of radar polarimetry are summarized and the polarimetric SAR observables that are used in this thesis are described.

2.2.1 Scattering matrix

Let us consider that a monochromatic electromagnetic plane wave, characterized by a well-defined polarization state described according to an orthogonal system right-hand (RH) with respect to the incident direction $\hat{\imath}$, is incident upon a target. A receiving antenna, located at large distance from the target in a direction $\hat{s}$, receives the scattered plane wave, whose polarization state depends on the target characteristics.
The complex Jones vectors [1–4] associated to incident and scattered fields, $\mathbf{E}^i$ and $\mathbf{E}^s$, are defined as

$$\mathbf{E}^i = \begin{bmatrix} E_{\mathrm{X}^i} \\ E_{\mathrm{Y}^i} \end{bmatrix} \quad \mathbf{E}^s = \begin{bmatrix} E_{\mathrm{X}^s} \\ E_{\mathrm{Y}^s} \end{bmatrix} \tag{2.2}$$

where (X,Y) are the two wave orthogonal components defined in a plane orthogonal to the propagation direction. The scattering process, which can be regarded as the transformation of the polarization sate $\mathbf{E}^i$ into $\mathbf{E}^s$, can be completely described, for deterministic targets, according to the Jones formalism [1, 3, 4]

$$\mathbf{E}^s = \frac{e^{-jkr}}{r} \begin{bmatrix} S_{\mathrm{XX}} & S_{\mathrm{XY}} \\ S_{\mathrm{YX}} & S_{\mathrm{YY}} \end{bmatrix} \mathbf{E}^i \quad , \tag{2.3}$$

where $\frac{e^{-jkr}}{r}$ is the spherical wave factor and $\mathbf{S}$ is the 2×2 complex scattering matrix [1–4]. The entries of $\mathbf{S}$ are named the complex scattering coefficients or scattering amplitudes. The element $S_{\mathrm{qp}} = |S_{\mathrm{qp}}|e^{j\phi_{\mathrm{qp}}}$ is the scattering coefficient relevant to the the incident field with p-polarization and the received field with q-polarization. The diagonal elements of the scattering matrix are refereed as co-polar terms while the off-diagonal ones are referred as cross-polar terms. If one neglects the absolute phase, which cannot be measured in practice [4], $\mathbf{S}$ consists

of seven independent parameters: four amplitudes and three relative phases.

It must be explicitly pointed out that, for a given frequency and scattering geometry, **S** depends only on the scattering target. However, the mathematical expression of the scattering matrix depends on the coordinate system that is adopted for describing the incident and the scattered fields. Two conventions are commonly used: Forward Scattering Alignment (FSA) and Backward Scattering Alignment (BSA). All coordinate systems are defined in terms of a global coordinate system centered inside the scatterer [1, 4]. The FSA convention, shown in Fig.2.4(a), is related to the direction of propagation of the waves. This convention is commonly adopted for bistatic configurations. On the other hand, the BSA convention (see Fig.2.4(b)) is related to the antennas and is frequently used for monostatic configurations, since in this case the same coordinate system is used for describing the polarization of both the incident and the scattered waves [1, 4]. The scattering matrix expressed in the BSA convention, $\mathbf{S}_{\mathrm{BSA}}$, can be

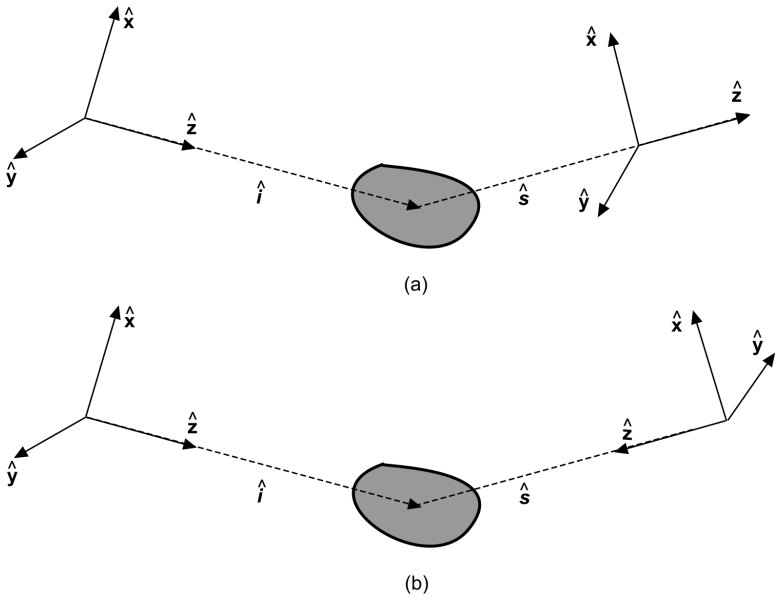

Figure 2.1: Bistatic scattering: (a) FSA; (b) BSA.

obtained by the one expressed in the FSA convention, $\mathbf{S}_{\mathrm{FSA}}$, by means of a simple relationship [4]

$$\mathbf{S}_{\mathrm{FSA}} = \begin{bmatrix} 1 & 0 \\ 0 & -1 \end{bmatrix} \mathbf{S}_{\mathrm{FSA}} \quad . \tag{2.4}$$

Dealing with the practical case of backscattering in a reciprocal medium, the following relationships hold

$$S_{\mathrm{YX}} = -S_{\mathrm{XY}} \quad , \tag{2.5}$$

if the FSA convention is used and

$$S_{\mathrm{YX}} = S_{\mathrm{XY}} \quad , \tag{2.6}$$

if the BSA convention is used. It must be noted that, when (2.5) or (2.6) hold, the scattering matrix consists of five independent parameters: three amplitudes and two relative phases.

The scattering matrix represents the basic measurements of a polarimetric radar. In order to show how this measurement is undertaken, we focus on the particular case of a SAR sensor. A *full* polarimetric SAR, also referred as *quad-pol* SAR, measures, for each resolution cell, the four elements of the scattering matrix. In order to do that, it is fundamental to maintain phase coherence during the measurements.

Let us consider the linear horizontal (h) and vertical (v) polarizations, with consist of the most commonly used polarization basis in SAR remote sensing. The first column of $\mathbf{S}$ (2.3) is measured by transmitting a h-polarized pulse and receiving echoes in the co- and the cross-polarized channels simultaneously. Similarly, the second column of $\mathbf{S}$ is measured by transmitting a pulse with v polarization and receiving the h and v components of the scattered radiation simultaneously. In such a way the four entries of $\mathbf{S}$ are measured in the (h,v) basis

$$\mathbf{S} = \begin{bmatrix} S_{\mathrm{hh}} & S_{\mathrm{hv}} \\ S_{\mathrm{vh}} & S_{\mathrm{vv}} \end{bmatrix} \quad . \tag{2.7}$$

Hence, the quad-pol configuration is based on interleaving the h and v transmit polarizations and receiving both the h- and v-polarized echoes. The switch between transmit pulses is so fast that, practically, the two columns of $\mathbf{S}$ can be considered as simultaneous measurements, thus allowing to maintain phase coherence. Due to this switching scheme, one of the main drawbacks of quad-pol SAR mode is that the width of the imaged swath is the half of the single-polarization mode, since the Pulse Repetition Frequency (PRF) is doubled.

A different operational mode of polarimetric SAR systems consists of measuring only one column of the scattering matrix $\mathbf{S}$, i.e. one copolar channel and the cross-polarized channel. These systems are referred as *coherent dual-polarimetric* SARs. It turns out that a significant advantage of these SAR systems with respect to quad-pol ones is the larger swath width, which is the same of the one provided by the single-pol SAR mode. Actual space-borne SARs, e.g. the Canadian RADARSAT–2 (C–band), the one onboard the Japanese ALOS-PALSAR–2 (L–band) support, apart from the conventional single-polarization mode, both the dual- and the quad-pol mode in the (h,v) basis. The European Space Agency (ESA) Sentinel–1 SAR sensor, operating at the C–band, supports only the dual-polarimetric mode.

2.2.2 Polarimetric covariance and coherency matrices

When a radar illuminates a deterministic targets the scattered wave is *completely polarized* [4]. This means that the its polarization state is deterministic, i.e. the wave is monochromatic, with the tip of the electric field describing, in general, an ellipse. In this case, the scattering process can be completely described by **S**.

This situation changes when dealing with distributed targets. These targets (e.g. sea surface, terrain, vegetated areas...) are composed by randomly distributed deterministic scatterers. Therefore, when a distributed target is illuminated by a monochromatic plane wave whose polarization state is well defined, the scattered wave will be, in general, *partially polarized* [1], that is, its polarization state changes randomly. This is due to the randomness of the imaged scene which, in the most extreme case, gives rise to an *unpolarized* scattered wave, i.e. a wave whose polarization state behaves in a completely random way, since it is equally probable to be anyone. Partial polarization lies between the two extreme cases of completely polarized and unpolarized waves.

The scattering matrix is, therefore, not able to describe the scattering process of distributed or *depolarizing* targets [3], since, in this case, its elements must be considered as random processes. As a consequence, second-order statistical characterizations of the scattering process, provided by the polarimetric covariance and the coherency matrices, are introduced.

In this thesis, C–band RADARSAT–2 full polarimetric SAR data are used, and polarimetric observables derived from both the covariance and the coherency matrices are analyzed. Therefore, in the following, only those observables used in the thesis are described. In addition, the BSA convention is adopted, which implies $S_{\mathrm{vh}}{=}S_{\mathrm{hv}}$.

According to the target vectors formalism [5], the scattering matrix can be expressed in vectorial form, by defining the target vector **k** as

$$\mathbf{k} = \frac{1}{2}\mathrm{Trace}(\mathbf{S}\Psi) \quad , \tag{2.8}$$

where Trace$(\cdot)$ denotes the sum of the diagonal elements of a matrix and Ψ is a set of 2×2 complex basis matrices which are constructed as an orthonormal set under an hermitian inner product [5]. Although several basis sets can be found in literature, two particular sets are often used: the Lexicographic basic set Ψ_L, and the Pauli basis set Ψ_P. The mathematical expression of both Ψ_L and Ψ_P can be found in [1, 5].

In the backscattering case, under the BSA convention, the target vector is given by

$$\mathbf{k}_L = \begin{bmatrix} S_{\mathrm{hh}} & \sqrt{2}S_{\mathrm{hv}} & S_{\mathrm{vv}} \end{bmatrix}^T \quad , \tag{2.9}$$

in the lexicographic basis, and by

$$\mathbf{k}_P = \frac{1}{\sqrt{2}} \begin{bmatrix} S_{\mathrm{hh}} + S_{\mathrm{vv}} & S_{\mathrm{hh}} - S_{\mathrm{vv}} & 2S_{\mathrm{hv}} \end{bmatrix}^T \quad , \tag{2.10}$$

in the Pauli basis.

The covariance matrix $\mathbf{C}$ and the coherency matrix $\mathbf{T}$ are defined by means of $\mathbf{k}_L$ and $\mathbf{k}_P$, respectively.

The 3×3 complex covariance matrix is given by

$$\mathbf{C} = \langle \mathbf{k}_L \cdot \mathbf{k}_L{}^{\dagger} \rangle = \begin{bmatrix} \langle |S_{\mathrm{hh}}|^2 \rangle & \sqrt{2}\langle S_{\mathrm{hh}} S_{\mathrm{hv}}^* \rangle & \langle S_{\mathrm{hh}} S_{\mathrm{vv}}^* \rangle \\ \sqrt{2}\langle S_{\mathrm{hv}} S_{\mathrm{hh}}^* \rangle & 2\langle |S_{\mathrm{hv}}|^2 \rangle & \sqrt{2}\langle S_{\mathrm{hv}} S_{\mathrm{vv}}^* \rangle \\ \langle S_{\mathrm{vv}} S_{\mathrm{hh}}^* \rangle & \sqrt{2}\langle S_{\mathrm{vv}} S_{\mathrm{hv}}^* \rangle & \langle |S_{\mathrm{vv}}|^2 \rangle \end{bmatrix} \quad , \tag{2.11}$$

while the 3×3 complex coherency matrix is given by

$$\mathbf{T} = \langle \mathbf{k}_P \cdot \mathbf{k}_P{}^{\dagger} \rangle \tag{2.12}$$

which yelds

$$\mathbf{T} = \frac{1}{2} \begin{bmatrix} \langle |S_{\mathrm{hh}} + S_{\mathrm{vv}}|^2 \rangle & \langle (S_{\mathrm{hh}} + S_{\mathrm{vv}})(S_{\mathrm{hh}} - S_{\mathrm{vv}})^* \rangle & 2\langle (S_{\mathrm{hh}} + S_{\mathrm{vv}}) S_{\mathrm{hv}}^* \rangle \\ \langle (S_{\mathrm{hh}} - S_{\mathrm{vv}})(S_{\mathrm{hh}} + S_{\mathrm{vv}})^* \rangle & \langle |S_{\mathrm{hh}} - S_{\mathrm{vv}}|^2 \rangle & 2\langle (S_{\mathrm{hh}} - S_{\mathrm{vv}}) S_{\mathrm{hv}}^* \rangle \\ 2\langle S_{\mathrm{hv}} (S_{\mathrm{hh}} + S_{\mathrm{vv}})^* \rangle & 2\langle S_{\mathrm{hv}} (S_{\mathrm{hh}} - S_{\mathrm{vv}})^* \rangle & 4\langle |S_{\mathrm{hv}}|^2 \rangle \rangle \end{bmatrix} \quad . \tag{2.13}$$

In (2.11)–(2.13) † and * denote the conjugate transpose and the complex conjugate, respectively. $\mathbf{C}$ and $\mathbf{T}$, both Hermitian and semidefinite positive matrices, can be estimated by assuming statistical ergodicity and homogeneity. Hence, the ensemble average can be replaced by a spatial averaging that is undertaken by a multilook process [6]. In addition, if one of these two matrices is estimated, the other one can be straightforwardly obtained from it, since they are related by a unitary similarity transformation [5]

$$\mathbf{C} = \frac{1}{2} \begin{bmatrix} 1 & 1 & 0 \\ 0 & 0 & \sqrt{2} \\ 1 & -1 & 0 \end{bmatrix} \mathbf{T} \begin{bmatrix} 1 & 0 & 1 \\ 1 & 0 & -1 \\ 0 & \sqrt{2} & 0 \end{bmatrix} \quad . \tag{2.14}$$

In this thesis both the covariance and the coherency matrices are used, since polarimetric observables involved in the description of the radar response to phenological stages of crops, and hence their estimation, are derived from both the two matrices.

2.2.3 Polarimetric SAR observables derived from the covariance matrix

In tis thesis, three sets of observables are derived form the **C** matrix: the backscattering coefficients at the HH,VV and HV channels, the polarization ratios and the complex coherence between the copolar channels.

The backscattering coefficients at the linear polarizations consist of the diagonal elements of **C** (2.11). Regarding the polarization ratios, the copolar ratio is defined as

$$r_{\mathrm{hh/vv}} = \frac{\langle |S_{\mathrm{hh}}|^2 \rangle}{\langle |S_{\mathrm{vv}}|^2 \rangle} = \frac{C_{11}}{C_{33}} \quad , \tag{2.15}$$

while the cross-polarization ratio are given by

$$r_{\mathrm{hv/hh}} = \frac{\langle |S_{\mathrm{hv}}|^2 \rangle}{\langle |S_{\mathrm{hh}}|^2 \rangle} = \frac{1}{2}\frac{C_{22}}{C_{11}} \qquad r_{\mathrm{hv/vv}} = \frac{\langle |S_{\mathrm{vh}}|^2 \rangle}{\langle |S_{\mathrm{vv}}|^2 \rangle} = \frac{1}{2}\frac{C_{22}}{C_{33}} \quad . \tag{2.16}$$

Concerning the complex coherence between the HH and VV channels, it is defined as

$$\rho_{\mathrm{hhvv}} = |\rho_{\mathrm{hhvv}}| e^{j\phi_{\mathrm{hhvv}}} = \frac{\langle S_{\mathrm{hh}} S_{\mathrm{vv}}^* \rangle}{\sqrt{\langle |S_{\mathrm{hh}}|^2 \rangle \langle |S_{\mathrm{vv}}|^2 \rangle}} = \frac{C_{13}}{\sqrt{C_{11} C_{33}}} \quad . \tag{2.17}$$

where ϕ_{hhvv} is the phase difference between HH and VV or copolar phase difference (CPD). Both $|\rho_{\mathrm{hhvv}}|$ and ϕ_{hhvv} are important observables for agriculture applications.

$|\rho_{\mathrm{hhvv}}|$, also named as copolar coherence, should be very high in the case surface scattering, while it is expected to be low when volume scattering, i.e. the scattering from the vegetation layer, is present [7].

Concerning ϕ_{hhvv}, it can be related to the scattering mechanisms present in the scene [8]. It is expected to be low for surface scattering [7]. On the other hand, when the double-bounce scattering mechanism, caused by the interaction between soil and stems, is significant the phase difference between the copolar channels differs from zero. For a pure double-bounce, i.e. the one corresponding to the dihedral type scattering, the CPD should equal 180°. In [8] the CPD was modeled as the sum of three main terms: the phase difference due to the Fresnel reflection at the ground surface; the phase difference due to the bistatic scattering at the stems; the phase difference due to the two-ways propagation through the vegetation layer. A more complete description was provided in [9], where the complex coherence was expressed as the sum of three terms: the complex coherence of the soil surface; the complex coherence of the trunk-soil interaction component; the complex coherence of the vegetation layer. The phase of the first two terms include both the complex HH-VV coherence phase and the phase shift due to the the two-ways propagation through the vegetation layer.

2.2.4 Polarimetric SAR observables derived from the coherency matrix

Unlike the **C** matrix, which is directly related to the radar measurables (powers of the three polarimetric channels), the coherency matrix **T** allows providing a direct and physical interpretation of the scattering process.

The polarimetric observables derived from the coherency matrix that are used in this thesis are grouped in three sets: the backscattering coefficients at the Pauli channels, the complex coherence between the first and the second Pauli channels and the parameters extracted from the well known eigenvalue/eigenvector decomposition of **T** [5]. Regarding this last set, it will be described in the next paragraph.

The Pauli channels consist of the three complex elements of the target vector $\mathbf{k}_P$ (2.10) and they can be referred as Pauli_1, Pauli_2 and Pauli_3, respectively. They can be regarded as related to three elementary scattering mechanisms [1]: the first being the scattering from a plane surface (single or odd-bounce scattering), the second being diplane scattering (double or even-bounce scattering), the third being cross-polarized scattering. Therefore, the strong physical meaning of the three Pauli channels allows to interpret directly important scattering mechanisms present in radar imagery.

Within the framework of this thesis, Pauli_1 is related to the scattering from soil surface, Pauli_2 is associated to the double-bounce between soil and stems and Pauli_3 (coincident with the HV channel) is related to the volume scattering from the vegetation layer.

The backscattering coefficients at the Pauli channels consist of the diagonal elements of **T** (2.13).

Regarding the complex coherence between the first and the second Pauli channels, referred as Pauli coherence, it is given by

$$\rho_{\text{p}} = |\rho_{\text{p}}| e^{j\phi_{\text{p}}} = \frac{\langle (S_{\text{hh}} + S_{\text{vv}})(S_{\text{hh}} - S_{\text{vv}})^* \rangle}{\sqrt{\langle |S_{\text{hh}} + S_{\text{vv}}|^2 \rangle \langle |S_{\text{hh}} - S_{\text{vv}}|^2 \rangle}} = \frac{T_{12}}{\sqrt{T_{11} T_{22}}} \quad . \tag{2.18}$$

In [10] a physical interpretation of the behavior of ρ_{p}, referred as Pauli coherence, in terms of phenological stages of rice fields, was provided. When the HH and VV channels are highly correlated ρ_{p} turns out to be low and hence the backscattering coefficient at the Pauli channels are very different. Then, in the case in which VV is very low both Pauli_1 and Pauli_2 are very similar to the HH channel, thus resulting in a high coherence.

2.2.4.1 Eigenvalue/Eigenvector decomposition

Although several polarimetric decomposition are present in literature, in this thesis eigenvalue/eigenvector decomposition of of the coherency matrix [5], that is briefly described in this paragraph, is used.

Being Hermitian and semidefinite positive, $\mathbf{T}$ can be diagonalized as follows [5]

$$\mathbf{T} = \mathbf{U}\mathbf{\Lambda}\mathbf{U}^{-1} \quad , \tag{2.19}$$

where

$$\mathbf{\Lambda} = \begin{bmatrix} \lambda_1 & 0 & 0 \\ 0 & \lambda_2 & 0 \\ 0 & 0 & \lambda_3 \end{bmatrix} \tag{2.20}$$

with $\lambda_1 \geq \lambda_2 \geq \lambda_3 \geq 0$ being the eigenvalues of $\mathbf{T}$, real and non negative. $\mathbf{U} = [\ \mathbf{u}_1\ \mathbf{u}_2\ \mathbf{u}_3]$ is a 3×3 matrix whose columns are the three orthogonal eigenvectors of $\mathbf{T}$. Note that (2.19) can be rewritten as

$$\mathbf{T} = \sum_{i=1}^{3} \lambda_i (\mathbf{u}_i \cdot \mathbf{u}_i^{\dagger}) = \lambda_1 (\mathbf{u}_1 \cdot \mathbf{u}_1^{\dagger}) + \lambda_2 (\mathbf{u}_2 \cdot \mathbf{u}_2^{\dagger}) + \lambda_3 (\mathbf{u}_3 \cdot \mathbf{u}_3^{\dagger}) = \mathbf{T}_1 + \mathbf{T}_2 + \mathbf{T}_3 \quad , \tag{2.21}$$

where the matrices $\mathbf{T}_i$ are characterized by a rank equal to one and describe deterministic scattering processes. Therefore, (2.19) can be physically interpreted as the decomposition of $\mathbf{T}$ into three independent deterministic scattering processes whose contribute, in terms of power, is given by the appropriate eigenvalue.

The eigenvalues of $\mathbf{T}$ allow defining two important polarimetric observables. The first one is the entropy [5]

$$H = -\sum_{i=1}^{3} p_i \log_3 p_i \quad , \tag{2.22}$$

where

$$p_i = \frac{\lambda_i}{\sum_{l=1}^{3} \lambda_l} \quad . \tag{2.23}$$

H, bounded between 0 and 1, is a measure of the degree of randomness of the scattering process. For H=0, $\mathbf{T}$ is a rank one matrix with only one non-zero eigenvalue, thus implying that a single deterministic scattering mechanism is in place. On the other hand, H=1 implies that a completely random scattering process, characterized by equal and non-zero eigenvalues, which depolarizes completely the incident wave, is occurring [5]. However, most distributed natural scatters lie in between this two extreme cases, having intermediate entropy values.

The second parameter derived from the eigenvalue of $\mathbf{T}$ is the anisotropy A defined as [1]

$$A = \frac{\lambda_2 - \lambda_3}{\lambda_2 + \lambda_3} \quad . \tag{2.24}$$

The anisotropy is complementary to the entropy and represents a measure of the importance of the third eigenvalue with respect to the second one [1]. It turns out to be important for high entropy values (H above 0.7) since it allows distinguishing different types of scattering processes [1].

Further polarimetric observables can be derived from the eigenvectors of $\mathbf{T}$. In facts, each eigenvector can be parametrized as follows [11]

$$\mathbf{u}_i = \begin{bmatrix} \cos\alpha_i & \sin\alpha_i \cos\beta_i e^{j\delta_i} & \sin\alpha_i \sin\beta_i e^{j\gamma_i} \end{bmatrix} \quad . \tag{2.25}$$

Without loss of generality, while β represents a rotation of the target around the line-of-sight, the α angle or *scattering angle* (bounded between 0 and 90°) is the main parameter able to identify the type of scattering mechanism, being a roll-invariant parameter [1]. As a matter of fact, the analysis of (2.25) as function of α allows to identify some typical cases.
When α= 0° the scattering mechanism can be interpreted as *isotropic* surface scattering, i.e. a surface scattering type with S_{hh}=S_{vv}. α= 45° corresponds to a dipole-like scattering. Finally, α= 90° denotes that the scattering mechanism is a dihedral scattering.
Furthermore, it can be shown that the best estimate of α is given by the *average* α angle [11]

$$\overline{\alpha} = p_1\alpha_1 + p_2\alpha_2 + p_3\alpha_3 \tag{2.26}$$

where the angles α_i are obtained by the first element of the eigenvector in (2.25). $\overline{\alpha}$ is a measure of the *average* scattering mechanism that is in place. As a consequence, when the entropy is high it is important evaluate the *dominant* scattering mechanism α_1, i.e. the one corresponding to the larger eigenvalue of $\mathbf{T}$.

2.3 Incoherent dual-polarization SAR observables

A dual-polarization SAR which does not preserve the relative phase between the two received echoes is said to be *incoherent*. As a consequence, due to the lack of phase information, the observables that can be exploited restrict to backscattering coefficients and polarization ratios. In this thesis such systems will be referred as dual-polarization SARs, in order to distinguish them from the coherent dual-polarimetric SARs. Typical examples of these systems are the C–band ESA ENVISAT Advanced SAR (ASAR) Alternating Polarization Mode and the actual X–band COSMO-SkyMed PingPong mode. The latter will be exploited in the last part of this thesis for land cover discrimination purposes. In particular, the peculiarity of this incoherent dual-polarization mode will be detailed later on in the thesis also by defining a new observable.

2.4 Conclusions

In this chapter the basis concepts of radar polarimetry have been reviewed. In particular, those observables that are employed in the thesis have been described.

Regarding the full polarimetric case, deterministic targets can be easily characterized according to the Jones formalism, that is, the scattering matrix. On the other hand, when dealing with distributed target, as is the case of remote sensing, second order statistics have to be employed: the covariance and the coherency matrices. The latter is able to provide a direct physical interpretation of the scattering process. In particular, the eigenvalue/eigenvector decomposition proposed in [5] is of great importance for a better understanding of the scattering mechanisms that take place.

Finally, the lack of phase information in incoherent polarimetric acquisitions represents a key limitation since only some conventional polarimetric observables can be exploited.

3

Estimation of phenological stages of agricultural crops by means of polarimetric SAR measurements

3.1 Introduction

Crop phenology denotes the continuous development of agricultural crops during the cultivation cycle, i.e. from sowing or transplanting to harvest, and it is usually expressed by means of numerical scales [12, 13]. Phenological stages of crops are generally grouped in three main phases: *vegetative*, *reproduction* and *maturation*. The vegetative phase comprises those stages which represent the initial development of plants, starting with the growth from seeds and finishing with fully developed plants. The reproductive phase includes inflorescence emergence and flowering stages, while the maturation phase goes from the development of fruits to plants ripening and senescence.

The monitoring of crop phenology is fundamental for the planning and the management of those cultivation practices (e.g. irrigation, fertilization, etc.) that require timely information about the crop conditions along the cultivation cycle.

Within the framework of active microwave remote sensing, phenology monitoring has not been an attractive topic in the past, due to the lack of proper time series of images, caused by long revisit time (e.g. 35 for ENVISAT and ERS), and the cost of field campaigns along the cultivation cycle that are required to support the development of methodologies. Studies, e.g. [14–22], have demonstrated the relationship between the X- and C- band radar backscattering

at different polarization channels and the growth stages of crops.

The monitoring of crop phenology by means of SAR remote sensing has gained more interest with the launch of space-borne SAR sensors capable to measure different polarimetric channels in a coherent way, such as RADARSAT–2 (C-band), TerraSAR–X (X-band) and the most recently launched Sentinel–1 (C-band). In addition, the shorter revisit time provided by these satellites (11 days for TerraSAR–X and 12 days for Sentinel–1) and the possibility of combining different beams and ascending/descending orbits (especially in the chase of RADARSAT–2, whose revisit time is 24 days) is also of relevant importance, since it allows to provide a dense time sampling throughout the growing season. Recent studies, [10, 23–32] have shown the potential of polSAR measurements in the monitoring of growth stages of agricultural fields in a robust and efficient way when polarimetric observables are used.

To date, the issue of phenology estimation by means of polSAR data has been explicitly addressed in [10, 24, 25, 29–31] where effective retrieval procedures based on supervised classification [10, 24, 25] and dynamical systems concept [29–31] have been proposed. In [10, 25, 29, 31] phenological stages of rice fields have been estimated, while in [24, 30] cereals fields have been considered.

In this chapter, which represents the main contribute to the thesis, polarimetric observables derived by a time series of full polarimetric RADARSAT–2 SAR data is exploited to estimate phenological stages of onion and oat fields present in Barrax, Spain, by means of supervised classification algorithms. Ground truth information about crop growth stages is provided by the ESA-funded Agricultural bio/geophysical retrieval from frequent repeat pass SAR and optical imaging (AgriSAR) field campaign conducted in Barrax in 2009 almost concurrently with the SAR acquisitions. The contents of this chapter is based on papers submitted at international journals and presented at international conferences [33, 34].

The remaining is organized as follows. In section 3.2 the employed methodology is detailed, while in section 3.3 the test site, the ground campaign and the SAR data that are used are described. In section 3.4 [33], polarimetric observables, along with single-polarization intensity channels, are first used to estimate growth stages of onion fields. Experimental results demonstrate that meaningful polarimetric parameters, such as the entropy or copolar coherence, when used jointly with the backscattering intensity provide the best results in the estimation. In section 3.5 [34], phenological stages of oat fields are estimated by means of a classification procedure defined at two different scales. Such an approach, due to an appreciable sensitivity of the polarimetric observables to such growth stages, allows obtaining high estimation accuracies.

3.2 Methodology

This section is aimed at describing the procedure that is followed in this study for the phenology retrieval.

The first step consists of the multi-look process of the available Single Look Complex (SLC) RADARSAT–2 polSAR images, that provides an estimate of the polarimetric covariance matrix $\mathbf{C}$ for each pixel of every image. For such a purpose, a 9×9 sliding boxcar filter is employed. Not the that reciprocity is assumed throughout the study. Then, each matrix is geocoded (UTM coordinates). Once all the covariance matrices are geocoded, from each of them, the polarimetric coherency matrix $\mathbf{T}$ is obtained, being these two matrices, $\mathbf{T}$ and $\mathbf{C}$, related by a unitary similarity transformation [5]. Therefore, for each image of the time series, several polarimetric observables are extracted from the covariance and coherency matrices.

Since we are focused on the analysis of specific parcels, regions of interest (ROIs) corresponding to the parcels in the polSAR images are defined and such observables are evaluated inside these ROIs. Then, the successive step consists of interpreting the evolution of the polarimetric observables in terms of the phenological stages of the crops under study. Such an analysis is based on the representation of these observables as a function of phenology. In particular, for each observable, the mean value and the standard deviation evaluated within each parcel at every radar acquisition are plotted against phenolgy. From this analysis the observables that exhibit the largest sensitivity to the phenological stages are extracted and then used for the phenology retrieval.

Phenological stages of agricultural crops can be seen as *classes* and their identification can be treated as a classification problem [10, 25]. Therefore, once the most meaningful polarimetric observables are selected, the classes, i.e. the stages, can be identified from such a reduced set by means of supervised classification algorithms. In this study, classification procedures based on hierarchical trees and simple decision planes are defined for phenology estimation. Such rule-based algorithms are based on the scattering mechanisms and properties that characterize the specific crop type at the different growth stages. Therefore, hierarchical trees or decision planes are defined by thresholds that are set manually on the base of the polarimetric observables analysis. In addition, the estimation is undertaken by considering each polSAR image independently, i.e. without exploiting any temporal information. For such a purpose such an approach can be considered as *statical* [30].

Concerning the scale, or the level, at which the estimation is provided, it is important to distinguish between *pixel* and *parcel* level. In this study, the estimation is carried out at the pixel level when a pixel in a given image is assigned to a certain phenological stage or interval. On the other hand, phenology is estimated at the parcel level when the whole parcel (entire set of pixels) is assigned to a given stage.

The performance of the estimation is assessed by comparing the outputs of the classification with the available ground truth. Such a validation is carried out at the parcel level, since ground truth are provided only at that level. Then, in the case of a pixel level estimation, the percentage of assigned pixels to each phenological interval is computed for each image, and the mode, i.e. the most retrieved value, is compared with ground measurements. When phenology is estimated at the parcel level, since the whole parcel consists of only one class it will result in a totally correct or totally wrong estimate according to the ground measurements.

3.3 Test site, ground truth and SAR data

Barrax belongs to the province of of Albacete (Spain) and is located on the La Mancha plateau at 700 m above the sea level. Due to the presence of many agricultural fields, the Barrax area has been used as a test site where several remote sensing experiments have been carried out [35–40]. In the AgriSAR field campaign conducted in 2009 in Barrax more than 100 parcels corresponding to different crop types, i.e. wheat, barley, oat, corn, sweet corn, onion, sunflower, pea and papaver, were monitored between the spring and the autumn seasons. Such an intensive field campaign led to two sets of ground measurement. The first one provided information about the phenological stages of all the monitored parcels. These stages are not expressed in terms of a numerical scale, but they are recorded, for all the crop types, in a time window defined by a start and an end date. The start date of a given stage corresponds to the day after the end date of the previous stage. Hence, in the i-th time window, a given parcel is in the i-th phenological stage.

The second set of ground measurements started at the beginning of July and was carried out only in 23 parcels. It provided additional information about phenology and other kind of information such as plant density, row orientation and crop height. Moreover, meteorological measurements, including precipitation events, wind speed and air temperature, were carried out at meteorological stations present in the Barrax area, and information regarding the irrigation schedule of some fields was also provided. From April to September 2009 more than 50

RADARSAT–2 fine quad-pol images (corresponding to different beams and orbit passes) were acquired over the Barrax area during the field campaign. In this study, a time series is built up by combining seven beams, characterized by different incidence angles, that range 23° to 39°, and different orbit passes (ascending/descending), in order to provide a dense revisit time along the cultivation cycle. The characteristics of the RADARASAT–2 images are listed in Table 3.1. It is important to underline that the same SAR data were previously used in [38], where the sensitivity of the backscattering coefficients to growth stages of onion, oat, barley, wheat, and alfalfa fields was analyzed. The present study is intended to complement that work because here the interpretation of the radar response of both oat and onion fields is based on exploiting the whole polarimetric space (i.e. correlations, decompositions outputs) and not only on the backscattering coefficients.

Table 3.1: Characteristics of the RADARSAT–2 images.

	Fine Quad–Polarization mode images						
Beam	FQ4	FQ6	FQ9	FQ11	FQ14	FQ16	FQ20
Orbit	Ascending	Descending	Ascending	Descending	Ascending	Descending	Ascending
Average AOI (degrees)	23	25	28	31	34	36	39
Acquisition time	∼ 6 pm	∼ 6:20 am	∼ 6 pm	∼ 6:20 am	∼ 6 pm	∼ 6:10 am	∼ 6 pm
Radar center frequency	5.405 GHz						
Slant–range pixel spacing	4.73 m						
Azimuth pixel spacing	4.92 m	4.69 m	4.81 m	5.58 m	4.76 m	5.15 m	4.79 m

3.4 Phenology retrieval of Onion fields during the first year of growth

Onion (*Allium Cepa* L.) is recognized as one of the most important vegetable crops worldwide [41].

In this section, the RADARSAT–2 full polarimetric SAR data collected over Barrax during the AgriSAR 2009 field campaign are first exploited to estimate the phenological stages of onion fields present in that area.

Onion is a biennial crop [42], i.e. a crop whose lifecycle has a two-years duration. In the first year of growth, a sown onion seed evolves to a plant and then the bulb starts to grow. Once grown, the bulb overwinters and then, during the spring and the summer of the next year (second year of growth), the onion plant flowers and produces seeds [42].

Therefore, the phenological stages of onion fields during the first year of growth are all comprised

in the vegetative phase of the plant development, while the reproduction and the maturation phases are observed in the second year of growth.
When onion growing is devoted to bulb production for food purposes, plants are usually harvested at the end of the vegetative phase, thus being transformed in annual crops. In this case, the knowledge of phenological stages represents a key information that can be effectively used for the planning and management of those cultivation practices aimed at improving the food crop production. On the other hand, when dealing with seeds production (for onion as well as other vegetable alliums) it is really important to understand how vegetative growth and bulbing interact with the flowering stages, for a successful production of seeds [43]. As a consequence, the monitoring of onion growth stages in the first growing season turns out to be important also in this case. Hence, the interest of this study arises from the importance of the vegetative phase of onion for both food and seeds production, and its final objectives are the monitoring and the estimation of such phenological stages by means of meaningful observables provided by C-band RADARSAT–2 polSAR imagery.

In this section, a procedure similar to the one proposed in [10, 25] to estimate rice fields phenology, is employed, for the first time, to estimate the penological stages of onion fields during the first year of growth.
Hence, the contribute of this study is the physical interpretation of polarimetric observables in terms of growth stages of onion and their use for the estimation of such stages.

3.4.1 Phenological stages of onion in the first year of growth

In this section we briefly describe the phenological stages of onion plants during the first year of growth, i.e. the vegetative phase of the plant development. Such a phase comprises different growth stages, from the *germination* to the maturation of the bulb or *bulb ripening*.
During germination the plant and the radicles evolve from the seed and, at the end of this stage, the cotyledon (seed leaf) emerges through the soil surface with a loop-like shape [43]. When germination is completed, the *leaf development* stage occurs, during which the plant grows its leaves (up to seven). Once the seventh leaf is appeared, the first falls and the plant goes into the *start of bulbing* stage [43]. During this stage, while the second and the third leaves desiccate, the bulb begins to extend and more leaves (from the eighth to the thirteenth leaf) appear and the plant reaches its maximum height.
The next stage is the *bulb swelling* stage, characterized by a rapid growth of the bulb and the desiccation of the fourth-sixth leaf. Moreover, the leaves may bend or fold. This stage is then

followed by the *fall down* stage, in which the weight of the foliage leads it to collapse. Finally, in the bulb ripening stage the outer skin of the bulb becomes dry and the foliage desiccates.

3.4.2 Ground truth

In this study, we focus on seven onion parcels located in Barrax and its surroundings. These parcels are clearly visible in the Google Earth picture shown in Fig.3.1. Note that parcels E, F and G were also analyzed in [38].

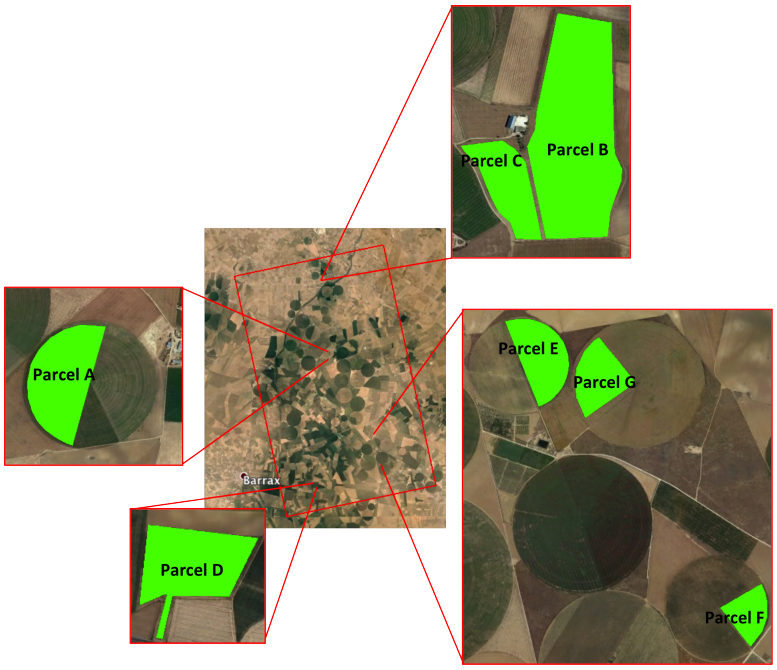

Figure 3.1: Onion parcels considered in the analysis. Seven fields, highlighted in green, are analyzed.

Information regarding the phenological stages of the parcels is provided by the main set of ground measurements as reported in Table 3.2, where nine stages are identified. Although some of the dates in Table 3.2 may be the same for different parcels, in general they differ from one parcel to another.

It must be pointed out again that the succession of phenological stages listed in Table 3.2 corresponds to the vegetative phase of the onion parcels since, according to the two years lifecycle of onion, the presence of both the foliage and the bulb growth stages witnesses that the reproductive and the maturation phases do not occur. Therefore, we are observing onion fields in their first year of growth. The *seedling* stage refers to the growth of the cotyledon

before and after its emergence through the soil, while stages from $STAGE_2$ (*2 leaves* stage) to $STAGE_6$ (*6–7 leaves* stage) denote the leaf development stage. Then, the *start of bulb growth*, the *bulb growth* and the *ripening* stages should correspond to the *start of bulbing*, the *bulb swelling* and the *bulb ripening* stages, respectively. Regarding to the last stage, it is reasonable to assume that it also includes the *fall down* stage.

Table 3.2: Phenological stages of onion parcels provided by the main set of ground measurements. The start and the end date of each stage are different for all the parcels.

Time window	Phenological stage
Start date$_{STAGE_1}$ – End date$_{STAGE_1}$	$STAGE_1$: Seedling
Start date$_{STAGE_2}$ – End date$_{STAGE_2}$	$STAGE_2$: 2 leaves
Start date$_{STAGE_3}$ – End date$_{STAGE_3}$	$STAGE_3$: 2–3 leaves
Start date$_{STAGE_4}$ – End date$_{STAGE_4}$	$STAGE_4$: 3–4 leaves
Start date$_{STAGE_5}$ – End date$_{STAGE_5}$	$STAGE_5$: 5–6 leaves
Start date$_{STAGE_6}$ – End date$_{STAGE_6}$	$STAGE_6$: 6–7 leaves
Start date$_{STAGE_7}$ – End date$_{STAGE_7}$	$STAGE_7$: Start of bulb growth
Start date$_{STAGE_8}$ – End date$_{STAGE_8}$	$STAGE_8$: Bulb growth
Start date$_{STAGE_9}$ – End date$_{STAGE_9}$	$STAGE_9$: Ripening

An important aspect that may provide information, although roughly, about the end of the ripening stage is the knowledge of the harvest date. The start date of seedling and the end date of ripening of all the parcels, along with further information recorded by the second set of ground measurements (phenology, harvest date and the row orientation) are listed in Table 3.3, where each date is also expressed in Day of Year (DoY). Note that the start of seedling and the end of ripening are simultaneous for some parcels. The sowing date is not reported since it is not provided for any parcel. Regarding the harvest date, it is provided only for parcels E and F (only an approximate date is indicated). If we focus on parcel A we note that while the end date of the ripening stage is on August 19, further information indicates that the parcel is still in the ripening stage on September 10. For those parcels whose the harvest date is not provided, there is no information, not even approximate, about the the end of the ripening stage.

3.4.3 RADARSAT–2 images relevant to onion parcels

According to the duration of the growing season of the analyzed parcels (see Table 3.3), a proper set of the available RADARSAT–2 images is used in this study. Unfortunately, four parcels

Table 3.3: Additional information regarding the onion parcels analyzed. Horizontal lines denote that the information is not provided.

Parcel	Start date$_{Seedling}$ (DoY)	End date$_{Ripening}$ (DoY)	Further information about phenology (second set of ground measurements)	Harvest date (DoY)	Row orientation
A	March 30 (89)	August 19 (231)	September 10 (DoY 253): the parcel is in the ripening stage	–	North-South
B	March 15 (74)	August 22 (234)	–	–	North-South
C	March 15 (74)	August 19 (231)	–	–	–
D	April 19 (109)	August 19 (231)	–	–	North-South
E	March 30 (89)	August 23 (235)	–	Since September 20 (263)	NorthEast-SouthWest
F	March 30 (89)	August 23 (235)	–	Since September 20 (263)	–
G	March 30 (89)	August 23 (235)	–	–	–

(A, B, C and D) fall outside the coverage of some beams. Hence, for these parcels a smaller set of images is used. In Table 3.4 the list of the beams that cover a parcel is reported for all the parcels, along with the effective number of images used for the analysis. Note that those images acquired after the end of ripening for parcels B, C, D and G, after September 10 for parcel A, and until two days before the harvest date for parcels E and F, are not considered. Moreover, for some acquisition dates the presence of man–made objects within a specific parcel and some artifacts were present at the borders of parcels, led, in some cases, to the removal of a few other images from the analysis.

Table 3.4: RADARSAT–2 images used for each parcel.

Parcel	Beams that cover the parcel	Number of images used
A	All except FQ20	**33**: from April 3 to August 31
B	All except FQ16 and FQ20	**30**: from April 3 to August 21
C	All except FQ16 and FQ20	**27**: from April 3 to August 14
D	All except FQ20	**29**: from April 23 to August 15
E	All	**43**: from April 3 to September 18
F	All	**45**: from April 3 to September 18
G	All	**40**: from April 9 to August 21

A key aspect of this study is the analysis of the evolution of radar response of the parcels as a function of their phenological stages. In this study a simplified numerical scale is defined in order to describe the phenology observations reported in Table 3.2. Such an *ad hoc* scale is built by following the scheme reported in Table 3.5. In this scheme each start/end date is assigned to a number between 0 and 10. For instance, let us to consider an onion plant in the seedling stage ($STAGE_1$). According to the scheme, the start date of seedling is assigned to "0", while

the end date is assigned to "1". Therefore, as the plant evolves continuously in time from the start to the end of this stage, at a given day it will be in a particular *state* corresponding to a number between 0 and 1. Regarding the second stage (2 leaves), while the start date of this stage is still assigned to "1" (since it can be assumed that the plant does not evolve very rapidly from one day to the next), the end date is assigned to "2". Hence, while the plant is in the second stage, its state in a certain day is associated with a number between 1 and 2, and so on until the ripening stage ($STAGE_9$). In this specific case, we take full benefit of all the information provided in Table 3.3. For all the parcels, but parcel A, the end date of ripening is considered and assigned to "9". In the case of parcel A the date September 10 is assigned to "9" (see Table 3.3). Moreover, for those parcels whose harvest date is provided (parcels E and F) we define a tenth stage, the *pre–harvest* stage, by assigning such a date to "10". The resulting phenological scale derived from such a scheme is presented in Table 3.6. Then, since the radar acquisitions are, in general, not coincident with the ground measurements, a linear interpolation is undertaken in order to derive phenology, in terms of the numerical scale adopted, at the radar acquisition dates [10, 25].

3.4.3.1 Backscattering coefficients at linear polarizations and copolar ratio

The evolution of the HH, VV and HV backscattering coefficients, is shown as a function of phenology in Fig.3.2(a)-(c), respectively. Note that at the bottom of the figure, a legend denoting the orbit pass ("A" stands for Ascending and "D" stands for Descending) and the average incidence angle of each beam, along with the mark corresponding to each parcel, is annotated. According to the legend, hereinafter we will refer to a particular beam by the corresponding pass and incidence angle. Note that the same format is adopted in all the subsequent experiments. We first focus on the backscattering at the copolar channels and their ratio, shown in in Fig.3.2. We note that, from stages 0 to 2 (seedling–2 leaves stages) their evolution is quite similar, while in terms of absolute values the VV backscattered power is, for most of the parcels, larger than or equal to the HH one. As a consequence, the copolar ratio, is between -2 and 0 dB. This implies that the scattering from slightly rough/rougher surfaces dominates.

From the 2 leaves to the start of bulb growth (stages 2–7), the HH backscattering coefficient increases, on average, from $\sim$ -13 to $\sim$ -8 dB, while the backscattering at the VV channel increases from $\sim$ -12 to $\sim$ -10 dB. This is mostly due to leaves emergence. In fact, onion leaves emerge in two ranks at 180° from each other [43]. As a consequence, the structure of the plants

Table 3.5: Scheme used to build the numerical scale associated with the phenological evolution of the onion parcels.

Start date$_{STAGE_1}$	$\longrightarrow$ 0	End date$_{STAGE_1}$	$\longrightarrow$ 1
Start date$_{STAGE_2}$	$\longrightarrow$ 1	End date$_{STAGE_2}$	$\longrightarrow$ 2
Start date$_{STAGE_3}$	$\longrightarrow$ 2	End date$_{STAGE_3}$	$\longrightarrow$ 3
Start date$_{STAGE_4}$	$\longrightarrow$ 3	End date$_{STAGE_4}$	$\longrightarrow$ 4
Start date$_{STAGE_5}$	$\longrightarrow$ 4	End date$_{STAGE_5}$	$\longrightarrow$ 5
Start date$_{STAGE_6}$	$\longrightarrow$ 5	End date$_{STAGE_6}$	$\longrightarrow$ 6
Start date$_{STAGE_7}$	$\longrightarrow$ 6	End date$_{STAGE_7}$	$\longrightarrow$ 7
Start date$_{STAGE_8}$	$\longrightarrow$ 7	End date$_{STAGE_8}$	$\longrightarrow$ 8
Start date$_{STAGE_9}$	$\longrightarrow$ 8	End date$_{STAGE_9}$/ Additional information	$\longrightarrow$ 9
		Harvest date	$\longrightarrow$ 10

Table 3.6: Phenology of the onion parcels described in terms of the numerical scale defined in Table 3.5.

Stage	Phenology	Numerical scale
$STAGE_1$	Seedling	0–1
$STAGE_2$	2 leaves	1–2
$STAGE_3$	2–3 leaves	2–3
$STAGE_4$	3-4 leaves	3–4
$STAGE_5$	5–6 leaves	4–5
$STAGE_6$	6–7 leaves	5–6
$STAGE_7$	Start of bulb growth	6–7
$STAGE_8$	Bulb growth	7–8
$STAGE_9$	Ripening	8–9
$STAGE_{10}$	Pre-harvest	9–10

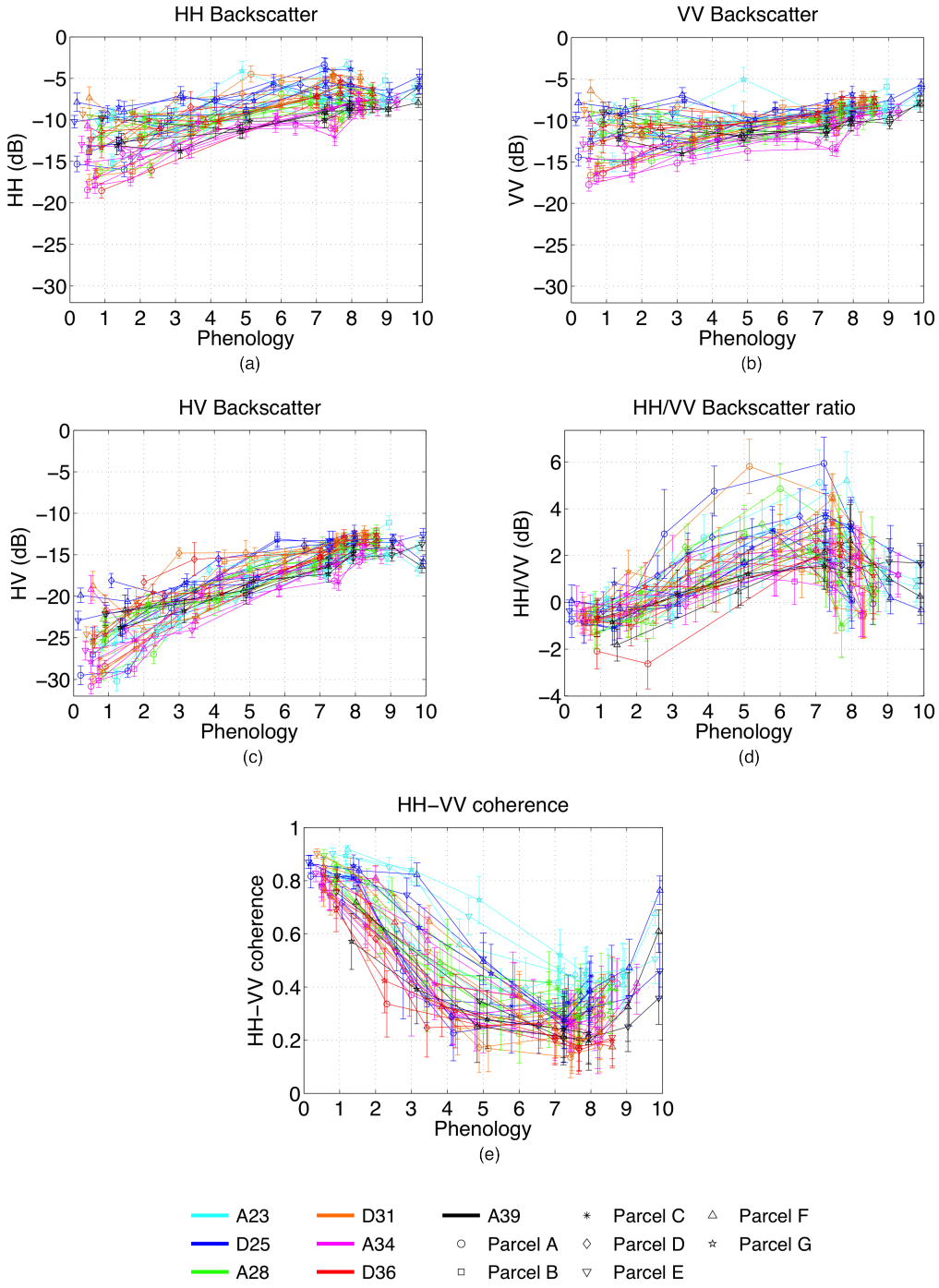

Figure 3.2: Evolution of the polarimetric observables extracted from the covariance matrix **C**. (a) HH backscattering coefficient; (b) VV backscattering coefficient; (c) HV backscattering coefficient; (d) Copolar ratio; (e) Copolar coherence.

becomes more and more random as new leaves appear and hence there is more scattering from the canopy layer. However, in the case of the VV channel such an increase is less significant and the backscattering level is reduced below the HH one, thus leading to an increase of the copolar ratio. This can be attributed to those leaves whose orientation is almost-vertical (younger leaves) that determine an attenuation of the VV backscattering coefficient with respect the HH one.

From the bulb growth to the ripening stage (7–9) the HH backscattering coefficient remains, on average, fairly flat, while the VV one increases of about 1.5 dB. Hence, the copolar ratio decreases up to values around 1 dB. This can be explained by the more random structure of the plants at these stages, which gives rise to a significant multiple scattering in the canopy layer and hence to an extreme depolarization. In this case, the the VV backscattering coefficient gets closer to the HH one, resulting in a decrease of the copolar ratio which, theoretically, should be close to 0 dB [7].

Finally, during the pre-harvest stage (9–10) the HH (VV) backscattering coefficient increases of about 1.5 (2) dB. It must be explicitly pointed out that during the acquisition of the beams A23 and A39, rain events took place. Information relevant to weather conditions gathered at the Barrax meteorological station recorded almost 13.7 mm of rainfall eight hours before the acquisition of the A23 image, and a maximum rainfall of ~ 1 mm in the day in which the A39 image was acquired.

Concerning the HV backscattering coefficient (Fig.3.2(c)), it increases of about 10 dB from the initial bare surface scattering up to the bulb growth stage, thanks to the emergence and development of new leaves, which increase the randomness of the plant structure. Among the three backscattering channels, the cross-poalrized one presents the largest dynamic range.

It must be underlined that, for parcel G, the trends reported in Fig.3.2(a)-(c) are in total agreement with results reported in [38] although in that work a different representation is used (plots against DoY).

3.4.3.2 Coherence between copolar channels

The evolution of the copolar coherence, $|\rho_{\mathrm{hhvv}}|$, as a function of phenology is shown in Fig.3.2(e). From stages 0 to 2, when surface scattering is the most important contribution to the radar response, we observe, as expected, a high coherence with values between 0.6 and 1 (for parcel D, i.e. beam D36, and parcel G, i.e. beam A39, such values are slightly below 0.6).

As the plants foliage develops from stage 2 to 7 the coherence decreases, as expected, to values

between 0 and ~ 0.4. However, if we focus on the evolution of beams A23 and D25 for parcels E, F and G, it presents higher values with respect to the evolution of the other beams, and to the evolution of the same beams for the other parcels. Regarding beam D25 around stage 3, the larger $|\rho_{\mathrm{hhvv}}|$ values obtained over parcel E (> 0.7) and parcel G (> 0.6) are due to irrigation. The irrigation schedule, provided only for these two fields, reports that, in that day (May 21, DoY 141), both the fields were irrigated with about 8 (6) mm of water for parcel E (parcel G). Moreover, parcel G was also irrigated on June 14 (DoY 165) when the acquisition of the beam D25 image between stages 5 and 6 occurred. Therefore the higher level of backscattering from the ground led to an increase of $|\rho_{\mathrm{hhvv}}|$, that, as expected is more noticeable at steeper incidence angles. With respect to parcel F, which results in a larger coherence value ($|\rho_{\mathrm{hhvv}}| > 0.8$), unfortunately no information about irrigation is provided. Concerning beam A23, neither parcel E nor parcel G were irrigated when the images were acquired. Therefore, a possible explanation of the high coherence values exhibited by the beam A23 over parcels E and G can be related to the row orientation of the parcels (see Table 3.3) with respect to the line of sight of the radar. In fact, when dealing with row planted fields, the backscattering at the copolar channels may be significantly affected by the row orientation [44]. As a consequence, the coherence between the copolar channels should be affected as well. This could explain those high coherence values that, otherwise, can not be explained, since, according to ground measurements, they are not due to rain events or irrigation.

From stages 7 to 8 $|\rho_{\mathrm{hhvv}}|$ remains mainly below 0.4, due to the fully developed foliage of the plants. Then, in the ripening stage an increase is experienced, caused by fact that leaves start to collapse and desiccate.

At the end of the pre-harvest stage, which practically consists of the advanced ripening stage that is deducted by the knowledge of the harvest date, we observe an increase of the copolar coherence for parcel F ($|\rho_{\mathrm{hhvv}}|$ values between 0.6 and 0.8) with respect to parcel E ($|\rho_{\mathrm{hhvv}}|$ values below 0.5). Although, as underlined in the previous subsection, rain events occurred on the days in which beams A23 and A39 were acquired, such an effect can be related to the harvesting (see Table 3.3). In fact, it is quite probable that the harvesting occurred immediately after September 20 for parcel F and a little further away for parcel E. This explains the high values of $|\rho_{\mathrm{hhvv}}|$ for parcel F, being the backscattering from this parcel practically consisting of surface scattering.

3.4.3.3 Eigenvalue/Eigenvector decomposition

In this subsection, the behavior of the polarimetric observables obtained from the eigenvalue/eigenvector decomposition of the coherency matrix [5, 11] is analyzed. Fig.3.3 shows the evolution, as a function of phenology, of the entropy, the anisotropy, the average scattering angle $\overline{\alpha}$, and dominant scattering angle α_1.

First, we note that these observables exhibit a clear trend that allows to interpret the radar response of the parcels in terms of the scattering mechanisms that take place as the plants develop. Moreover, according to the behavior of the copolar coherence shown in Fig.3.2(e), the evolution of the entropy, $\overline{\alpha}$ and α_1 relevant to beams A23 and D25 for parcels E, F and G is characterized by lower values with respect to the other cases, due to irrigation and row orientation.

From the seedling to the 3/4 leaves stage (0–4) entropy increases from values between 0.2 and 0.6 to values between 0.7 and 0.9, whereas the anisotropy assumes low values (between 0.2 and 0.5 with a peak around 0.6). The lowest values of entropy at the beginning of the growing season indicate the presence of a single scattering mechanism that can be interpreted as surface-type, according to $\overline{\alpha}$ and α_1. Then, as plants develop up to stage 4, the entropy increases as a consequence of leaves emergence. The high values of entropy experienced at the end of this fourth stage witness that the scattering from an almost random volume is taking place. In fact, four leaves are fully emerged (see Table 3.2) with the older (outer) leaves, i.e. the second and the third, very tilted. Regarding the average and the dominant scattering angle at this stage, values of $\overline{\alpha}$ between 30° and 50° are observed, while α_1 is mainly below 20°, denoting that the dominant scattering mechanism is still the one from the soil surface.

From stages 4 to 9 entropy tends to 0.9, reaching its maximum at the end of ripening. Concerning anisotropy, it decreases to even lower values below 0.3. This trend is due to the high random structure of the canopy, caused by the emergence of further leaves and then by the bending of the leaves in the bulb growth stage. Therefore, the extreme depolarization experienced at these stages is clearly shown by these polarimetric observables.

Up to the middle of the bulb growth stage, $\overline{\alpha}$ is mostly between 40° and 50°, while α_1 increases from a range of 10°–20° to a range of 20°–40°. This means that the dominant scattering mechanism corresponds to the scattering from anisotropic surfaces, i.e. a surface-type scattering where the term *anisotropic* refers to the difference, in terms of magnitude, between HH and VV. Then, as plants go in through the ripening stage α_1 decreases since a pure surface scattering starts to dominate the radar echo again.

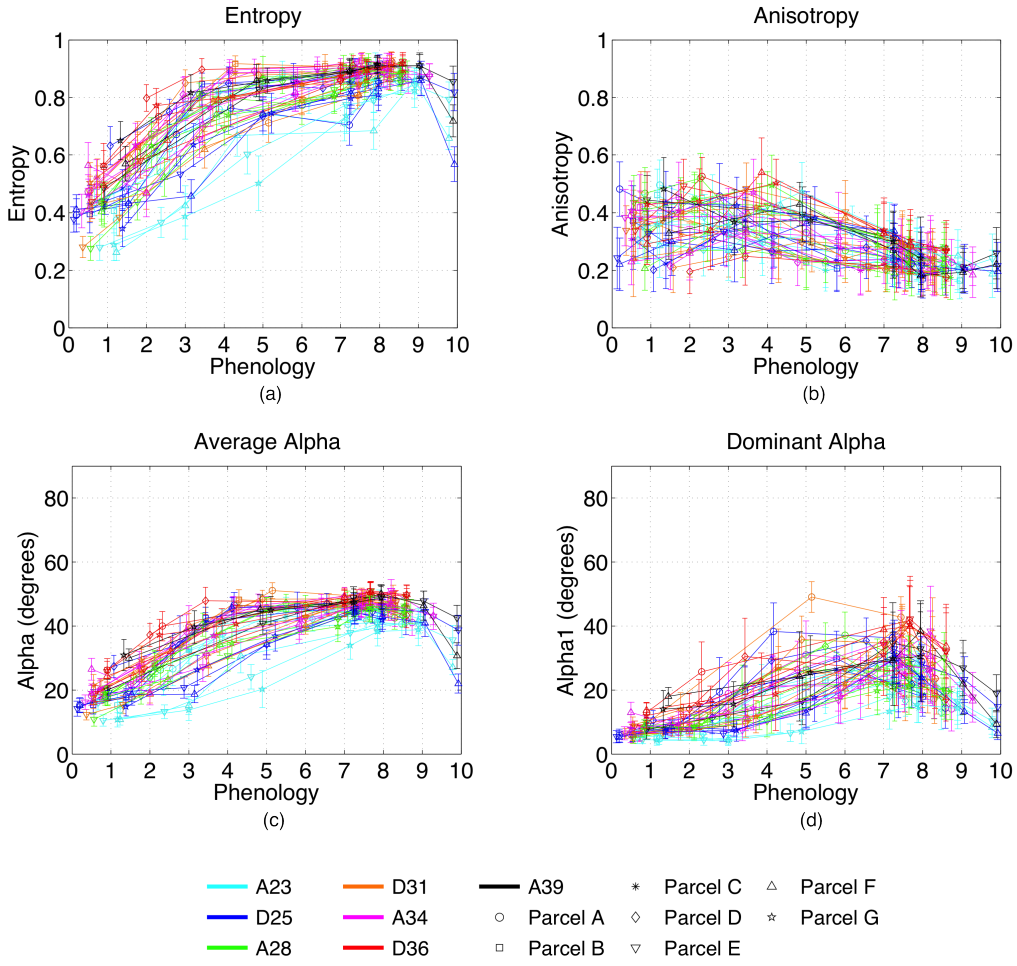

Figure 3.3: Evolution of the polarimetric observables extracted from the covariance matrix **T**. (a) Entropy; (b) Anisotropy, (c) $\overline{\alpha}$; (d) α_1.

Finally, in agreement with the copolar coherence, at the end of the pre-harvest stage we observe a larger decrease of both entropy and $\overline{\alpha}$ for parcel F with respect to parcel E. Regarding α_1, it is between 10° and 20° for parcel E and below 10° for parcel F. Hence, due to the time gap between the harvesting of the two parcels, only for parcel F we observe one scattering mechanism, i.e. surface scattering.

3.4.4 Retrieval of phenological stages

In this section both single-polarization and polarimetric observables are exploited to classify the phenological stages of onion fields. Since the single-polarization analysis showed that the HV channel is the most sensitive to the onion phenology, HH and VV channels will not furthered.

Three phenological intervals can be easily identified for onion fields. This corresponds to a partitioning of the whole vegetative phase reported in Table 3.2 into three main phases:

1. Early vegetative phase: from seeding to 2 leaves stage (phenological interval 0–2).
2. Middle vegetative phase: from 2/3 leaves stage to 6/7 leaves stage (phenological interval 2–6).
3. Advanced vegetative phase: from start of bulb growth to ripening/pre-harvest stages (phenological interval 6–10).

These intervals can be retrieved by defining a very simple classification algorithm.
It must be noted that, in order to obtain an estimation as correct as possible, none of the polarimetric observables can be used alone. Therefore, more of these parameters have to be combined in the retrieval procedure. In this study, the HV backscattering coefficient and the copolar coherence $|\rho_{\mathrm{hhvv}}|$ are used. The joint use of these two parameters allows to reduce ambiguities between the three phenological intervals. If $|\rho_{\mathrm{hhvv}}|$ is used alone, the early and the middle vegetative phases would be easily distinguished by its high values in the early vegetative phase, caused by the dominance of surface scattering. However, we would experience a total ambiguity between the middle and the advanced vegetative phases, due to decrease of this parameter with the foliage development occurring at these intervals (see figure 3.2(e)). To solve this issue, the high values of the HV backscattering coefficient in the advanced vegetative phase, driven by the extreme randomness of the foliage, provide a significant separation between these two classes. On the other hand, by using only the backscattered power at the cross polarized channel many ambiguities would be observed. Thus, the copolar coherence turns out to be fundamental to separate the first two phenological intervals in a better and consistent way.

In Fig.3.4(a) the plane defined by all the measured values (mean and standard deviation) of this pair of observables is shown, and the early, the middle and the advanced vegetative phase are colored in blue, green and red, respectively. Note that these three intervals are generally not overlapped. The mixing and overlapping values that we observe regard those days in which the radar response of the fields does not correspond to the expected interval, but to others. As a consequence, these points are expected to be misclassified. In some occasions, misclassifications are due to values very close to the transitions between phenological intervals. This is unavoidable since, usually, different zones of a field develop at different rates. In other words, such transitions are not so abrupt in nature.

The three phenological intervals are retrieved by considering the decision plane that is obtained by thresholding the $|\rho_{\mathrm{hhvv}}|$–HV space, as shown in Fig.3.4(b), where thresholds are set manually.

The algorithm is applied to all the available images and the classification is carried out at pixel level: for each image, a pixel is assigned to a phenological interval if it falls in the corresponding region identified in the $|\rho_{\mathrm{hhvv}}|$–HV decision plane. Those pixels that fall outside the three regions are not classified.

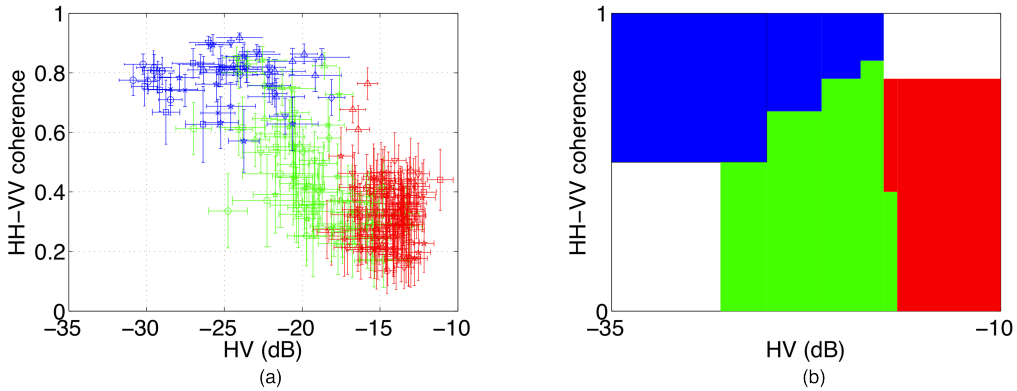

Figure 3.4: Scheme used to perform the classification of the three phenological intervals: (a)$|\rho_{\mathrm{hhvv}}|$–HV space and (b) corresponding decision plane. Color coding: blue: early vegetative; Green: middle vegetative; Red: advanced vegetative.

The performance of the estimation, carried out at the parcel level, is reported in Table 3.7 where the confusion matrix, relevant to all the parcels, is shown, along with the Overall Accuracy (OA), the Producer's Accuracy (PA), the User's Accuracy (UA) and the Kappa coefficient.

The OA is 86.23 % with Kappa = 0.78. We note that, while the early and the advanced vegetative phases are characterized by an high PA, the middle vegetative phase presents the worst PA, as a consequence of the higher number of misclassifications between this class and the others. Regarding the UA, it exhibits its lowest value in the middle vegetative phase.

It must be noted that other polarimetric observables can be used to estimate the three phenological intervals. In fact, if the entropy is considered (see Fig.3.3(a)), we note that the lowest values experienced in the early vegetative phase would allow to identify this phase. Regarding the middle and the advanced vegetative phases, it is evident that they cannot be estimated with the entropy alone. Therefore the HV backscatter is still needed to separate

these two classes. In table 3.8 the confusion matrix relevant to the estimation undertaken with this pair of observables is shown. The OA is slightly lower (about the 0.4 %) with respect to the $|\rho_{\mathrm{hhvv}}|$–HV case. This is a consequence of the larger number of misclassifications that is experienced between the middle and the advanced vegetative phases. These misclassifications give rise to a decrease of both the PA in the middle vegetative phase ($\sim$ 5 %) and the UA in the advanced vegetative phase ($\sim$ 2.5 %). Regarding the PA in the early and advanced vegetative phases and the UA in the early and the middle vegetative phases, the pair entropy–HV performs better than the pair $|\rho_{\mathrm{hhvv}}|$–HV.

Finally, inTable 3.9, the confusion matrix relevant to the estimation of these three phases by using only the HV backscattered power is reported. The classification is undertaken by thresholding the HV backscattering evolution shown in Fig.3.2(c). We note the worst OA, lower of about the 6 % with respect the ones of the $|\rho_{\mathrm{hhvv}}|$–HV and entropy–HV cases. This is practically due to the many misclassifications (20 cases out of 55) that occur between the early and the middle vegetative phases, that significantly lower the PA in the early vegetative phase, and the UA in the middle vegetative phase. In fact, in the first phase, the PA is lower of about the 30 and the 32 % with respect to the cases in which the HV backscattering is used jointly with the copolar coherence and the entropy, respectively. Concerning the UA, it is higher of about the 2,5 % than the $|\rho_{\mathrm{hhvv}}|$–HV/entropy–HV ones. In the middle vegetative phase, although the HV channel provides the best PA, the UA is lower of about the 16 % (20 %) than the ones provided by the pair $|\rho_{\mathrm{hhvv}}|$–HV (entropy–HV). Therefore, the backscattering at the HV channel provides the poorest result in the classification of all the three phenological intervals.

Table 3.7: Confusion matrix relevant to the phenology retrieval by using the pair $|\rho_{\mathrm{hhvv}}|$–HV.

		Ground data			
		Early	**Middle**	**Advanced**	UA (%)
Retrieval	**Early**	**51**	9	0	85
	Middle	4	**53**	6	84.13
	Advanced	0	15	**109**	87.9
	PA (%)	92.73	68.83	94.78	**OA**= 86.23 %

Kappa = 0.78

In summary, for the first time polarimetric SAR observables derived from C-band SLC quad-pol RADARSAT–2 images are used to estimate phenological stages of onion fields in the first

Table 3.8: Confusion matrix relevant to the phenology retrieval by using the pair entropy–HV.

		Ground data			
		Early	**Middle**	**Advanced**	UA (%)
Retrieval	**Early**	**52**	9	0	85,25
	Middle	3	**49**	4	87.5
	Advanced	0	19	**111**	85,38
	PA (%)	95,55	63,64	96,52	**OA**= 85.83 %

Kappa = 0.775

Table 3.9: Confusion matrix relevant to the phenology retrieval by using only the HV backscattering.

		Ground data			
		Early	**Middle**	**Advanced**	UA (%)
Retrieval	**Early**	**35**	5	0	87.5
	Middle	20	**55**	6	67.90
	Advanced	0	17	**109**	86.5
	PA (%)	63,63	71,42	94.78	**OA**= 80,56 %

Kappa = 0.688

year of growth. Three main phenological intervals are defined and a performance analysis is undertaken using both polarimetric observables and conventional intensity features. Experimental results show that the joint use of polarimetric features and the cross-polarized intensity results in the best retrieval of the three phenological intervals.

It would be interesting to estimate, in a future study, the phenological stages of onion during the second year of growth (reproduction and maturation phases) if both polSAR time series and ground measurements were available in this growing season.

3.5 Phenology retrieval of Oat fields

According to the world cereal production statistics, Oat (*Avena Sativa* L.) is at sixth rank after wheat, maize, rice, barley and sorghum [45]. Oat crops are primarily grown for livestock grain feed, fodder, hay and silage and are considered as good source of protein and fibre.

This section is focused on the estimation of phenological stages of oat fields monitored in Barrax within the framework of the AgriSAR 2009 field campaign.

In recent studies [32, 46] time series of RADARSAT–2 quad-pol data have been exploited

to analyze the polarimetric signature of oat fields along the growing season. In [46] the temporal evolution of both backscattering coefficients at linear polarization and polarization ratios relevant to oat, barley and wheat and other crop types has been evaluated in order to identify those acquisition dates and polarization configurations that maximize the crop separability. Regarding cereals crops, results shown that the HV allows to distinguish oat and wheat from barley when early heading occurs. In [32], apart from the backscattering coefficients, a set of polarimetric observables, i.e. the copolar phase difference and the outputs of both the eigenvalues/eigenvector and the Freeman-Durden decomposition [47], were analyzed to describe the scattering properties of oat, wheat, barley, canola and soybean in Ontario, Canada. Regarding oat, results shown that at the beginning of tillering the radar response was classified between surface and volume scattering in the H–$\overline{\alpha}$ plane [11] and by the Freeman-Durden decomposition. Then, toward the end of the cultivation cycle and after harvest the radar echo was dominated by volume and surface scattering, respectively.

Concerning the estimation of phenological stages of oat by means of full polarimetric SAR measurements, this issue has been recently addressed in [24, 30], where the time series of RADARSAT–2 quad-pol images collected over the Indian Head test site, in Canada, during the AgriSAR 2009 field campaign, has been exploited to derive phenological stages of different crop types including oat, barley, wheat, canola and pea. In [24], a simple supervised algorithm, consisting of an hierarchical tree based on two polarimetric parameters, i.e. α_1 and the Pauli_2 backscattering coefficient, was defined to retrieve cereals crops phenology at the pixel level. Four phenological intervals were estimated: 1) Early vegetative (BBCH 0–19); 2) Advanced vegetative (BBCH 20–44); 3) Reproductive (BBCH –79); 4) Maturation (BBCH 80–100). The validation, carried out at the parcel level, shown that the four intervals were properly estimated for barley and wheat with an high amount of right estimations. Concerning oat, the low sensitivity of the radar response to growth stages after the early vegetative phase did not allow distinguishing the last two intervals, resulting in the poorest result. In [30] a new methodology for phenology estimation, framed in the dynamical systems context, has been presented and tested over cereals fields, i.e. barley, oat and wheat. Six phenological intervals, that range from the early vegetative to the advanced maturation stages, were estimated by means of principal component analysis and an extended Kalman filter approach. Also in this case, the best results were obtained for barley and wheat, while oat provided low estimation accuracies due to the lack of sensitivity.

In this section, a supervised classification procedure, based on an hierarchical tree defined both at the parcel and at the pixel level, is first used to retrieve the phenological stages of oat fields. It is shown that, contrarily to [30] the polarimetric observables analyzed exhibit a sensitivity to growth stages of the parcels along the whole cultivation cycle.
Therefore, the contributes of this study are:

(1) The assessing of the sensitivity of the polarimetric response to the growth stage of this crop type cultivated in a different test site.

(2) Based on this sensitivity, the definition of an algorithm able to estimate phenology at two different scales, i.e. at the pixel and at the parcel one.

3.5.1 Ground truth

In Barrax, three oat fields, shown in Fig.3.5, were monitored during the AgriSAR 2009 field campaign. Regarding parcels A and B, they were analyzed in [38].
For this crop type, ten phenological stages, listed in Table 3.10, were recorded by the main set of ground measurements. According to the numerical scale provided in [13] for cereals, the *Seedling* stage should comprise *Germination* and *Seedling growth*. The latter consists of the leaf development phase [13]. Then, the *Start of tillering* and the *Tillering* stages clearly refer to *Tillering*, while *Start of stem growth*, *Stem growth* and *End of stem growth* correspond to the *Stem elongation* stage. Regarding the *Booting* stage [12, 13], it is not reported in the available ground truth and hence we may assume that it occurs in the end of stem growth stage. Finally, while the *Head emergence and flowering* stage should include both *Inflorescence emergence* and *Anthesis*, the succession *Kernel milk-dough/Kernel dough/Kernel hard* should comprise the *Milk development*, the *Dough development* and maybe the start of the *Ripening* stage. The approximate information concerning the last three stages will limit the interpretation of some polarimetric observables in the last part of the cultivation cycle.
Concerning the start/end dates of the stages listed in Table 3.10, also in this case they generally differ among the parcels, although some coincidences occur. The start date of seedling, common to the three parcels, is March 15 (DoY 74), while the end date of the kernel hard stage is July 14 (DoY 195) for parcels A and C, and July 15 (DoY 196) for parcel B. The harvest date, provided for the three parcels, is 23–24 July (DoY 204–205).
In analogy with the onion study, an *ad hoc* numerical scale, associated to the growth stages in Table 3.10, is defined according to the scheme shown in Table 3.11. According to this scale,

Figure 3.5: Oat parcels monitored in the AgriSAR 2009 field campaign in Barrax.

Table 3.10: Phenological stages of oat parcels provided by the main set of ground measurements.

Time window	Phenological stage
Start date_{STAGE_1} – End date_{STAGE_1}	$STAGE_1$: Seedling
Start date_{STAGE_2} – End date_{STAGE_2}	$STAGE_2$: Start of tillering
Start date_{STAGE_3} – End date_{STAGE_3}	$STAGE_3$: Tillering
Start date_{STAGE_4} – End date_{STAGE_4}	$STAGE_4$: Start of stem growth
Start date_{STAGE_5} – End date_{STAGE_5}	$STAGE_5$: Stem growth
Start date_{STAGE_6} – End date_{STAGE_6}	$STAGE_6$: End of stem growth
Start date_{STAGE_7} – End date_{STAGE_7}	$STAGE_7$: Head emergence and flowering
Start date_{STAGE_8} – End date_{STAGE_8}	$STAGE_8$: Kernel milk-dough
Start date_{STAGE_9} – End date_{STAGE_9}	$STAGE_9$: Kernel dough
Start $\text{date}_{STAGE_{10}}$ – End $\text{date}_{STAGE_{10}}$	$STAGE_{10}$: Kernel hard

reported in Table 3.12, the start of tillering and the tillering stages are grouped in an unique stage referred as $Stage_2$ (*Tillering*, phenological interval 1–2). Regarding the start of stem growth, stem growth and end of stem growth stages, they are referred as $Stage_3$ (*Stem growth*, phenological interval 2–3). Similarly, the kernel milk-dough, kernel dough and the kernel hard stages are grouped in the *Kernel development* stage ($Stage_5$, phenological interval 4–5). Finally, the harvest date provided allowed to define the *Pre-harvest* stage ($Stage_6$), corresponding to

the phenological interval 5–6.

Table 3.11: Scheme used to build the numerical scale associated to the phenological evolution of the oat parcels.

Start date$_{STAGE_1}$	→ 0	End date$_{STAGE_1}$	→ 1
Start date$_{STAGE_2}$	→ 1	End date$_{STAGE_2}$	
Start date$_{STAGE_3}$		End date$_{STAGE_3}$	→ 2
Start date$_{STAGE_4}$	→ 2	End date$_{STAGE_4}$	
Start date$_{STAGE_5}$		End date$_{STAGE_5}$	
Start date$_{STAGE_6}$		End date$_{STAGE_6}$	→ 3
Start date$_{STAGE_7}$	→ 3	End date$_{STAGE_7}$	→ 4
Start date$_{STAGE_8}$	→ 4	End date$_{STAGE_8}$	
Start date$_{STAGE_9}$		End date$_{STAGE_9}$	
Start date$_{STAGE_{10}}$		End date$_{STAGE_{10}}$	→ 5
		Harvest date	→ 6

3.5.2 RADARSAT–2 images relevant to oat parcels

The available RADARSAT–2 images collected over the Barrax area cover almost the entire cultivation cycle of the three oat parcels. In facts, since the growing season starts on March 15, the seedling stage is not covered by the SAR acquisitions. As a consequence, such a stage cannot be estimated in this study. According to the harvest date of the parcels, those SAR images acquired after July 21 are not considered. In addition, since, unlike the onion case, the three parcels are covered by all the beams, none of the beam is excluded from the analysis. Therefore, the time series of RADARSAT–2 SAR data consists of 33 images acquired from April 2 to July 21, and provides a revisit time ranging from one to six days. The phenological scale at the radar acquisitions is obtained by a linear interpolation.

Table 3.12: Phenology of the oat parcels described in terms of the numerical scale defined in Table 3.11.

Stage	Phenology	Numerical scale
$Stage_1$	Seedling	0–1
$Stage_2$	Tillering	1–2
$Stage_3$	Stem growth	2–3
$Stage_4$	Head emergence and flowering	3–4
$Stage_5$	Kernel development	4–5
$Stage_6$	Pre-harvest	5–6

3.5.3 Analysis of polarimetric observables

In this section, the sensitivity of polarimetric observables to the phenological stages of the oat fields under study is investigated. Such parameters are divided in two main sets: the first set, shown in Fig.3.6, comprises those observables derived from the covariance matrix **C**; the second set, shown in Fig.3.7, consists of the polarimetric observables extracted from the coherency matrix **T**.

3.5.3.1 Backscattering coefficients at linear polarizations and polarization ratios

The evolution of the backscattering coefficients at the copolar channels is shown in Fig.3.6(a)-(b). In the tillering stage (1–2) the HH and the VV channels exhibit a similar trend, with a level ranging between -12 and -8 dB. As a consequence, the HH/VV ratio, shown in Fig.3.6(d), ranges between -1 and ∼-1.5 dB. The higher values of backscattering at both channels (around -6 dB) experienced by beams D25 and A28 for parcel B at the start and the middle of the tillering stage are due to irrigation. In facts, the irrigation schedule provided for this parcel reports that, when both the D25 and the A28 images were acquired (April 3–DoY 93, and April 16–DoY 106, respectively) the field was irrigated with an amount of water of 3.3 mm and 6.65 mm, respectively.

During the stem growth stage (2–3), while the backscattering at the HH channel decrease of about 3 dB, the decrease at the VV backscattering is around 6 dB. This is due to the vertical extension of the plants, that attenuates more the VV channel with respect the HH one. Accordingly, the copolar ratio increases up to 5 dB.

Regarding the head emergence and flowering stages (3–4), the lack of images does not allow to provide a physical interpretation. In facts, only one image, corresponding to beam D36, falls

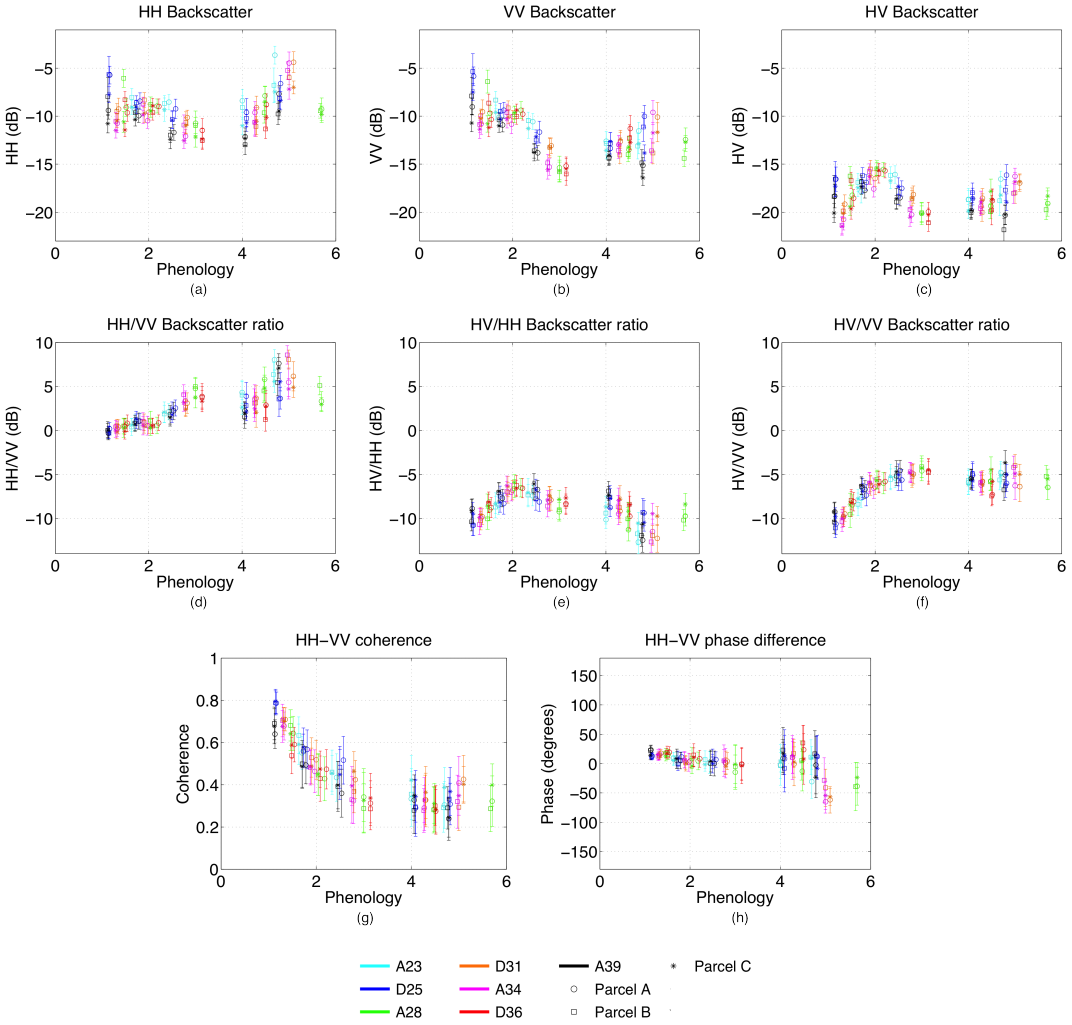

Figure 3.6: Evolution of the polarimetric observables extracted from the coherency matrix **C**. (a)-(c) HH, VV and HV backscattering coefficients; (d)-(f) HH/VV, HV/HH and HV/VV; (g)-(h) Copolar coherence and phase difference.

between stages 3 and 4 and, in this case, the backscattering coefficient for both the copolar channels follow the trend of the previous stage.

In the first half of the kernel development stage (4–4.5) the HH (VV) backscattering coefficient lies mainly between -12 and -8 (-14 and -12) dB, while it increases of about 4 (2) dB as plants reach the end of this stage. This last increase is due to the fact that leaves and branches are dryer with respect to the previous stages. Therefore, since the radar penetrates more the foliage, we observe both an higher backscattering from the ground and the double-bounce scattering mechanism caused by the interaction between the stems and the ground. Such a double-bounce

imposes a larger attenuation on the VV return with respect to the HH one. Hence, the coploar ratio reach its maximum level around stage 5 ($\sim$ 9 dB).
Toward the end of the pre-harvest stage the HH (VV) backscattering coefficients decreases, on average, of about 4 (1) dB, due to the fact that stems are dryer with respect to the previous stage.

Regarding the backscattering at the HV channel, shown in Fig.3.6(c), it increases of about 5 dB in the tillering stage, due to the increasing amount in the above-ground vegetation (tillers). Then, in the stem growth stage, the cross-polarized echo decreases to values around -21 dB, as consequence of the vertical orientation of the plants at this stage.
From stage 4 to 5 the HV backscattering coefficient is mostly between -20 and -18 dB, exhibiting a slight increase ($\sim$ 2 dB) toward stage 5. Such an increase can be attributed to the structure of the plants at this stage. In facts, unlike other cereals crops, such as barley and wheat, oat heads consist of open panicles that tend to bend at this stage, thus increasing the amount of randomness in the canopy layer.
The final decrease of the HV backscattered power ($\sim$ 2 dB for parcels A and B, and around 1 dB for parcel C) can be justified by the further drying of the canopy.

Finally, concerning the cross-polarized ratios (Fig.3.6(e)-(f)), their evolution is dictated by the trends of the HH and VV channels commented above.

3.5.3.2 Coherence between copolar channels and copolar phase difference

Fig.3.6(g)-(h) show the evolution of $|\rho_{\mathrm{hhvv}}|$ and ϕ_{hhvv}. Concerning the copolar coherence, it is characterized by high values (mostly above 0.5) during the tillering stage, due to the dominance of the scattering from the ground in the radar echo. Then, as plants develop, $|\rho_{\mathrm{hhvv}}|$ decreases to low values (mainly below 0.4). Regarding the behavior of the copolar coherence in the pre-harvest stage, we should observe an increase of this parameter due to the dominant surface scattering caused by the total desiccation and collapsing of the plants, since the last acquisition occurred two-three days before harvesting. Contrarily, $|\rho_{\mathrm{hhvv}}|$ is still low. A possible explanation is that plants were harvested before they were dead and collapsed, i.e. when the backscattering from the stems is not negligible. Unfortunately, the limitations imposed by the lack of more ground information do not allow to fully interpret last stage. Regarding ϕ_{hhvv}, according to the copolar coherence evolution, it remains mostly around 0° up to the end of the kernel development stage. Then, around stage 5, it significantly decreases, even reaching values

around -65°, due to the aforementioned double-bounce scattering mechanism. Although in the last stage the CPD slightly increases, it is still below zero.

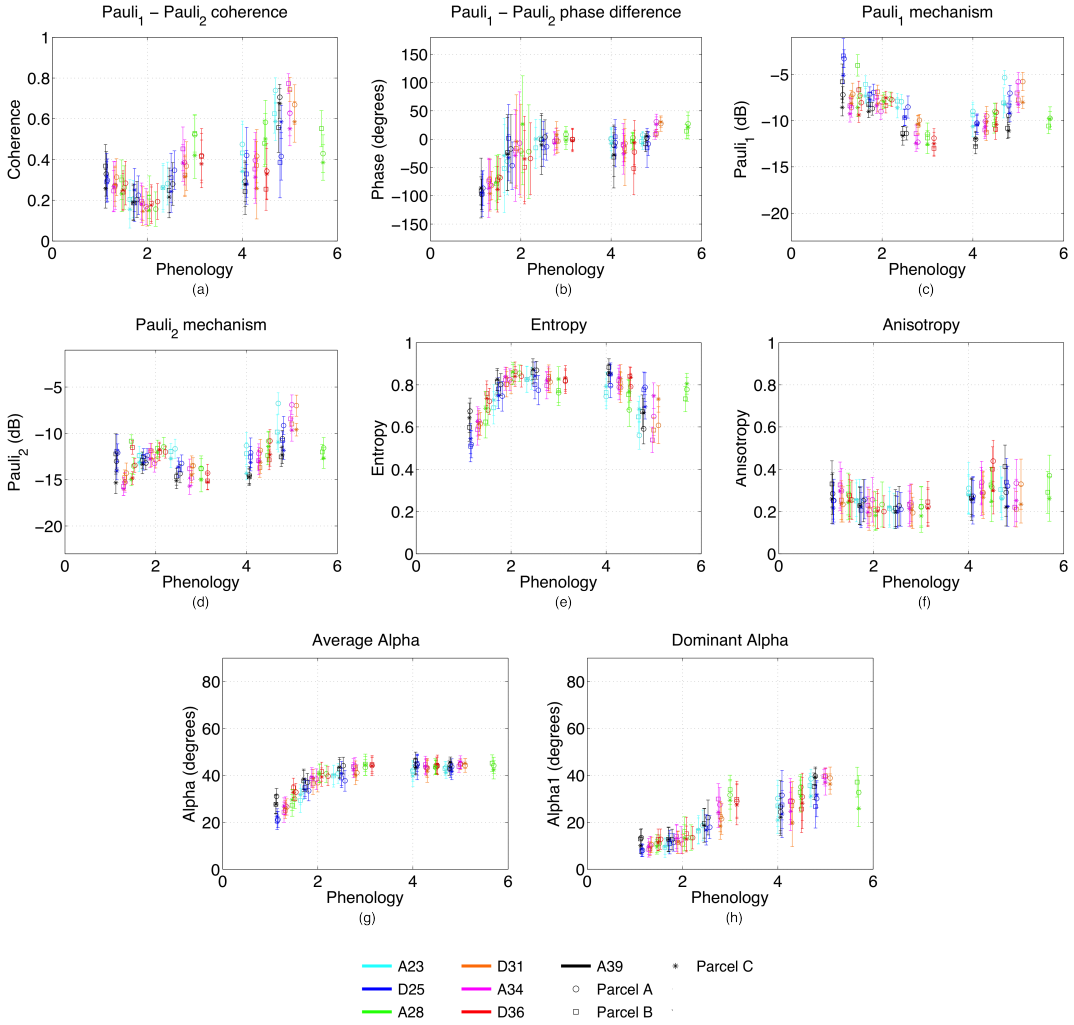

Figure 3.7: Evolution of the polarimetric observables extracted from the coherency matrix **T**. (a)-(b) Pauli coherence and phase difference; (c)-(d) Pauli_1 and Pauli_2 backscattering coefficients; (e) Entropy; (f) Anisotropy; (g) $\overline{\alpha}$; (h) α_1.

3.5.3.3 Pauli coherence and phase difference and backscattering coefficients at the Pauli channels

In Fig.3.7(a)-(d) the evolution of the Pauli coherence $|\rho_{\text{p}}|$, the phase difference between the Pauli channels ϕ_{p} and the backscattering coefficient at the Pauli_1 and Pauli_2 channels, is shown.

In the tillering stage, due to the high correlation between the copolar channels, the first and

the second Pauli channels exhibit a low correlation ($|\rho_p|$ below 0.4-0.3). Therefore, their amplitudes are very different, resulting in an higher backscattering coefficient at the first Pauli channel with respect to the second one, thanks to the dominance of the direct scattering from the ground (single-bounce type scattering). However, the backscattering level at the $Pauli_2$ channel increases of about 4 dB, driven by the increasing amount of the tillers. Such a behavior is similar to the one experienced by the HV backscattering (third Pauli channel) commented before.

In the stem growth stage, as a consequence of the significant attenuation of VV channel with respect the HH one, the first two Pauli channels start to be correlated and hence the Pauli coherence exhibits an increase reaching values above 0.5. Regarding the $Pauli_1$ and $Pauli_2$ backscattering coefficients, their decrease (~ 5 and ~ 4 dB, respectively) is due to the attenuation of the soil backscattering caused by the foliage and the attenuation imposed by the vertical orientation of the plants, respectively.

From stages 4 to 4.5, $|\rho_p|$ exhibit large variations between 0.2 and 0.6 and then it reaches its highest value (~ 0.8) around stage 5. Such an in crease is due to the double-bounce between the ground and the stems, commented before. In facts, being the HH backscattering coefficients much larger than the VV one, the two Pauli channels are both similar to HH, and hence highly correlated. Accordingly, the $Pauli_1$ and $Pauli_2$ backscattering coefficients are around -6 and -7 dB, respectively.

In the pre-harvest stage, although the Pauli coherence exhibits a decrease, it is mainly above 0.4. Concerning the $Pauli_1$ and $Pauli_2$ backscattering coefficients, they decrease of ~ 4 and ~ 5 dB, respectively. The decrease of the $Pauli_2$ backscattering coefficient, along with the negative CPD experienced at this stage, may be due to the dominance of the two-way propagation through the vegetation layer.

Regarding the phase difference between the Pauli channels, it increases from values below -100° to values close to 0° between stages 1 and 2.5. Then, it remains mainly around zero (except some values below -50°) in the the kernel development stage, while it increases to values around 30° in the pre-harvest stage.

3.5.3.4 Eigenvalue/Eigenvector decomposition

The outputs of the eigenvalue/eigenvector decomposition are shown in Fig.3.7(e)-(h), respectively. Regarding entropy, it increases from ~ 0.5 to ~ 0.85 in the tillering stage. The high entropy values at the end of tillering denote, together with a low anisotropy (always below 0.4),

the presence of three scattering mechanisms: the scattering from the ground, the double-bounce interaction between ground and tillers and the scattering from the tillers. $\overline{\alpha}$ increases up to 40°, while the low values of α_1 (below 20°) witness that the dominant scattering mechanism is the one from the ground.

In the stem growth stage the entropy remains high, while $\overline{\alpha}$ approaches to 45°. Concerning α_1, it is below 40°. Then, from the start to the middle of the kernel development stage, entropy is mainly between 0.7 and 0.9, while, especially for parcels A and B at higher incidence angles, it drops to lower values (until ~ 0.5) in the second half of the stage. Such low values of entropy, along with $\overline{\alpha} \sim 45°$ and α_1 below 40°, denote, in these cases, that the radar echo is characterized by a single scattering mechanism: the dipole-like scattering due to the double-bounce effect that is observed.

Finally, the high values of entropy (between 0.7 and 0.85) in the pre-harvest stage may be the consequence of further scattering mechanisms caused by the aforementioned two-way propagation through the vegetation layer.

3.5.4 Retrieval of phenological stages

The polarimetric observables described in the previous section are exploited to estimate the phenological stages of the three oat fields parcels.

In this case, five phenological intervals are identified:

(1) Early vegetative: from the beginning to the middle of the tillering stage (phenological interval 1–1.55).

(2) Middle vegetative: from the middle of the tillering stage to beginning of stem growth (phenological interval 1.6–2.2).

(3) Advanced vegetative/early reproductive: from beginning of stem growth to the beginning of head emergence and flowering (phenological interval 2.3–3.5).

(4) Early maturation: beginning of kernel development (phenological interval 4–4.35).

(5) Late maturation: from the middle of kernel development to pre-harvest (phenological interval 4.4–6).

Note that, since each parameter, if used alone, would give rise to ambiguous estimations, also in this case a proper set of observables has to be used.

The estimation is based on an hierarchical tree, shown in Fig.3.8, that is applied both at the parcel and at the pixel level. At the parcel level, the standard deviation of the following parameters is used: ϕ_{p}, ϕ_{hhvv} and α_1. At the pixel level, the evolution of both the HV/VV ratio and the backscattering coefficient of Pauli_2 channel is considered. The use of these parameters provides an effective estimation of the above phenological intervals. In facts, according to the highest values of the copolar coherence experienced at the first two intervals caused by the dominance of surface scattering, the small standard deviation of ϕ_{hhvv}, along with the level of HV/VV ratio, allows the estimation of such intervals at the pixel level. Note that the second interval is also estimated at the parcel level by the standard deviation of ϕ_{p} and α_1, since, at this stage, the Pauli coherence assume its lowest values (largest standard deviation of the phase) and the standard deviation the dominant alpha angle is low. Concerning the third phenological interval, according to the higher values of the Pauli coherence (lower standard deviation of ϕ_{p}) and the lower values of copolar coherence (higher standard deviation of ϕ_{hhvv}), it is estimated both at the parcel and at the pixel level. At the pixel level, the low values of the Pauli_2 backscattering coefficient caused by the vertical orientation of the plants in this interval are considered, while at the parcel level the standard deviation ϕ_{p} is used. The fourth interval is estimated only at the parcel level by considering the highest standard deviation of α_1 experienced at this stage, and the standard deviation of the Pauli phase difference. Finally, the last stage is estimated at the pixel level by means of the higher values of the Pauli_2 backscattering coefficient commented before, and at the parcel level by means of the ϕ_{p} standard deviation.

It is important to point out that, since the standard deviation of parameters involved in the estimation are affected by the size of the multi-look window, if a different window size is used thresholds would change.

The output of the algorithm is presented in Fig.3.9, where a mosaic with the retrieval results relevant to the three parcels is shown.

The estimation performance is reported in Table 3.13, where the confusion matrix is shown, along with the OA, the PA, the UA and the Kappa coefficient. We can appreciate the quite high classification accuracies and the high value of Kappa. Such results are in net contrast with the ones obtained in [30] for oat fields, where only three phases out of six, i.e. the early vegetative, the middle vegetative and the advanced maturation phases, where estimated with appreciable accuracies, thus resulting in a OA equal to 53 % and a value of Kappa below 0.4. This is practically due to the different part of the worlds (e.g. characterized by different soils and the

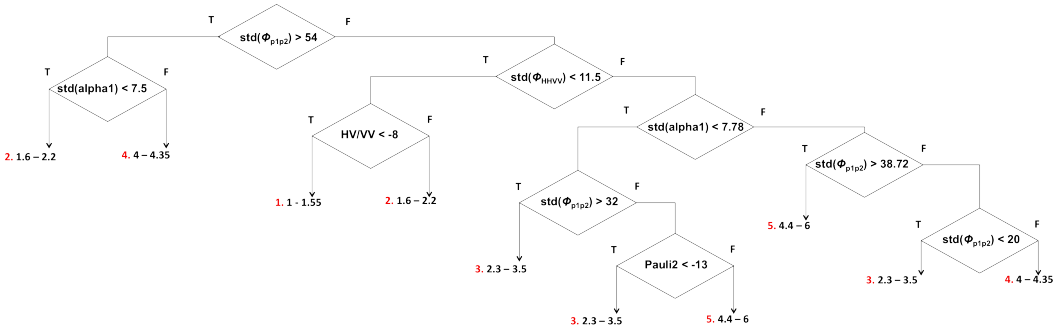

Figure 3.8: Hierarchical tree employed for the phenology retrieval.

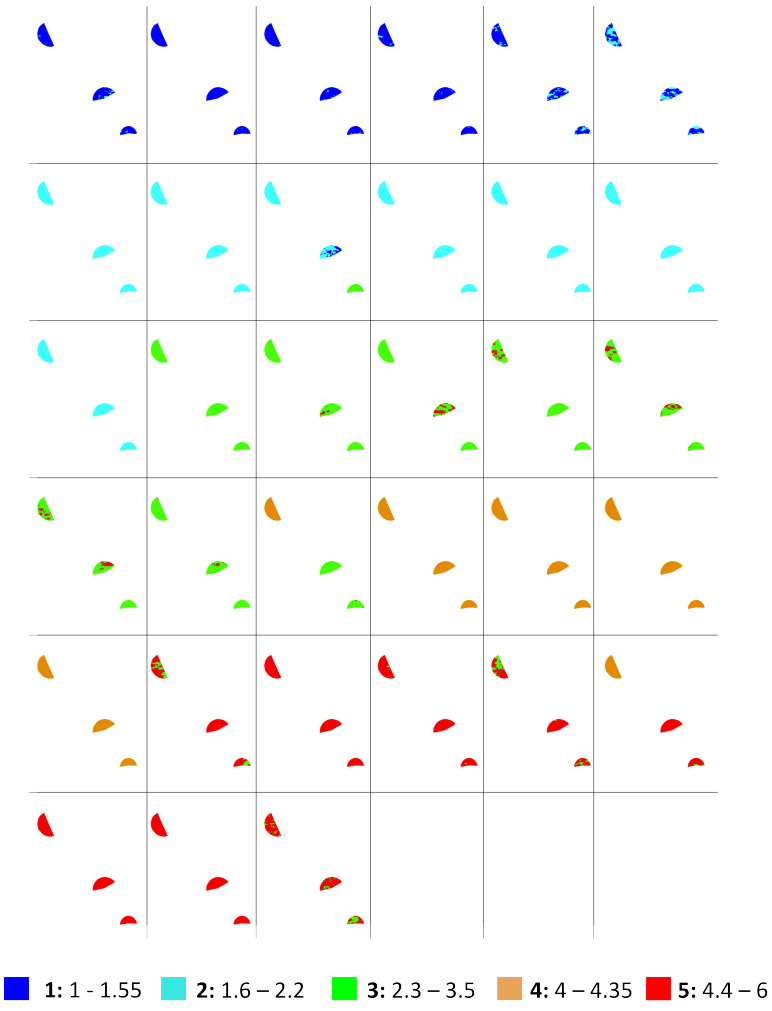

Figure 3.9: Mosaic of the retrieval results for the three parcels.

use of different types of seeds) in which the oat fields analyzed in [30] and in the present study are cultivated and, most likely, to the different cultivation practices they are applied. Such differences can give rise to different development of the same crop type and hence to different polarimetric signatures during the cultivation cycle.

Table 3.13: Confusion matrix relevant to the phenology retrieval.

		Ground data					
		Class 1	**Class 2**	**Class 3**	**Class 4**	**Class 5**	UA (%)
Retrieval	**Class 1**	**17**	5	0	0	0	100
	Class 2	1	**20**	0	0	0	95.23
	Class 3	0	1	**21**	0	0	87.25
	Class 4	0	0	0	**13**	1	92.85
	Class 5	0	0	0	0	**23**	100
	PA (%)	94.44	95.23	100	86.66	95.83	**OA**= 94.94 %

Kappa = 0.936

In summary, five phenological intervals of oat fields present in Barrax are estimated by means of a set of polarimetric observables. A supervised classification scheme applied, both at the parcel and at the pixels level, is used for the estimation. Both the sensitivity and the high estimation accuracies are in contrast with a literature study undertaken on oat fields present in a different test site.

3.6 Conclusions

In this chapter, polarimetric observables extracted by a time series of C-band RADARSAT–2 quad-pol SAR data acquired over Barrax during the AgriSAR 2009 field campaign, have been exploited to estimate the phenological stages of both onion and oat fields.
The estimation is based on the physical interpretation of these observables in terms of the phenological stages. Such an interpretation allowed to define supervised algorithms, consisting of hierarchical trees and decision planes, that are used for the phenology retrieval.

Concerning onion fields, the estimation of the phenological stages by means of polSAR data has been first addressed in this study. It has been shown that conventional observables, such as the backscattering coefficient at the cross-polarized channel, provide the best results only if used jointly with polarimetric observables, i.e. copolar coherence or entropy. In facts, the physical interpretation of these two observables in the early vegetative phase, i.e. the presence

of a single scattering mechanism that is a surface-type one, allows obtaining the best estimate of such a stage by coupling them with the HV channel intensity. The latter is important to distinguish the last two stages, due to the increasing randomness of the structure of this crop type as it develops.

In the case of oat fields, an appreciable sensitivity of the polSAR observables is experienced from the start to the end of the cultivation cycle. This is in contrast with recent studies undertaken on different test sites, which report a lack of sensitivity for oat after the early stages, thus leading to poor result in the phenology retrieval. This discrepancy, that is practically due to the different test sites and the different cultivation practices that give rise to changes in the plants evolution, leads to the conclusions that this sort of analysis has to be adapted locally to each test site.

Regarding the phenology retrieval, five phenological intervals have been estimated in a very effective way at two different scales, i.e. pixel and parcel level, by means of an hierarchical tree that involves:

(1) The standard deviation of the phase differences, both the copolar and the Pauli one. These parameter is related to the high/low values of the corresponding coherences experienced at certain stages according to the plants morphology.

(2) The standard deviation of the dominant scattering mechanism, that is low in the early growth stages and exhibits an increase in the successive ones.

(3) The Pauli_2 backscattering, characterized by a low level in the stem growth stage which increases in the later stages.

(4) The HV/VV ratio, whose values are quite low at the earliest growth stages.

3.7 Acknolodegment

This work was partially supported by the Spanish Ministry of Economy and Competitiveness (MINECO) and EU FEDER, under Project TEC2011-28201-C02-02. All RADARSAT-2 images were provided by ESA in the framework of the AgriSAR2009 campaign. RADARSAT-2 Data and Products © MacDonald, Dettwiler and Associates Ltd. (2009) – All Rights Reserved. RADARSAT is an official trademark of the Canadian Space Agency.

4

Multi–polarization COSMO-SkyMed SAR data for land cover discrimination

4.1 Introduction

COSMO-SkyMed (CSK) is a technologically advanced Earth Observation (EO) space system, commissioned and funded by the Italian Space Agency (ASI) and the Italian Ministry of Defence, which consists of four Low Earth Orbit mid-sized satellites equipped with X-band SAR instruments. The CSK system has significant advantages. The first one is its dense revisit time which is lower than 12 hours [48]. The second one is the capability of the SAR instrument to operate in different imaging modes: Spotlight, Stripmap and ScanSAR. Spotlight mode (conceived for both civilian and defense use) allows achieving metric spatial resolution over small areas. Stripmap mode allows achieving metric spatial resolution over wide swath and foresees two different implementations: the Himage and the incoherent dual-polarization PingPong mode. ScanSAR mode allows a very large coverage and can be implemented in two different configurations, WIDE and HUGE region, providing different swath size and a medium to coarse spatial resolution. A further advantage of the CSK system is the capability to acquire interferometric image couples (two satellites operating in tandem configuration) which allows the generation of Digital Elevation Models (DEM) whose accuracy depends on the imaging mode. Hence, due to its peculiarities, CSK is very attractive for several EO applications including land areas monitoring and coastal and ocean monitoring.

Within this framework, some studies have exploited CSK SAR images in order to discriminate different land cover types. In [49] a land/sea discrimination is achieved using CSK Level 1A Single Look Complex Slant (SCS) PingPong mode HH/VV SAR data. The modulus of the correlation between the co-polarized HH/VV complex channels is used to effectively distinguish land from sea and then to extract the continuous coastline. In [50] and [51], CSK PingPong mode SAR data are used for classification of a suburban areas and crop classification, respectively. A supervised land cover classification approach, based on the use of CSK interferometric SAR (InSAR) data acquired in HH/HV PingPong mode is proposed in [52] to delineate land cover classes such as water bodies, urban and vegetated areas.

In this chapter the issue of land cover discrimination is addressed by exploiting the multi-polarization capabilities of the CSK system. In a first study, land is discriminated from sea and the coastline, i.e. the boundary between sea and land, is detected. In successive study, sea areas are distinguished from urban and vegetated ones.

The contents of this chapter is based on papers published at international journals and presented at international conferences [53–56].
The chapter is organized as follows. In section 4.2 [54], single-polarization CSK SAR data, acquired both at the co- and at the cross-polarized channels, are effectively used to separate land from sea, on the base of a multi-polarization analysis of the X–band sea surface backscattering. Then, the continuos coastline is detected. In section 4.3 [53, 55, 56], the peculiarities of the CSK incoherent dual-polarization PingPong mode are first exploited to distinguish between sea, vegetated and urban areas. In particular, dual-polarization features derived from the PingPong mode, along with the single-pol ones, are used and their sensitivity to different sea state conditions, different types of vegetation and different types of urban scenarios are also investigated.

4.2 Land/sea discrimination based on a multi–polarization analysis

In this section, CSK SAR data, collected using the single-polarization Himage Stripmap mode, are exploited to distinguish land from sea for coastline extraction purposes.

Coastline observation is of paramount importance for several applications including safe shipping navigation and coastal zone management, i. e. management of areas that are economically and environmentally important, such as harbors, fisheries, oil and gas fields, tourist sites,

wildlife habitats, etc. [57], [58].
Within the framework of satellites remote sensing systems, SAR sensors are the most effective tools for coastal detection, due to their capability in guaranteeing all-day and almost all-weather observations characterized by a fine spatial resolution [49, 59, 60]. Therefore, the CSK space system turns out to be very tailored for such a topic. Moreover, the use of high frequencies, such as the X–band, is recommended for an accurate coastline detection. However, SAR-based coastline extraction is a very challenging task due to: a) speckle noise, i. e. multiplicative noise that hampers SAR image interpretability; b) the lack of land/sea contrast that, in addition, depends on both sea state condition and land type [49], [61].

In this study, the capabilities of X-band CSK single-polarization Himage Stripmap mode SAR data in separating land from sea are analyzed for coastline extraction purposes. Land/sea discrimination is addressed in two steps. The first step consist of a multi-polarization study, undertaken to analyze co- and cross-polarized X–band sea surface scattering for different incidence angles (AOIs) and sea state conditions. Then, in the second step, a global threshold Constant False Alarm Rate (CFAR) algorithm, based on an exponential sea clutter distribution, is developed to obtain a binary image where sea areas are separated form the land ones. The performance of the proposed approach is discussed using actual HH and HV CSK SAR data collected under different AOIs and wind conditions. Finally, once the binary image is obtained, the 1-pixel continuous coastline is extracted by applying a conventional edge detector based on the Sobel kernel.
Hence, the contribute of this study is the development of a simple and effective procedure that, based on the exploiting X-band CSK single-polarization SAR data acquired at different polarizations, is aimed at distinguish land from sea with the final objective of coastline extraction.

4.2.1 Theoretical Background

In this section the theoretical rationale which lies at the basis of the proposed land/sea discrimination approach is briefly outlined.

In first place, X-band sea and land backscattering must be accounted for. When dealing with sea surface, under low-to-moderate wind conditions and for intermediate incidence angles, the dominant scattering mechanism is governed by Bragg or tilted-Bragg [62]. Hence, sea surface backscattering is mainly related to the small-scale (wind-dependent) roughness, modulated by the large-scale wave structure in a both linear and non-linear way [63]. To analyze the X-band multi-polarization sea surface backscattering under low-to-moderate wind conditions, an

improved version of the Integral Equation Method (IIEM), is used [64]. Accordingly, the NRCS for a transmitting/receiving polarization couple $pq = \{h, v\}$ is given by [65]:

$$\sigma^s_{qp} = S(\theta, \theta_s)\frac{k^2}{2} exp[-\sigma^2(k_z^2 + k_{sz}^2)] \sum_{n=1}^{N} \sigma^{2n} |I^n_{qp}| \frac{W^{(n)}(k_{sx} - k_x, k_{sy} - k_y)}{n!} , \qquad (4.1)$$

where k is the electromagnetic wave number, $k_x = ksin\theta cos\phi$, $k_y = ksin\theta sin\phi$ and $k_z = kcos\theta$ are defined in terms of the incident direction identified by the angles θ and ϕ, while k_{xs}, k_{ys} and k_{zs} are similarly defined in terms of the scattering angles θ_s and ϕ_s. Furthermore, σ is the surface rms height, $W^{(n)}$ is the Fourier transform of the n^{th} power of the surface correlation coefficient, $S(\theta, \theta_s)$ is a bistatic shadowing function, I^n_{qp} is a compact form term accounting for the field coefficients f_{qp} and ! stands for factorial [65].

The HH, VV and HV NRCS, obtained using an exponential correlation function in both high and low-to-moderate sea state conditions, are shown in Fig.4.1(a)-(b). Low-to-moderate sea state conditions result in exponential correlation function with a correlation length equal to 0.5 m and a rms height equal to 0.00103 m, see Fig 4.1(a). High sea state condition is characterized by an exponential correlation function with a correlation length equal to 0.1 m and a rms height equal to 0.00469 m (see Fig.4.1(b)). It can be noted that, as expected, the HV NRCS is significantly lower (from $\approx$ 10 dB to $\approx$ 30 dB at intermediate AOI) than the co-polarized ones; while HH and VV backscatterings are very close to each other up to an AOI equal to $\approx 25°$. Moreover, the VV backscattering is slightly larger than the HH one for larger AOI. It must be explicitly pointed out that a different behaviour may be in place when departures from Bragg scattering apply [66, 67].

When dealing with land backscattering, due to its heterogeneity, the scattering behavior strongly depends on the type of scenario. Hence, a theoretical modeling is not straightforward. In case of bare soil and sandy terrain, the dominant scattering mechanism is a Bragg-like one, and the related backscattering intensity strongly depends on several factors such as soil moisture level and AOI. This implies that sandy areas or bare soils may be challenging to be discriminated from sea surface. In case of urban areas, the dihedral and diffuse scattering mechanisms are expected that result in a stronger and more persistent backscattered signal, while in case of vegetated areas, the backscattering strongly depend on the vegetation type and on the canopy.

The above-described theoretical considerations suggest investigating the land/sea discrimination using both co- and cross-polarized channels, under low-to-moderate wind conditions. To generate a logical true (land) and false (sea) output in a partially unsupervised way, the sea

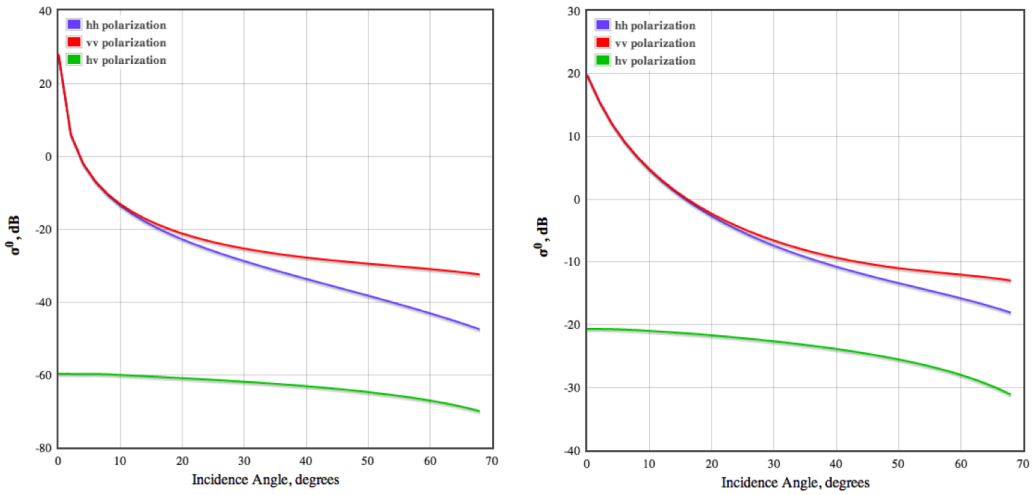

Figure 4.1: X-band sea surface HH, VV and HV NRCS predicted using IIEM for different sea state conditions (surface rms height and correlation length) and for incidence angles up to 68°. The real and imaginary part of the sea dielectric constant are 50.1 and 35.5, respectively, for a surface temperature equal to 18°C and a salinity equal to 38 psu. (a) Low-to-moderate sea state condition; (b) High sea state condition.

clutter distribution is analyzed. In case of Bragg scattering, sea surface backscattering intensity is well-modeled by an exponential distribution [63]. Hence, the following model is adopted:

$$p(x) = \frac{1}{\sigma} exp\left(-\frac{x}{\sigma}\right), \; x \geq 0 \; , \tag{4.2}$$

where x is the field intensity and σ is the distribution mean value. To generate the binary image, a CFAR detector, based on a global threshold th, is proposed. The relationship between the detection threshold th and the false alarm rate P_{fa} is given by [68]:

$$\Gamma\left(\left(\frac{th}{\sigma}\right), 1\right) = 1 - P_{fa} \; , \tag{4.3}$$

where $\Gamma(\cdot, \cdot)$ is the incomplete Gamma function [69]. Therefore, inverting (4.3) the following threshold is obtained [68], [69]:

$$th = -\sigma ln(P_{fa}) \; . \tag{4.4}$$

The final step consists of extracting the 1-pixel continuous coastline from the binary output. This is addressed by using a conventional Sobel edge detector. Several edge detection algorithms have been proposed in [60, 61, 70]. The Sobel filter allows achieving the desired result in a simple and effective way [71]. It performs a 2-D spatial gradient measurement on the binary output, emphasizing high spatial frequency regions, i.e. edges. For further details see [71]. Once edges are extracted from the binary output, the 1-pixel continuous coastline is obtained.

4.2.2 Experiments

In this section the effectiveness of the proposed approach is discussed using actual CSK SCS Stripmap Himage SAR data.

The CSK data set, see Table 4.1, consists of four CSK Stripmap Himage SAR scenes, characterized by a 3 x 3 m spatial resolution and a large swath ($\approx$ 40 x 40 km). Such data were collected in the Gulf of Naples and the in the Gulf of Cape Town. Wind speed information, obtained by [72], is listed in Table 4.1.

For each scene a pre-processing is undertaken, which consists of reprojecting the SAR scene (UTM) and selecting a Region Of Interest (ROI) of 500×500 pixels that is used to estimate the parameter of the exponential distribution in (4.2) and to evalutate *th* from (4.4). Then, the binary image corresponding to the processed SAR scene, is obtained by applying a CFAR detection with the global threshold (4.4) for $P_{fa} = 10^{-4}$. Once the binary image is obtained, isolated clusters (i.e. metallic targets at sea) that consist of less than T pixels are filtered out. In this study, T = 12000 is considered that accounts for both the CSK spatial resolution and the typical size of isolated clusters. Finally, the 1-pixel continuous coastline is extracted using a conventional Sobel edge detector.

Table 4.1: CSK data set

Experiment	Scene	Size (Pixels)	Acquisition date and Time (UTC)	Polarization	Incidence angle (°)	Wind speed (m/s)
Exp.1	Gulf of Naples	3419 x 2494	06/09/2010 18:05:58	HV	53.2 - 54.7	2.1
Exp.2	Gulf of Naples	8557 x 15278	16/09/2010 17:53:53	HV	38.6 - 41.5	2.6
Exp.3	Gulf of Cape Town	8097 x 6513	13/12/2013 15:56:49	HH	36.1 - 38.8	11.3
Exp.4	Gulf of Naples	5908 x 4476	01/11/2009 05:10:00	HH	48.6 - 50.6	1.0

The first experiment is relevant to the CSK HV-polarized SAR scene collected on September 6, 2010, at 18:06 UTC, in the Gulf of Naples (see Exp.1 in Table 4.1). An excerpt (3419×2494 pixels) of the whole SAR scene is processed, see Fig.4.2(a). The considered area includes a small portion of the "Penisola Sorrentina", an area characterized by a rocky and vegetated coastal

profile, see Fig.4.2(b).

First, the mean Land-to-Sea NRCS Ratio (LSR) is analyzed over two equal-size (500×500 pixels) ROIs, in order to better assess the coastline extraction capabilities. LSR, evaluated over the two ROIs of Fig.4.2(a), is equal to 6.05 dB (see Table 4.2). It can be noted that LSR is smaller than expected for a cross-polarized channel: this is probably due to the high AOI ($\approx 54°$) and the mostly vegetated nature of the land area.

The empirical sea distribution and the theoretical exponential one are shown in Fig.4.4(a). The Kolmogorov-Smirnov binary hypothesis test, performed for a significance level of 0.05, confirms the soundness of the exponential model adopted. The same test is used in all the subsequent experiments. The evaluated σ value, estimated from (4.2) as mean value of the sea ROI, is equal to 0.0101 and the corresponding exponential-based global detection threshold (4.4) is equal to $th = 0.0934$. These numbers are listed in Table 4.2. By using this threshold, the binary output of Fig.4.3(b) is obtained, where isolated clusters less than T pixels have been filtered out. It can be noted that there is a black hole in the upper-side of the image that corresponds to a land area that is erroneously detected as sea.

The extracted continuous coastline is shown in Fig.4.4(a). It must be pointed out that the coastal profile is well-fitted and no hole is present in the extracted coastline. To visually inspect the accuracy of the result, the extracted coastline is superimposed on the HV-polarized intensity image, see Fig.4.4(b). It can be noted that the 1-pixel extracted continuous coastline well fits the actual coastal profile, apart for a false edge within the land area. To quantitatively discuss the accuracy of the extracted coastline, an excerpt of the latter (see white box in Fig.4.4(b)) is superimposed on a reference coastline (that is manually traced using Fig.4.2(b)). The accuracy, measured in terms of overlapping between the two coastlines, is larger than 80% (see Table 4.2).

Table 4.2: Experimental results summary

Experiment	Land/Sea Ratio (dB)	Estimated σ	th	Figure of Merit (%)
Exp.1	6.05	0.0101	0.0934	81
Exp.2	7.44	0.0073	0.0674	83
Exp.3	7.83	0.0195	0.1797	-
Exp.4	22.55	0.0178	0.1635	92

The second experiment is relevant to the CSK HV-polarized SAR scene collected on September 16, 2010, at 17:53 UTC, in the Gulf of Naples (see Exp.2 in Table 4.1). An excerpt

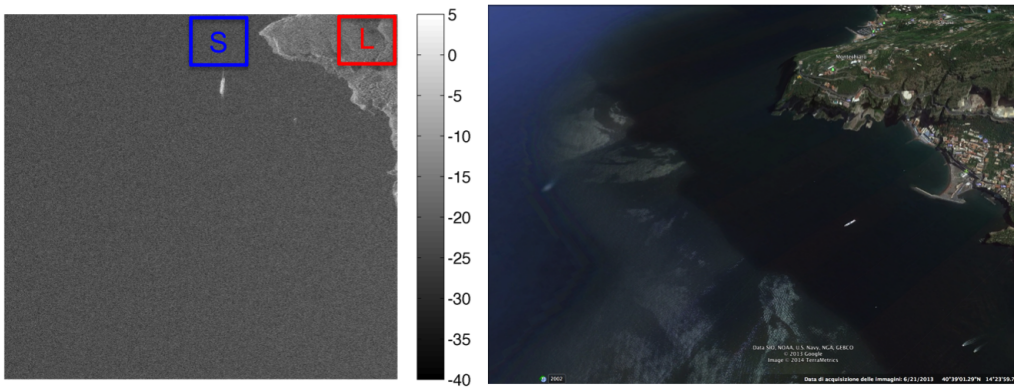

Figure 4.2: CSK SAR scene collected on September 6, 2010 in the Gulf of Naples. (a) Excerpt of the geocoded HV intensity image (dB scale is adopted), where the land and sea ROIs are labeled as "L" and "S", respectively; (b) Google Earth picture.

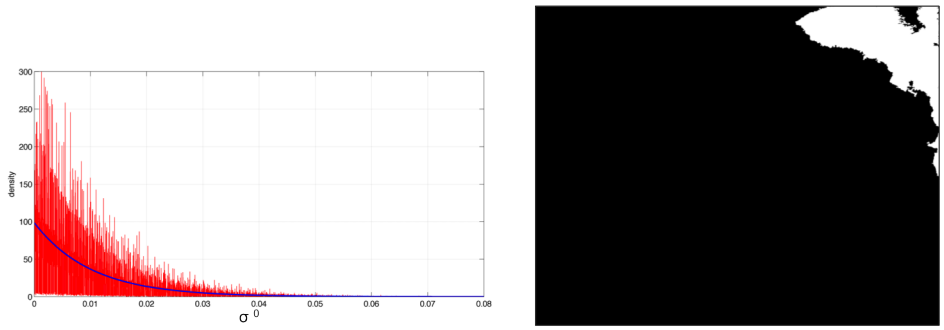

Figure 4.3: (a) Estimated empirical sea probability density function (pdf) versus the theoretical exponential one; (b) Binary output obtained with $th = 0.0934$.

(8557×15278 pixels) of the whole SAR scene is processed, see Fig.4.5(a). The considered area includes the Gulf of Pozzuoli and the islands of Ischia and Procida. This area is characterized by a various coastal morphology and by in-land water areas, as shown in Fig.4.5(b). The evaluated LSR and the σ parameter are equal to 7.44 dB and 0.0073, respectively (see Table 4.2). The estimated exponential-based global detection threshold is equal to $th = 0.0674$. The empirical sea distribution and the theoretical exponential one are shown in Fig.4.6(a), while the achieved binary output is shown in Fig.4.6(b). It can be noted that an area that is wrongly detected as land is visible in the upper-left corner of Fig.4.6(b).

In Fig.4.7(a) the extracted continuous coastline is shown, while it is superimposed on the HV-polarized intensity image in Fig.4.7(b). Also in this case the detected coastline well fits the

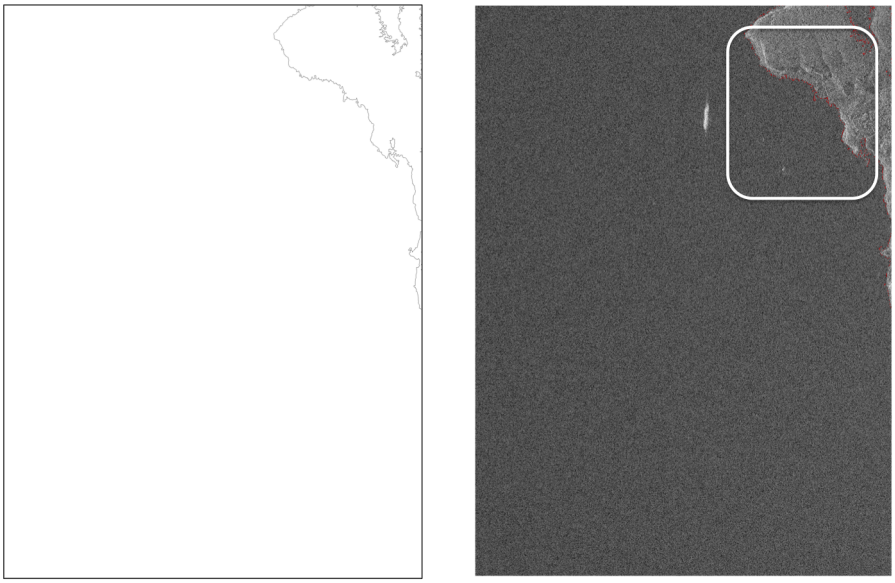

Figure 4.4: (a) Extracted 1-pixel continuous coastline; (b) Coastline superimposed on the HV intensity image.

actual coastal profile, apart for a false edge at sea on the upper-left corner of the image. Superimposing an excerpt (see white box in Fig.4.7(b)) of the extracted coastline to the corresponding manually traced reference, extracted from Fig.4.5(b), results in more than the 80% of detected edges overlapped, as listed in Table 4.2.

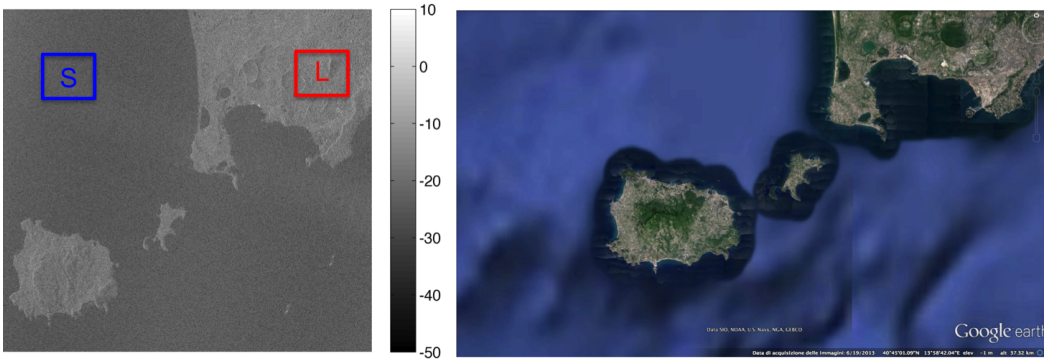

Figure 4.5: CSK SAR scene collected on September 16, 2010 in the Gulf of Naples. (a) Excerpt of the geocoded HV intensity image (dB scale is adopted), where the land and sea ROIs are labeled as "L" and "S", respectively; (b) Google Earth picture.

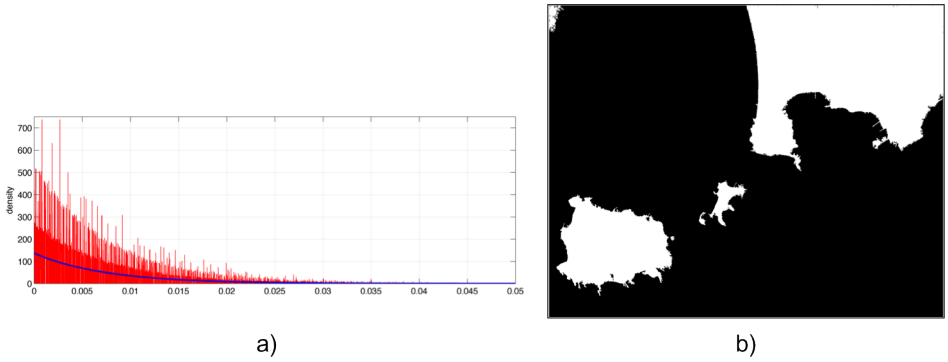

Figure 4.6: (a) Estimated empirical sea probability density function (pdf) versus the theoretical exponential one; (b) Binary output obtained with $th = 0.0674$.

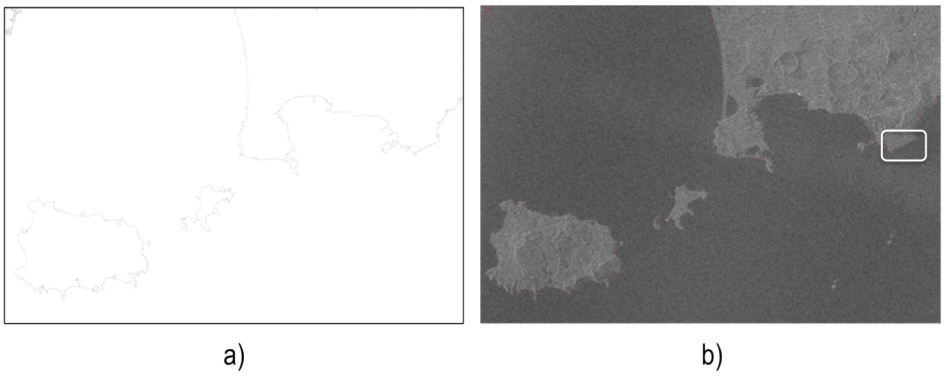

Figure 4.7: (a) Extracted 1-pixel continuous coastline; (b) Coastline superimposed on the HV intensity image.

The third experiment is relevant to the CSK HH-polarized SAR scene collected on December 13, 2013, at 15:57 UTC, in the Gulf of Cape Town (see Exp.3 in Table 4.1). An excerpt (809×6513 pixels) of the whole SAR scene is processed, as shown in Fig.4.8(a). The selected area includes the Robben island in front of the Cape Town harbor, and both the rocky and sandy littoral between the Cape Town harbor and the Koeberg nuclear power station (see Fig.4.8(b)). Unlike the previous experiments, as reported in Table 4.1, high wind speed conditions apply in this case.

LSR is equal to 7.83 dB, as listed in Table 4.2. This low value is due to rougher sea surface state. The empirical sea distribution and the theoretical exponential one are shown in Fig.4.9(a). The estimated σ value is equal to 0.0195 and the corresponding detection threshold is equal to th = 0.1797. These numbers are listed in Table 4.2. The binary output, achieved by using such a threshold, is shown in Fig.4.9(b).

It can be noted that, while the Robben island and the land area are well detected, false land areas at sea are present. This is actually due to the high sea state conditions that characterize the imaged area, that includes a pronounced wave pattern. Moreover, it can be easily noted that in the bottom left-hand side of Fig.4.10(a)-(b) the Robben island coastline is correctly detected due to calm sea conditions that apply in that area. It must be pointed out that similar results are obtained by varying P_{fa} (not shown to save space). It is important to underline that, as well as all the undertaken experiments, results are obtained in a single image analysis framework. A temporal stack of images would allow monitoring and detecting the temporal changes of the coastal profile. The availability of such an images stack is guaranteed by the CSK constellation dense revisit time.

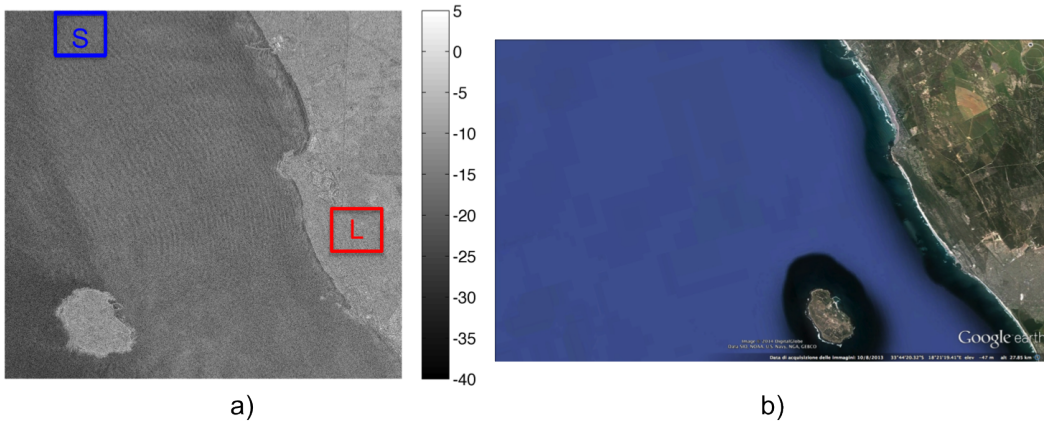

Figure 4.8: CSK SAR scene collected on December 13, 2013 in the Gulf of Naples. (a) Excerpt of the geocoded HH intensity image (dB scale is adopted), where the land and sea ROIs are labeled as "L" and "S", respectively; (b) Google Earth picture.

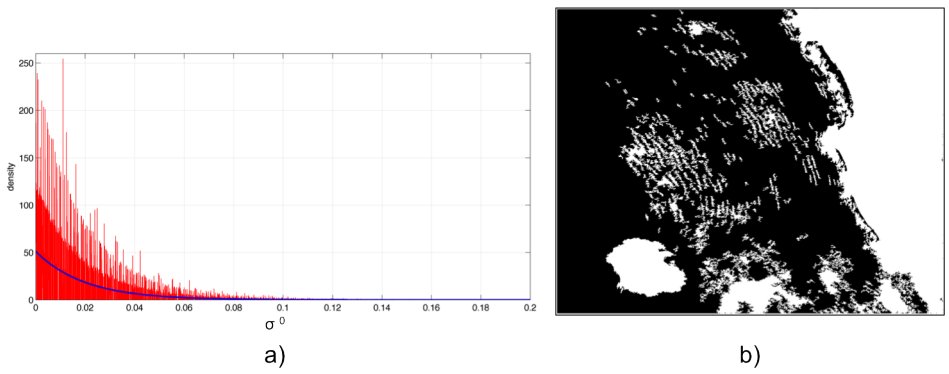

Figure 4.9: (a) Estimated empirical sea probability density function (pdf) versus the theoretical exponential one; (b) Binary output obtained with $th = 0.1797$.

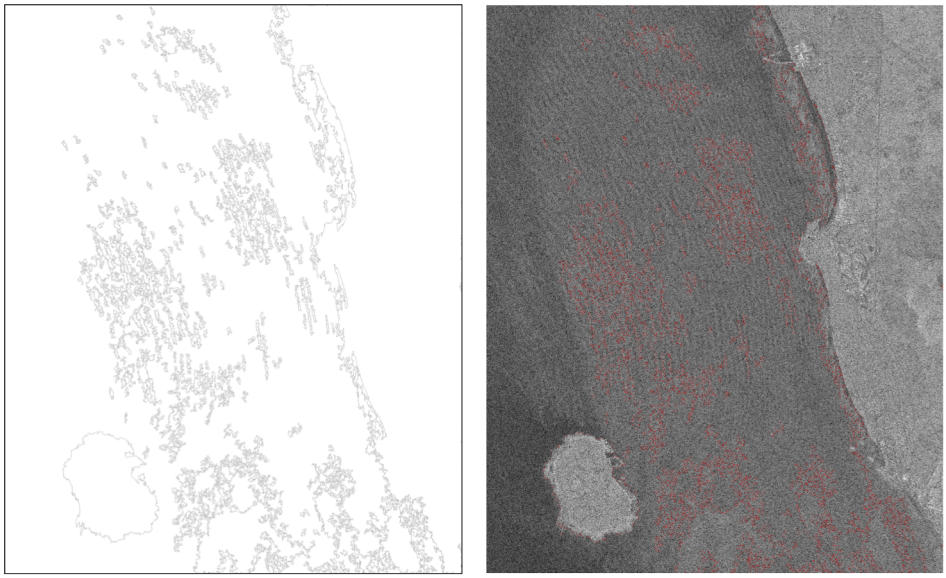

Figure 4.10: (a) Extracted 1-pixel continuous coastlin; (b) Coastline superimposed on the HH intensity image.

The fourth experiment is relevant to the CSK HH-polarized SAR scene collected on November 1, 2009, at 05:10 UTC, in the Gulf of Naples (see Exp.4 in Table 4.1). An excerpt (5908×4476 pixels) of the whole SAR scene is processed, see Fig.4.11(a). Such an area includes the mainly sandy littoral of Castellammare di Stabia, between the harbors of Torre Annunziata and Castellammare di Stabia (see Fig.4.11(b)).

The measured LSR is larger than the previous ones, and it is equal to 22.55 dB, as listed in Table 4.2. The empirical sea distribution and the theoretical exponential one are reported in Fig.4.12(a). The evaluated σ parameter is equal to 0.0178, and it turns into a detection threshold equal to $th = 0.1635$ (see Table 4.2). This threshold, when applied to the SAR image, produces the binary output shown in Fig.4.12(b). The extracted continuous coastline is shown in Fig.4.13(a). By superimposing this result on the HH-polarized intensity image, as shown in Fig.4.13(b), we can appreciate that the detected coastline is well fitted to the actual coastal profile, also for anthropic artifacts (e.g. wharfs and moles). Note that a false coastline, that corresponds to the imaged artifact (see the white circle in Fig.4.11(a)), is detected. This is due to SAR imaging mode, and in anyway it is attributable to the proposed approach. An excerpt (see white box in Fig.4.13(b)) of the extracted coastline is considered and superimposed on the corresponding manually traced reference coastline. As listed in Table 4.2, more than the 90%

of detected edges are overlapped. An enlarged version related to the ROI labeled as "R" in Fig.4.13(b) is shown in Fig 4.14(a). This area refers to the sandy littoral of Castellammare, Naples (see Fig.4.14(b)). Although the area results in a low LSR (6.74 dB), the proposed approach succeeds in extracting the coastline. However, some false edges due to SAR artifacts are also present.

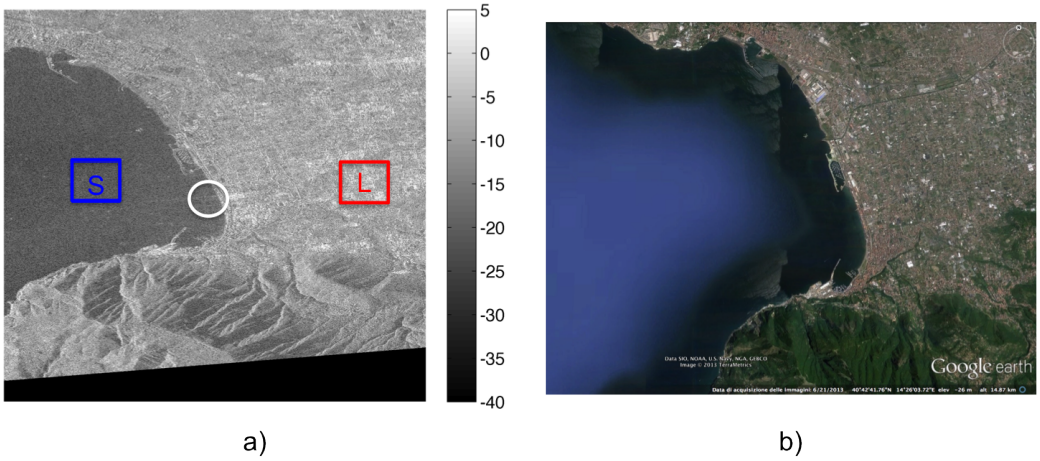

Figure 4.11: CSK SAR scene collected on November 11, 2009 in the Gulf of Naples. (a) Excerpt of the geocoded HH intensity image (dB scale is adopted), where the land and sea ROIs are labeled as "L" and "S", respectively; (b) Google Earth picture.

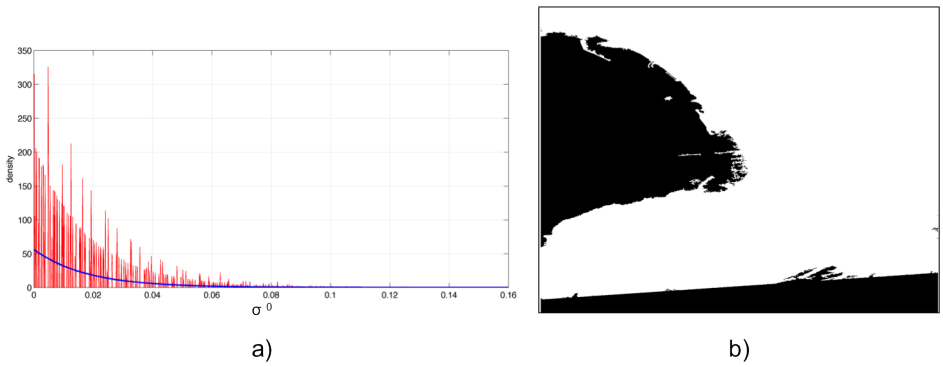

Figure 4.12: (a) Estimated empirical sea probability density function (pdf) versus the theoretical exponential one; (b) Binary output obtained with $th = 0.1635$.

In summary, CSK SAR data collected using the Himage Stripmap mode are exploited to discriminate land from sea in order to detect the continuos coastline. Land/sea discrimination is undertaken by generating a binary output from the SAR image, by employing a CFAR detector with a global threshold obtained exploiting an exponential distribution model for sea surface.

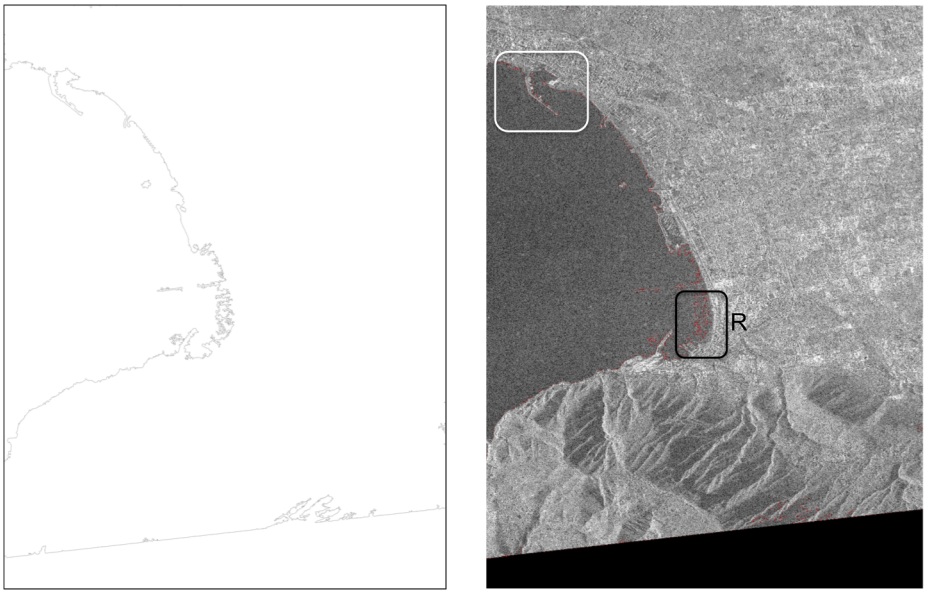

Figure 4.13: (a) Extracted 1-pixel continuous coastline; (b) Coastline superimposed on the HH intensity image.

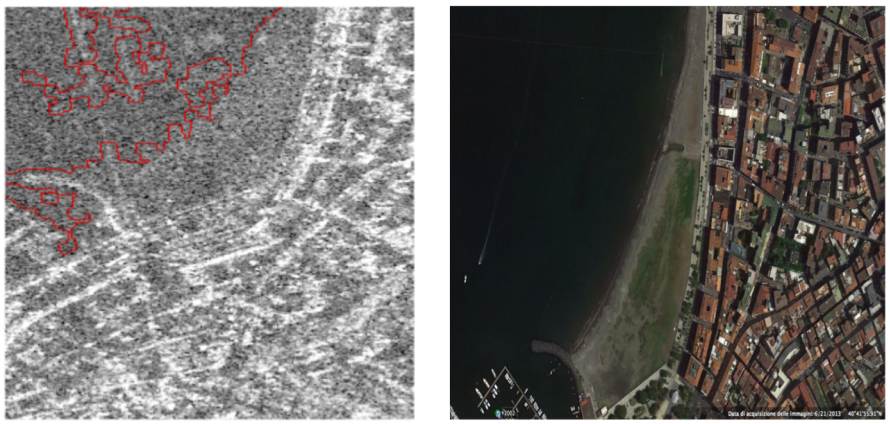

Figure 4.14: Enlarged version of the ROI labeled as "R" in Fig.4.13(b), corresponding to the Castellammare sandy coast. (a) Extracted coastline superimposed on the HH intensity image; (b) Google Earth picture.

Then, from such a binary output, the 1-pixel continuous coastline is extracted by means of a conventional Sobel edge detector. Experiments, undertaken on several images with a wide range of AOI and wind conditions, demonstrate that the proposed approach is accurate and effective,

for both HH and HV channels and for both low and high AOI, when low-to-moderate wind conditions apply. On the other hand, the occurring of high wind conditions and the presence of pronounced wave-like pattern give rise to poor results.

4.3 Sea/vegetation/urban discrimination by COSMO-SkyMed HH/VV PingPong mode SAR data

In this section, the capability of the CSK dual-polarization HH/VV PingPong mode SAR data to distinguish among sea, urban and vegetated areas is analyzed. A dual-polarization feature, namely the complex correlation between the copolar channels, is introduced to exploit the inherent peculiarities of the CSK incoherent dual-polarization PingPong mode for distinguishing the three scenarios. Such a feature is contrasted with the correlation between the HH and VV amplitudes, the copolar ratio and with conventional single-pol features, namely the HH and the VV intensity.
Therefore, the contribute of this study is the exploiting of both single- and dual-poalarization features derived from the incoherent CSK PingPong mode to discriminate among these three types of scenario.

4.3.1 COSMO-SkyMed incoherent dual-polarization PingPong mode

In this section, the CSK incoherent dual-polarization PingPong mode is briefly summarized.

CSK Stripmap PingPong mode, whose characteristics are listed in Table 4.3, is implemented by alternating a pair of transmitting/receiving polarizations across bursts by means of an antenna steering [48]. The two co-registered polarimetric channels, that can be selected among (HH, VV), (HH, HV) and (VV, VH), are acquired at slightly different times separated by the time interval τ. τ, which is given by the difference between the zero Doppler azimuth first time associated to the nth burst of the two polarimetric channels [73], is an increasing function of the incidence angle and its values range from 0.10 s to 0.25 s. Hence, since the phase link between the two channels is not preserved, the letters turn out to be incoherent.
The CSK instrument operating in dual-polarization PingPong mode acts like an along-track interferometer (ATI), that acquires two complex SAR images of the observed scene, in identical geometries and different polarizations, separated by the time lag τ. Mimicking the ATI configuration, in CSK PingPong mode the fore and the aft antennas are given by the combination of antenna steering and polarization switching. The swath size is about 30km×30km

(square frame), corresponding to an acquisition time of about 6.0 s, and a spatial resolution of 15m×15m.

Table 4.3: Characteristics of CSK SCS Level 1A PingPong mode SAR data

Polarization	(HH, VV); (HH, HV); (VV, VH);
Incidence angle (°)	20 ÷ 60
Swath (km)	30 x 30
Scene duration (s)	6
Azimuth resolution (m)	≤ 15
Ground Range resolution (m)	≤ 15

4.3.2 Dual-polarization observables

In this study the peculiarities of the dual-polarization CSK PingPong mode HH/VV data are exploited to discriminate among vegetated areas, urban areas and sea surface. The CSK PingPong data analysis is based on the evaluation of both single- and dual-polarization features. The latter include the correlation between the copolar channels, the correlation between the amplitudes of the HH and the VV channels and the copolar ratio.

The amplitude of the correlation between the copolar channels r is defined as

$$r(\tau) = |\langle S_{pp}(t) S^*_{qq}(t+\tau)\rangle|, \tag{4.5}$$

where S is the complex scattering amplitude and $\{p, q\} \in \{h, v\}$. Since in PingPong mode the CSK instrument acts like an ATI, it is important to read the copolar correlation amplitude in (4.5) in terms of both τ and the coherence time of the scene τ_c.

To provide a physical understanding of $r(\tau)$ in terms of the scene coherence time, a statistical description of the randomly rough sea surface is needed. In this study, the sea surface is assumed to follow the Pierson-Moskowitz spectrum. This is a reference scenario that applies under fully developed sea conditions. Hence, for low-to moderate resolutions and wind conditions, τ_c can be approximated as [74]

$$\tau_c = \frac{3\lambda}{u}, \tag{4.6}$$

where λ is the electromagnetic wavelength and u is the wind speed. For CSK X-band configuration τ_c is always lower than ≈ 0.035 s and hence $\tau_c \ll \tau$ [75]. Therefore, in this case, the copolar channels are practically uncorrelated, i.e. $r \approx 0$.

For land areas, which in this study are urban environment and vegetated areas, the backscattered signal is stronger and more persistent and a coherence time larger than the sea one is expected. Hence, the copolar channels are expected to be correlated, resulting in larger values of r. However τ_c can vary significantly in function of the land cover type thus leading to a variation of the correlation between the HH and VV channels.
In urban environments, specular, dihedral and trihedral scattering mechanisms take place, giving rise to a strong backscatter response over a wide range of incidence angles and frequencies. In such a case, the scatterers are considered as permanent scatterers [76] and, in modeling terms, the coherence time is expected to be significantly larger than τ:

$$\tau_c >> \tau, \tag{4.7}$$

implying a strong correlation between the HH and VV channels. Hence, in this case, r values should be significantly larger than the sea ones.
A different case is expected for vegetated areas. A critical fact is on one side the theoretical modeling of τ_c, not always straightforward, and on the other side its value in terms of τ. Theoretically speaking one expects a coherence time always longer than the one of a marine scene but much shorter than the one of urban areas. Accordingly, the correlation between the copolar channels should be larger with respect to the sea case and lower than the case of an urban scene.
On this rationale, the copolar correlation amplitude r is expected to assume the lowest values in the case of sea surface, the highest values for urban areas and intermediate values for vegetated areas.

In addition, since PingPong mode does not preserve the phase link between the two polarimetric channels, the correlation between the modulus of the copolar channels (r_m) is also considered:

$$r_m = \langle |S_{hh}| \cdot |S_{vv}| \rangle. \tag{4.8}$$

Regarding, the copolar ratio, that in this section is referred as r_{HV}, its definition is provided in the theoretical chapter.

4.3.3 Experiments

In this section, experiments undertaken on X-band level 1A SCS HH/VV CSK PingPong mode full resolution SAR data are presented. Four SAR scenes are processed, whose details are listed in Table 4.4, where wind information obtained by scatterometer data is also annotated. To get

information about the land cover and the type of vegetation, two sources of ground truth are used. The first is provided by a Coordination of Information on the Environment (CORINE) land cover map at 100×100 m^2 pixel size [77] that covers most of the European continent. The second consists of a vegetation cover map relevant to the Vesuvius National Park, situated in the Campania region, Italy, provided by the Dipartimento di Agraria of the Università di Napoli Federico II, Naples. For each SAR scene the single-polariazation features, i.e. the HH and the VV intensity (i_{HH} and i_{VV}, respectively), and the dual-poalrization features r (4.5), r_m(4.8) and r_{HV} are evaluated using a 7×7 average moving window. This allows also obtaining an equivalent spatial resolution comparable with the available ground truth. Then, each feature image is geocoded (UTM coordinates).

Table 4.4: CSK data set

Experiment	Geographic area	Acquisition Date and Time (UTC)	τ(s)	Incidence angle (°)	Wind speed (m/s)
Exp.1	Gulf of Naples	June 12, 2011 - 18:02	0.177	53.2-54.6	8
Exp.2	Gulf of Naples	June 27, 2011 - 17:44	0.131	31.4-35	2
Exp.3	South Holland	October 23, 2010 - 04:27	0.155	44.4-46.9	15
Exp.4	South Holland	October 17, 2010 - 04:33	0.144	39.6-41.7	4

The first experiment is relevant to the SAR scene collected over the Gulf of Naples on June 12, 2011, see Exp.1 in Table 4.4. An excerpt (5617×3983 pixels) of the whole SAR scene is considered and is represented in geographical coordinates in Fig.4.15(a). This includes urban environments (Naples and surrounding cities), vegetated areas and sea. The r, r_m, r_{HV}, i_{HH} and i_{VV} features are shown as false color images in Fig.4.15(b)-(f), respectively. Note that dB scale is used. A rough comparison with the Google Earth image of Fig.4.15(a) allows noting that, in all the cases but the r_{HV} image, sea surface can be distinguished from land and signals of well-distinguishable levels result from vegetated and urban environments. The r_{HV} image is very noisy and does not allow a straightforward land/sea discrimination. To provide a deeper analysis of the sensitivity of the above mentioned features with respect to sea, urban and vegetated areas, regions of interest (ROIs) are considered for each area. The size of the ROIs and the mean value of each feature are listed in Table 4.5.

With respect to the sea area, since the features shown in Fig.4.15 witness a non-negligible variability over the sea, two ROIs are selected, see "S1" and "S2" in Fig.4.15(a). Note that the ROIs are also annotated in Fig.4.15(b). The ROI "S1" belongs to a low backscattering area, see Fig.4.15(f). The mean value of the features, see Table 4.5, witnesses that all the features but i_{VV} result in similar values (within the same order of magnitude) for the two sea

ROIs. The mean value of i_{VV} evaluated within "S1" is one order of magnitude lower than the "S2" one. This witnesses that, as expected, i_{VV} shows the strongest variability with respect the sea conditions. With respect to the urban environment, to analyze the granularity of

Table 4.5: Mean values of the features evaluated within the ROIs shown in Fig.4.15(b).

ROI	size	r	r_m	r_{HV}	i_{HH}	i_{VV}
S1	81×78 pixels	$2.113{\cdot}10^{-5}$	$9.153{\cdot}10^{-5}$	0.691	$1.792{\cdot}10^{-4}$	$2.592{\cdot}10^{-4}$
S2	135×133 pixels	$8.443{\cdot}10^{-5}$	$4.558{\cdot}10^{-4}$	0.16	$3.5{\cdot}10^{-4}$	0.002
U1	138×407 pixels	0.083	0.451	2.667	1.018	0.382
U2	83×83 pixels	0.090	0.423	1.564	0.764	0.488
V1	104×55 pixels	0.001	0.009	1.053	0.013	0.012
V2	43×98 pixels	0.011	0.093	1.159	0.136	0.117
V3	45×27 pixels	0.004	0.029	0.964	0. 041	0.043

the features in discriminating urban areas characterized by a different buildings density, two ROIs are considered, see "U1" and "U2" in Fig.4.15(a)-(b). The ROI "U1" belongs to a high population density zone within the city of Naples. The ROI "U2" belongs to a suburban area of the city of Torre del Greco, Naples. It can be noted that r values related to the urban areas are well-distinguishable from the sea ones (about three order of magnitude). Moreover, r mean values do not allow separating urban from suburban areas, see Table 4.5. Similar comments apply for r_m that results in a better sea/urban separation (about four order of magnitude). i_{HH} provides the same sea/urban separation of r_m and shows also a certain granularity with respect to the urban (1.018) and the suburban (0.764) areas. A similar granularity applies for r_{HV}, see Table 4.5. However, r_{HV} exhibits the worst urban/sea separation.

With respect to the vegetated scenario, forested areas and cultivated fields are considered. Forested areas consist of two kind of forests that belong to the Vesuvius National Park. The Vesuvius National Park vegetation map shows that the first forest, located on the Vesuvius side, consists of Stone Pine woods while the second one, which consists of mixed Chestnuts woods sometimes colonized by hornbeam and maple, is located on the average-high slopes of Mount Somma. The cultivated field belongs to an agricultural area located near the city of Terzigno, in the province of Naples. In this case ground truth information provided by the CORINE land cover (CLC) map shows that the cultivated fields consist of fruit trees and beery plantations. Features values are listed in Table 4.5. With respect to "V1" and "V3" it can be noted that r exhibits intermediate values, i.e. values bounded by the sea and the urban area ones. In detail, r values are approximately one order of magnitude lower than the urban ones and two

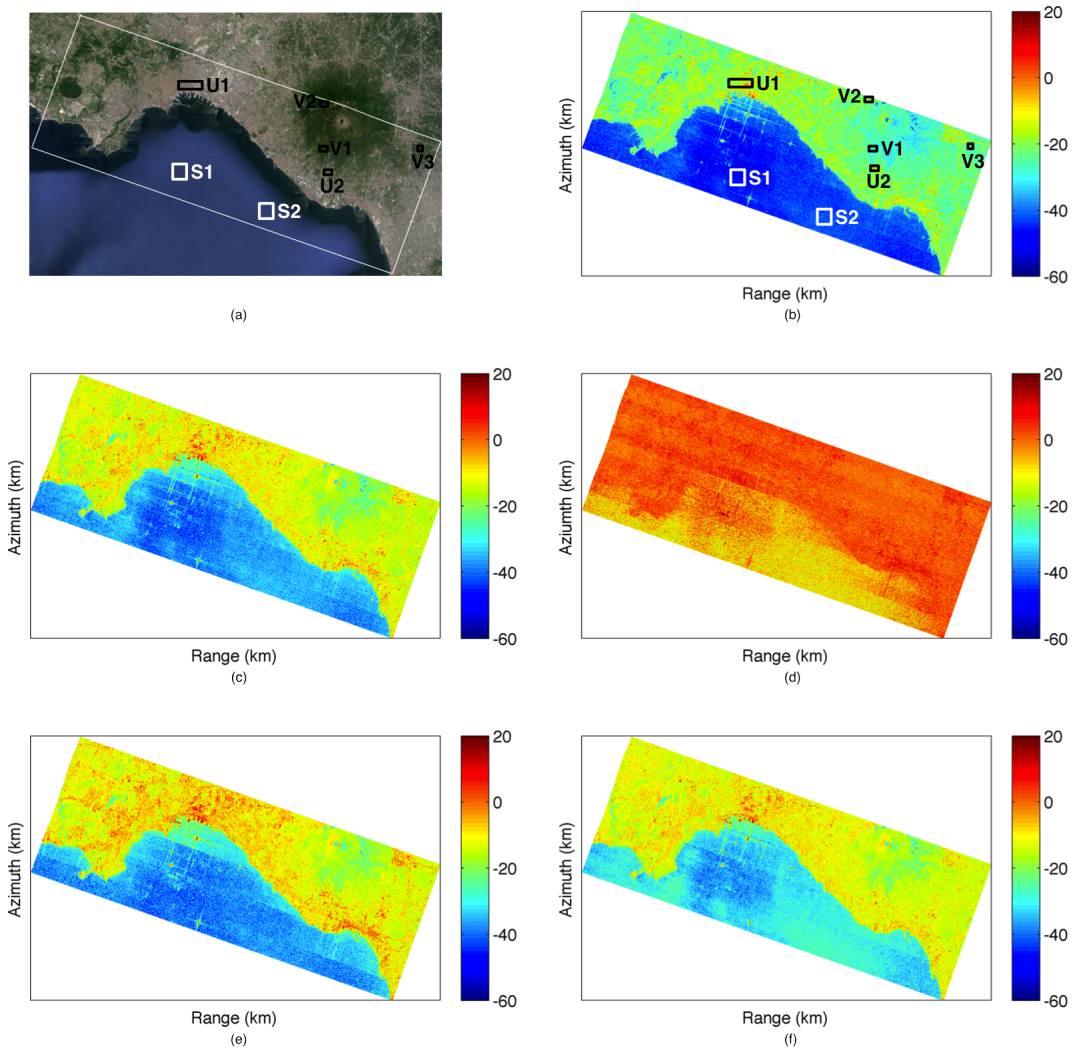

Figure 4.15: Excerpt of the CSK SAR data relevant to Exp.1, see Table 4.4. (a) Google Earth picture; (b) r image; (c) r_m image; (d) r_{HV} image; (e) i_{HH} image; (f) i_{VV} image. Note that all the features are shown in dB scale.

order of magnitude larger than the sea ones. Similar comments apply for all the features but r_{HV}, whose values, evaluated within "V1" and "V3" are of the same order of magnitude of the urban ones. A different behavior applies for the ROI "V2", that results in features values that are larger than "V1" and "V3" and are practically indistinguishable from the suburban area "U2" in all the features. The different behavior exhibited by Stone Pine woods (V1) and mixed Chestnuts woods (V2) is probably due to to the shape of the leaves. Chestnuts trees are

characterized by oval-shaped or lance-shaped leaves while Stone Pines have needle-like leaves that are completely different by the Chestnut ones. In electromagnetic terms this results in a a different backscattering response.

Following this sensitivity analysis, a simple k-means clustering algorithm [78] is applied to the features outputs. Note that r_{HV} is not considered since it shows very poor performance. In order to asses the accuracy of the clustering for each feature, the ground truth information provided by the CLC map is used as input for the computation of the confusion matrix. This allows obtaining, for each output of the k-means clustering, the OA, the PA and the UA. The number of classes in which each feature output is partitioned is equal to 3: "Sea", "Vegetation" and "Urban". For the computation of the confusion matrix a pre-processing of the CLC map is undertaken, which consists of the following steps:

- Selection of the area of interest, i.e. the area imaged by the CSK, from the whole CLC map.
- Projection of the CLC map into the geocoded SAR grid (UTM coordinates).
- The projected CLC map is reduced to three classes: sea, vegetation, and urban.

The CLC map obtained by the above steps, relevant to the Gulf of Naples, and the output of the k-means clustering for each feature are shown in Fig.4.16, where a legend indicating the color and the name of each class is also reported. It is important to note that the class "Bare Rocks" that belongs to the original CLC map, which includes the crater of Mount Vesuvius and some bare rock pattern present on the Mount Somma, is considered belonging to "Urban" class in the three classes CLC map since, in this case, we expect a strong backscattering response as in the case of urban areas. For each feature, an evaluation of the performance of the k-means clustering is provided by the OA, the PA and the UA listed in Table 4.6. With respect to

Table 4.6: OA, PA and UA of the k-means clustering output for each feature relevant to Exp.1.

		PA (%)			UA (%)		
Feature	OA (%)	Sea	Vegetation	Urban	Sea	Vegetation	Urban
r	77.97	95.27	73.71	57.68	98.31	64.19	66.01
r_m	78.74	96.10	75	57.78	98.71	65.12	66.94
i_{HH}	78.10	93.37	73.49	61.21	99.04	64.34	66.59
i_{VV}	75.68	95.19	67.46	56.74	97.69	61.68	61.09

OA, it can be noted that r_m performs best, r and i_{HH} provide very similar results, while i_{VV}

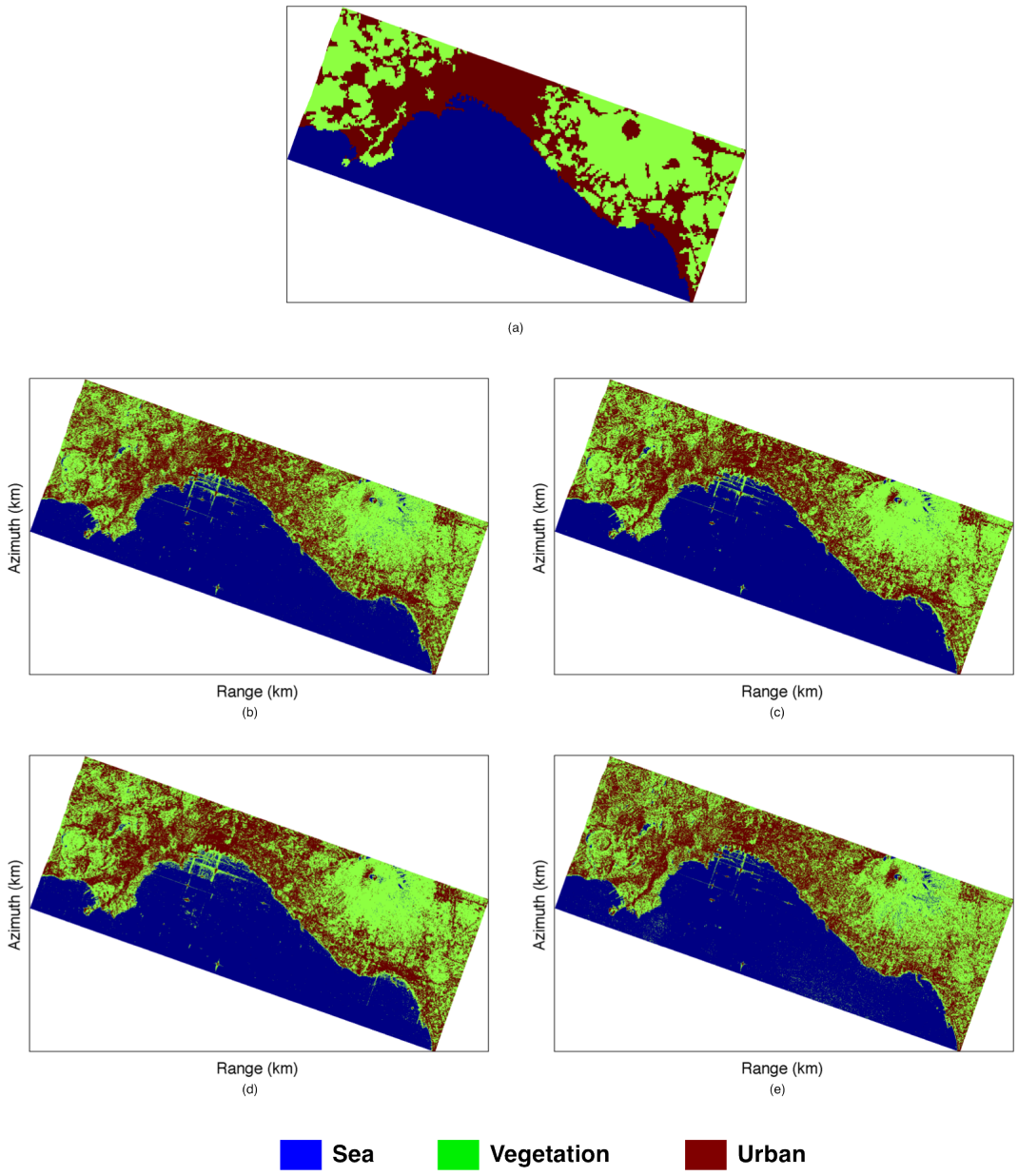

Figure 4.16: (a) CORINE land cover map over the Gulf of Naples (Exp.1) projected in the geocoded SAR grid and reduced to three classes; (b)-(e) k-means clustering output for r, r_m, i_{HH} and i_{VV}, respectively.

provides the poorest result. With respect to PA, r_m provides the best performance for "Sea" and "Vegetation" classes; while i_{HH} achieves the best performance for "Urban" class. The worst result is achieved by i_{HH} (for "Sea" class) and by i_{VV} (for "Vegetation" and "Urban"

classes). With respect to UA, r_m achieves best results for "Vegetation" and "Urban" classes; while i_{HH} performs best for "Sea" class. The worst performance is provided by i_{VV} for each of the three classes.

The second experiment is relevant to the SAR scene collected over the Gulf of Naples on June 27, 2011, see Exp.2 in Table 4.4. This scene is mostly overlapped with the previous one, but it is collected at a lower incidence angle. ($\sim 33°$). Hence, this experiment allows analyzing the sensitivity of the features to the incidence angle. An excerpt (5536×3945 pixels) of the whole SAR scene, shown in Fig.4.17(a) in geographical coordinates, is considered. In Fig.4.17(b)-(f) r, r_m, r_{HV}, i_{HH} and i_{VV} are shown as false color images, respectively. It can be noted that the r_{HV} image, Fig.4.17(d), although resulting in performance better than the one relevant to the previous experiment, does not allow a straightforward land/sea discrimination due to a lack of contrast. The mean value of r, r_m, r_{HV}, i_{HH} and i_{VV} is evaluated within ROIs corresponding to sea, urban and vegetated areas, see Fig.4.17(a)-(b). The size of the ROIs and the mean value of each feature are listed in Table 4.7.

With respect to the sea scenario, the images of Fig.4.17 witness that, even in this case, there is a non-negligible variability over the sea. Two ROIs, similar to the ones considered in the previous experiment are selected, see "S1" and the "S2" in Fig.4.17(a)-(b). The mean value of all the features is listed in Table 4.7. It can be noted the all the features result in values larger than the ones obtained in the previous experiment. This behavior can be explained considering that at $\sim 33°$ AOI Bragg scattering is the dominant mechanism, resulting in a larger copolar backscattering. The larger r and r_m are due to the shorter τ that applies at $\sim 33°$ AOI that results in a larger correlation.

With respect to the urban areas, two ROIs similar to the ones considered in the previous experiment are selected, see 'U1" and "U2" in Fig.4.17(a)-(b). The mean value of the features, listed in Table 4.7, shows that in this case r exhibits an urban/sea separation similar to the one obtained in the previous experiment (about three order of magnitude). Smaller urban/sea separation applies for all the remaining features. In detail, the urban/sea separation is about two and one order of magnitude for $r_m/i_{HH}/i_{VV}$ and r_{HV}, respectively. This result demonstrates that, although AOI affects all the features, r performs best in urban/sea discrimination.

With respect to the vegetated areas, the two ROIs "V1" and "V2" are similar to the ones considered in the previous experiment; while a different ROI is selected for the cultivated fields, see "V3" in Fig.4.17(a)-(b), since the one related to the previous experiment is out of this SAR scene. This ROI is located near the city of Terzigno and it is not shown to save

space. According to the CLC map, those fields still consist of fruit trees and barry plantations. Features mean values, listed in Table 4.7, witness that the features exhibit a behavior similar to the one experienced in the previous experiment.

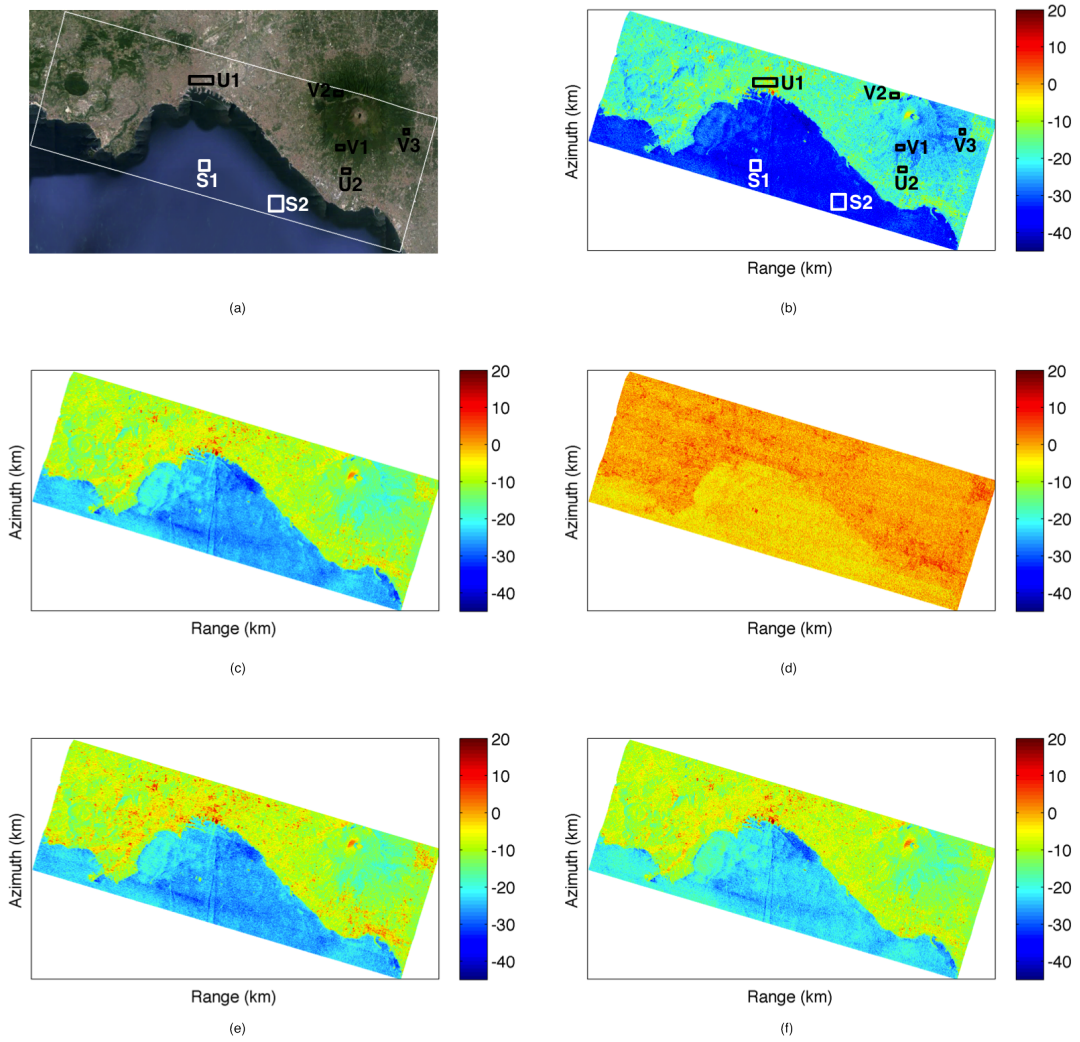

Figure 4.17: Excerpt of the CSK SAR data relevant to to Exp.2, see Table 4.4. (a) Google Earth picture; (b) r image; (c) r_m image; (d) r_{HV} image; (e) i_{HH} image; (f) i_{VV} image. Note that all the features are shown in dB scale.

The k-means clustering, applied to the features output using 3 classes (not shown), gives rise to the OA, PA and UA listed in Table 4.8, when compared with the CLC map. Note that, even in this case, r_{HV} is not considered due to its very poor performance. OA values witness that the total classification accuracy decreases with respect to the previous experiment for all the

Table 4.7: Mean values of the features evaluated within the ROIs shown in Fig.4.17(b).

ROI	size	r	r_m	r_{HV}	i_{HH}	i_{VV}
S1	69×117 pixels	$3.812{\cdot}10^{-4}$	0.002	0.651	0.003	0.004
S2	134×126 pixels	$4.811{\cdot}10^{-4}$	0.003	0.513	0.003	0.006
U1	140×449 pixels	0.101	0.522	1.604	0.873	0.544
U2	80×89pixels	0.073	0.360	1.579	0.617	0.390
V1	113×37 pixels	0.002	0.018	0.952	0.025	0.026
V2	51×80 pixels	0.031	0.217	0.940	0.277	0.295
V3	46×34 pixels	0.006	0.046	0.932	0. 06	0.065

features. It can be noted that r_m and i_{HH} result practically in the same OA, which is larger than the r and the i_{VV} one. With respect to PA, all the features exhibit values lower than the previous experiment in all the classes. The only exception is i_{HH}, whose PA is larger over the sea and is practically the same for "Vegetation" class. The best performance is provided by r_m, i_{HH} and i_{VV} for "Sea", "Vegetation" and "Urban" classes, respectively. The worst results are provided by i_{VV} for "Sea" and "Vegetation" classes and by i_{HH} for "Vegetation" class. With respect to UA, the best result is provided by i_{HH} and r_m for "Sea", "Urban" and "Vegetation" vegetation classes respectively. r provides the worst result for "Sea" class; while i_{VV} provides the worst result for "Vegetation" and "Urban" classes.

Table 4.8: OA, PA and UA of the k-means clustering output for each feature relevant to Exp.2.

		PA (%)			UA (%)		
Feature	OA (%)	Sea	Vegetation	Urban	Sea	Vegetation	Urban
r	73.62	93.55	68.26	54.74	93.01	60.68	64.45
r_m	75.50	95.80	71.18	54.97	95	62.83	65.68
i_{HH}	75.46	95.72	73.50	52.27	95.23	62.23	66.51
i_{VV}	72.02	91.35	64.41	56.50	93.39	58.74	61.62

The third experiment concerns the SAR scene collected over the South Holland on October 23, 2010, see Exp.3 in Table 4.4. An excerpt (11017×4105 pixels) of the whole SAR image is considered and it is shown in geographical coordinates in Fig.4.18(a). r, r_m, r_{HV}, i_{HH} and i_{VV} are shown as false color images in Fig.4.18(b)-(f), respectively. By visually inspecting Fig.4.18 it can be noted that all the features allow sea/land discrimination showing a non-negligible variability over land areas. An analysis of the sensitivity of all the features with respect to sea, urban and vegetated areas is provided by considering ROIs corresponding to such scenarios.

The size of the ROIs and the mean value of each feature are listed in Table 4.9.

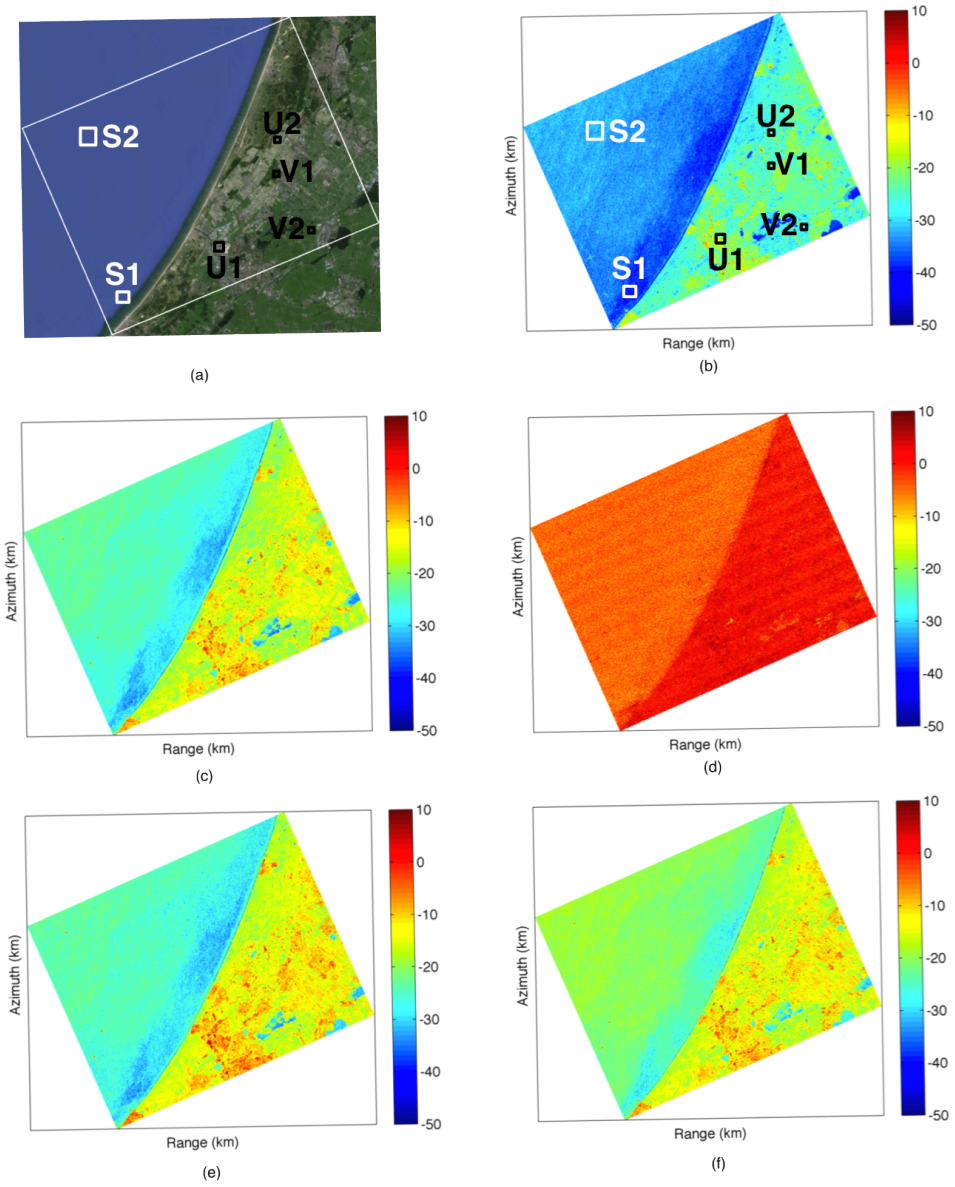

Figure 4.18: Excerpt of the CSK SAR data relevant to to Exp.3, see Table 4.4. (a) Google Earth picture; (b) r image; (c) r_m image; (d) r_{HV} image; (e) i_{HH} image; (f) i_{VV} image. Note that all the features are shown in dB scale.

With respect to the sea scenario, since the images shown in Fig.4.18 exhibit a variability over the sea surface, two ROIs, labeled as "S1" and "S2", which correspond to an area close to the coast and open sea, respectively, are considered (see Fig.4.18(a)-(b)). Note that this scene

Table 4.9: Mean values of the features evaluated within the ROIs shown in Fig.4.18(b).

ROI	size	r	r_m	r_{HV}	i_{HH}	i_{VV}
S1	99×60 pixels	$1.253{\cdot}10^{-4}$	$6.327{\cdot}10^{-4}$	0.334	$7.626{\cdot}10^{-4}$	0.002
S2	196×124 pixels	$8.707{\cdot}10^{-4}$	0.006	0.358	0.005	0.015
U1	146×203 pixels	0.068	0.374	2.038	0.693	0.340
U2	49×57 pixels	0.022	0.124	2.141	0.267	0.125
V1	59×37 pixels	0.004	0.038	0.938	0.051	0.055
V2	171×77 pixels	0.003	0.022	1.173	0. 034	0.029

calls for high wind conditions, see Table 4.4. All the features call for a behavior similar to the previous experiment. Moreover, all the features but r_{HV} show a different sensitivity with respect open sea (S2) and coastal water (S1), see Table 4.9.

With respect to the urban scenario, two areas characterized by different buildings density are considered, see "U1" and "U2" in Fig.4.18(a). The ROI "U1" belongs to the community of Rijnsburg, located near the town of Katwijk. The ROI "U2" belongs to De Zilk, a village that is part of the town of Noordwijkerhout (province of South Holland). It can be noted that the mean value of all the features within "U1" and "U2" are of the same order of magnitude showing a limited granularity, see Table 4.9. All the features allow clearly distinguishing urban areas from sea. The best performance is provided by r, r_m and i_{HH} (about two order of magnitude). The urban/sea separation reduces to about one order of magnitude for r_{HV} and i_{VV}.

With respect to the vegetated scenario, on the basis of the ground truth information provided by the CLC map, two different ROIs are considered. The first is a broad-leaved forest which belongs to the Keukenhof Park, which is located near the town of Lisse, see "V1" in Fig.4.18(a)-(b). The second vegetated area is an agricultural area located in Nieuwe Wetering (province of South Holland) and consists of pasture fields, see "V2" in Fig.4.18(a)-(b). Features values, listed in Table 4.9, show that in all the cases "V1" and "V2" call for similar values; hence limited granularity is present. Even in this case, as expected, intermediate features values apply that are lower-bounded by sea ones and upper-bounded by urban ones. However, it must be noted that the worst performance is obtained by r_{HV} whose values over urban and vegetated areas are very close, see Table 4.9. In addition, unlike the Gulf of Naples case, in this experiment all the features show a non-negligible granularity over urban areas allowing a clear distinction between urban and suburban areas.

The output of the k-means clustering algorithm, applied on the r, r_m, i_{HH} and i_{VV} image,

Table 4.10: OA, PA and UA of the k-means clustering output for each feature relevant to Exp.3.

		PA (%)			UA (%)		
Feature	OA (%)	Sea	Vegetation	Urban	Sea	Vegetation	Urban
r	59.96	60.16	53.17	80.87	96.12	41.26	36.25
r_m	53.05	53.74	40.46	89.98	97.85	32.44	32.01
i_{HH}	51.07	54.96	31.40	92.51	98.78	27.91	29.22
i_{VV}	50.72	45.48	51.57	78.35	92.23	33.76	35.23

is shown in Fig.4.19. Also in this experiment, 3 classes are used. In this case inland water bodies are present in the observed scene (see Fig.4.18(a)). Hence, to reduce the CLC map to three classes, such water bodies are considered belonging to "Sea" class. It must be pointed out that some water bodies that are visible in the SAR scene are not present in the original CLC map. This obviously affects the computation of the confusion matrix that results in reduced accuracy. Moreover, unlike the previous experiments, the coastal area is mostly characterized by sandy areas and it is practically undistinguishable from the sea in the CSK SAR scene. Hence, those areas are considered belonging to "Sea" class in the discretization of the CLC map. In addition, all the features results in misclassification over the sea due to high wind conditions. OA, PA and UA are listed in Table 4.10. It can be noted that r provides the highest OA while i_{VV} provides the lowest OA. Regarding PA, r performs best for "Sea" and "Vegetation" classes; while i_{HH} provides the best performance for "Urban" class. The poorest performances is provided by i_{VV} (classes "Sea" and "Urban") and i_{HH} (class "Vegetation"). With respect to UA, i_{HH} provides the best performance for "Sea" class; while r performs best for "Vegetation" and "Urban" classes. The poorest results are provided by i_{VV} (class "Sea") and i_{HH} (classes "Vegetation" and "Urban").

In order to analyze the behavior of the features over the area relevant to South Holland at a different AOI a fourth SAR scene is processed, see Exp.4 in Table 4.4. Such a scene is partially overlapped with the previous one, but moderate wind conditions apply. Unfortunately only part of the urban and the sea areas overlap with the previous scene. The single- and the dual polarization features, as well as the output of the k-means clustering algorithm, are not shown to save space. OA, PA and UA are listed in Table 4.11. It can be noted that, with respect to the previous experiment, OA significantly increases for all the features (i_{VV} exhibits the lowest increase). This is due to the moderate wind conditions that reduce the misclassifications, guaranteeing a significant separation between sea and vegetated areas for all the features. As

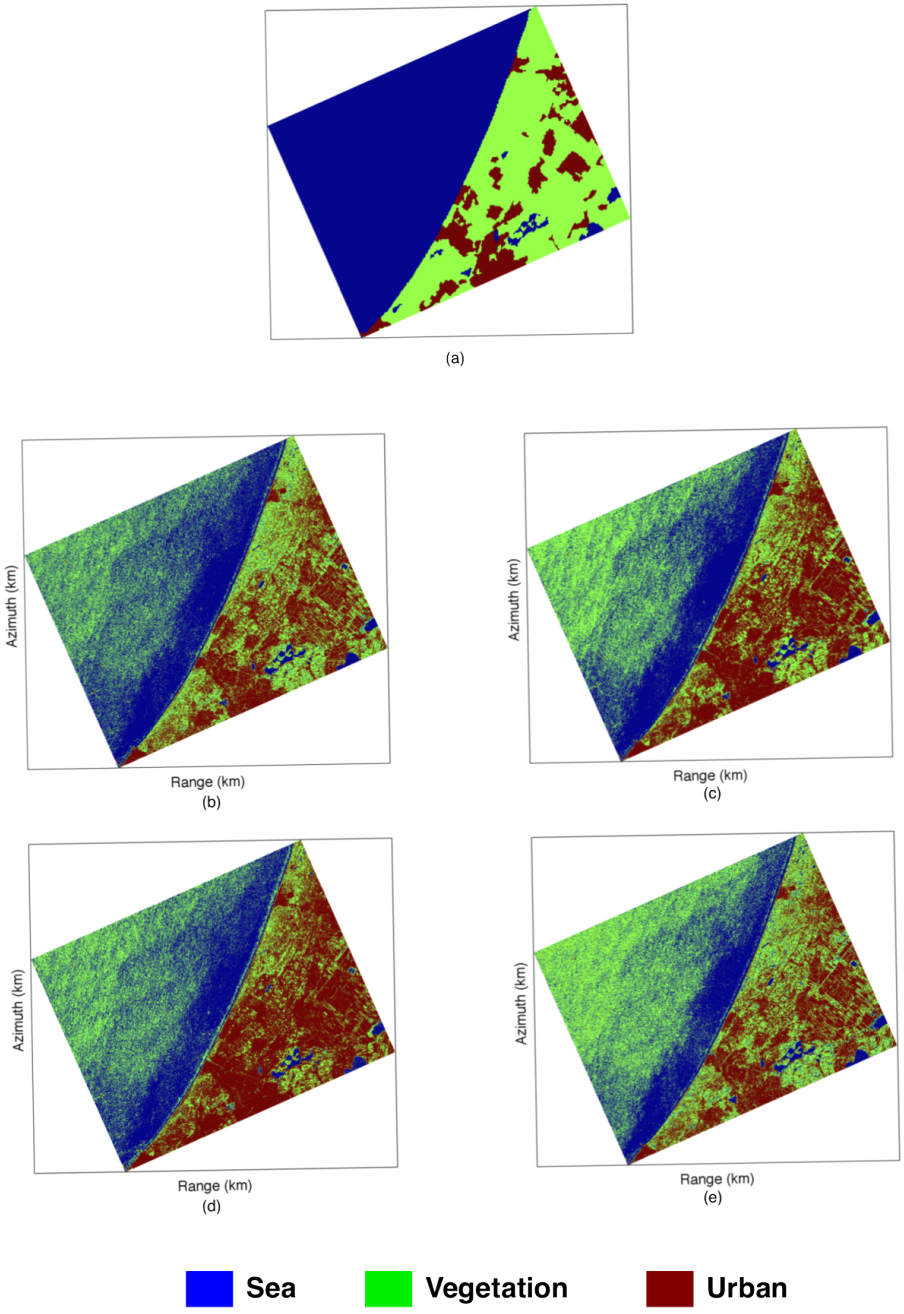

Figure 4.19: (a) CORINE land cover map over South Holland (Exp.3) projected in the geocoded SAR grid and reduced to three classes; (b)-(e) k-means clustering output for r, r_m, i_{HH} and i_{VV} respectively.

a consequence, with respect to the previous experiment, OA and PA values over for "Sea" and "Vegetation" classes are significantly larger for r, r_m and i_{HH} while, for i_{VV} such an increase is less significant. It can be noted (see Table 4.11), that i_{HH} provides the best OA. With respect to PA, i_{HH} performs best for "Sea" and "Vegetation" classes, while i_{VV} provides the best result for "Urban" class. Th worst results are provided by i_{VV} ("Sea" and "Vegetation" classes) and r_m ("Urban" class). Regarding UA, i_{HH} provides the best results for "Sea" and "Vegetation" classes, while r_m performs best for "Urban" class. Worst results are provided by r ("Sea" class) and i_{VV} ("Vegetation" and "Urban" classes).

Table 4.11: OA, PA and UA of the k-means clustering output for each feature relevant to Exp.4.

		PA (%)			UA (%)		
Feature	OA (%)	Sea	Vegetation	Urban	Sea	Vegetation	Urban
r	80.50	88.69	73.77	61.88	96.77	63.33	61.24
r_m	85.71	95.59	82.53	54.13	97.78	71.35	68.16
i_{HH}	86.35	96.03	82.65	56.51	98.61	72.68	66.91
i_{VV}	58.78	56.18	53.09	79.23	97.17	34.93	48.44

In summary, the sensitivity of CSK HH/VV PingPong mode SAR data with respect to sea, urban and vegetated areas is first investigated. The performances of single-polarization (HH and VV intensity) and dual-polarization features, i.e. the correlation between the copolar channels r, the correlation between the modulus of the copolar channels and the copolar ratio, in sea/vegetation/urban discrimination are assessed. Experiments undertaken on actual SAR data collected in different geographical areas and under different incidence angles demonstrate that:

- All the features call for a different sensitivity with respect the three scenarios.
- The worst result is provided by the copolar ratio.
- The HH intensity provides performance slightly better the VV one for land/sea discrimination.
- At higher incidence angles the correlation between the modulus of the copolar channels and the complex correlation provide the best OA in the k-means classification. The classification accuracy of all the features decreases at lower incidence angles.

- Sea state conditions play a key role to discriminate sea surface from vegetation. At high sea state conditions a large number of misclassifications is experienced over the sea surface.

Further studies will be devoted to the investigation of the capabilities of the CSK HH/HV and VV/VH channels to discriminate among the three scenarios.

4.4 Conclusions

In this chapter, the peculiarities of the CSK system, in particular its multi-polarization capabilities, have been exploited for land cover discrimination.

In the first study, HH and HV CSK Himage Stripmap mode SAR data, collected at different AOIs and different sea state conditions, have been used to separate land from sea in order to detect the coastline. Land/sea discrimination is carried out by means of CFAR detector with a global threshold that is based on an exponential distribution model for the sea surface backscattering. Results show that sea sate conditions significantly affect the separation of these two classes and, as a consequence, the coastline extraction. In facts, while the proposed approach turns out to be effective and accurate for a wide range of AOIs and in case of low-to-moderate wind conditions, it provides poor results when high when conditions apply.

In the second study, CSK incoherent dual-polarization PingPong mode HH/VV SAR data have been exploited for sea/vegetation/urban discrimination. Dual-polarization features, i.e. the correlation between the copolar channels, the correlation between the modulus of the copolar channels and the copolar ratio, along with the single-polarization ones, i.e. the HH and VV intensities, have been considered. Among all the features, the copolar ratio exhibits a significant lack of sensitivity with respect to the three scenarios thus being not able to distinguish them. In addition, it has been shown that, although the performance of the classification decrease at lower AOIs, the two kinds of correlation provide an overall accuracy slightly larger than the HH one. Also in this case, sea state condition affect the discrimination, especially between sea and vegetated areas.

5

Conclusions

In this thesis polarimetric SAR observables are effectively used to estimate phenological stages of agricultural crops. A dense time series of C- band full polarimetric RADARSAT–2 SAR data, built up by combining images collected at different incidence angles and with different orbit passes over the Barrax area (Spain) in 2009, during the AgriSAR field campaign, has been exploited.

Among the different crop types monitored in Barrax, this thesis has been focused on onion and oat fields. However, the estimation of phenological stages of other crops, such as wheat, barley and corn, is still subject of study.

In order to proper estimate phenology of onion and oat, a physical interpretation of the behavior of the polarimetric observables at different growth stages has been provided and then supervised classification procedures have been defined.

In the case of onion fields, whose growth stages estimation by means of polSAR data has been first addressed in this study, three phenological intervals have been estimated at the pixel level. Results shown that the use of the sole HV backscattering coefficient is not enough for an accurate estimation of these three intervals. In facts, the joint use of this parameter with polarimetric observables, i.e. the copolar coherence and the entropy, allows achieving the best estimation performance.

Regarding oat, contrarily to recent literature studies, carried out on a different test site, the polarimetric observables exhibit an appreciable sensitivity to phenological stages along all the cultivation cycle. This witnesses that the polarimetric response strongly depends on the test site and cultivation practices and that this type of analysis has to be applied locally. In this case, five phenological intervals have been properly estimated both at the pixel and at the

parcel level by means of an hierarchical tree which involves different parameters, namely: the standard deviation of the phase differences (both the linear and at the Pauli bases), the standard deviation of the dominant scattering angles, the HV/VV ratio and the Pauli_2 backscattering coefficient. The estimation accuracies are very high (between 87 and 100 %).
Further studies will be devoted to the estimation of crop phenology by means of the Wishart classifier, based on the statistics of the covariance matrix.

A second topic on which this thesis has been focused on is the land cover types discrimination by means of X- band multi-polarization COSMO-SkyMed (CSK) SAR data.
In a first step, single polarization Stripmap Himage mode CSK images, acquired both at the HH and HV polarizations, have been used to discriminate land areas form the sea ones, for coastline extraction purposes. Land/ sea separation has been performed with a CFAR detector with a globe threshold based on an exponential distribution for the sea surface backscattering intensity. Experiments, undertaken on SAR data acquired at different incidence angles, shown the effectiveness of the proposed approach for both the co- and the cross-polarized channel, when low-to-moderate wind conditions apply. On the other hand, high sea state conditions provide poor results.
In the second step, CSK incoherent dual-polarization PingPong mode SAR data have been used to discriminate sea, vegetated and urban scenarios. The analysis has been carried out by considering both single-polarization, i.e. the HH and the VV intensities, and dual-polarization features, i.e. the complex correlation between the copolar channels, the correlation between the modulus of the HH and the VV channels and the copolar ratio. Experiments shown that the copolar ratio provides the worst results in the discrimination. The performance of the k-means clustering applied to the features exhibits a decrease at lower incidence angles. Moreover, the two kinds of correlation performs slightly better with respect to the HH channel (which in turn is more accurate than VV) in terms of overall accuracy. As expected, sea state conditions significantly affect the discrimination.

References

[1] J. Lee and E. Pottier, *Polarimetric Radar Imaging: From Basics to Applications.* CRC Press, Boca Raton, 2009.

[2] F. Ulaby, K. Sarabandi, and A. Nashashibi, "Statistical properties of the Muller matrix of distributed targets," *IEE Proceedings*, vol. 139, no. 2, 1992.

[3] R. Azzam and N. Bashara, *Ellipsometry and Polarized Light.* Elsevier, Amsterdam, The Netherlands, 1977.

[4] A. Guissard, "Introduction to radar polarimetry," tech. rep., Université Catholique de Louvain, Faculté des Sciences Appliquées, Laboratoire de Télécommunications et Télédétection, 2005.

[5] S. Cloude and E. Pottier, "A review of target decomposition theorems in radar polarimetry," *IEEE Transaction on Geoscience and Remote Sensing*, vol. 34, no. 2, pp. 498–518, 1996.

[6] J. Lee, K. Hoppel, S. Mangond, and A. Miller, "Intensity and phase statistics of multilook polarimetric and interferometric SAR imagery," *IEEE Transaction on Geoscience and Remote Sensing*, vol. 32, no. 5, pp. 1017–1028, 1994.

[7] H. Skriver, M. Svendsen, and A. Thomsen, "Multitemporal C- and L-band polarimetric signatures of crops," *IEEE Transaction on Geoscience and Remote Sensing*, vol. 37, no. 5, pp. 2413–2429, 1999.

[8] F. Ulaby, D. Held, M. Dobson, C. McDonald, and T. Senior, "Relating polarization phase difference of SAR signals to scene properties," *IEEE Transaction on Geoscience and Remote Sensing*, vol. 25, no. 1, pp. 68–78, 1987.

[9] D. Hoekman and M. Quinones, "Biophysical forest type characterization in the Colombian Amazon by airborne polarimetric SAR," *IEEE Transaction on Geoscience and Remote Sensing*, vol. 40, no. 6, pp. 1288–1300, 2002.

[10] J. Lopez-Sanchez, S. Cloude, and J. Ballester, "Rice phenology monitoring by means of SAR Polarimetry at X-band," *IEEE Transaction on Geoscience an Remote Sensing*, vol. 50, no. 7, pp. 2695–2709, 2011.

[11] S. Cloude and E. Pottier, "An entropy based classification scheme for land applications of polarimetric SAR," *IEEE Transaction on Geoscience and Remote Sensing*, vol. 35, no. 1, pp. 498–518, 1997.

[12] U. Meier, *Growth Stages of Mono- and Dicotyledonous Plants.* Biologic Research Center for Agriculture and Forestry, 2th ed., 2001.

[13] J. Zadoks, T. Chang, and C. Konzak, "A decimal code for the growth stages of cereals," *Weed Research*, vol. 14, pp. 415–421, 1974.

[14] T. L. Toan, H. Laur, E. Mougin, and A. Lopes, "Multitemporal and dual-polarization observations of agricultural vegetation covers by X-band SAR images," *IEEE Transaction on Geoscience an Remote Sensing*, vol. 27, no. 6, pp. 709–718, 1989.

[15] T. Kurosu, M. Fujita, and K. Chiba, "Monitoring of rice crop growth from space using the ERS-1 C-band SAR," *IEEE Transaction on Geoscience an Remote Sensing*, vol. 33, no. 4, pp. 1092–1096, 1995.

[16] T. L. Toan, F. Ribbes, L. Wang, N. Floury, K. Ding, J. Kong, M. Fujita, and T. Kurosu, "Rice crop mapping and monitoring using ERS-1 data based on experiment and modeling results," *IEEE Transaction on Geoscience an Remote Sensing*, vol. 35, no. 1, pp. 41–56, 1997.

[17] A. Bouvet, T. L. Toan, and N. Lam-Dao, "Monitoring of the rice cropping system in the Mekong Delta using Envisat/ASAR dual polarization data," *IEEE Transaction on Geoscience an Remote Sensing*, vol. 47, no. 2, pp. 517–526, 2009.

[18] C. Picard, T. L. Toan, and F. Mattia, "Understanding C-band radar backscatter from wheat canopy using a multiple-scattering coherent model," *IEEE Transaction on Geoscience an Remote Sensing*, vol. 41, no. 41, pp. 1583–1591, 2003.

[19] K. Stankiewicz, "The efficiency of crop recognition on ENVISAT ASAR images in two growing seasons," *IEEE Transaction on Geoscience an Remote Sensing*, vol. 44, no. 4, pp. 806–814, 2006.

[20] P. Saich and M. Borgeaud, "Interpreting ERS SAR signatures of agricultural crops in Flevoland, 1993-1996," *IEEE Transaction on Geoscience an Remote Sensing*, vol. 38, no. 2, pp. 651–657, 2000.

[21] F. Mattia, T. L. Toan, G. Picard, F. Posa, A. D'Alessio, C. Notarnicolaand, A. Gatti, M. Rinaldi, G. Satalino, and G. Pasquariello, "Multitemporal C-band radar measurements on wheat fields," *IEEE Transaction on Geoscience an Remote Sensing*, vol. 41, no. 7, pp. 1551–1560, 2003.

[22] G. Satalino, F. Mattia, T. L. Toan, and M. Rinaldi, "Wheat crop mapping by using ASAR AP data," *IEEE Transaction on Geoscience an Remote Sensing*, vol. 47, no. 2, pp. 527–1530, 2009.

[23] J. Lopez-Sanchez, J. Ballester, and I. Hajnsek, "First results of rice monitoring practices in Spain by means of time series of TerraSAR-X dual-pol images," *IEEE Journal of Selected Topics in Applied earth Observations and Remote Sensing*, vol. 4, no. 2, pp. 412–422, 2011.

[24] J. Lopez-Sanchez, J. Ballester, F. Vicente-Guijalba, and S. Cloude, "Estimating phenology of agricultural crops from space," *Proceedings of ESA Living Planet Symposium, September 9-13, Edimburg, UK*, 2013.

[25] J. Lopez-Sanchez, F. Vicente-Guijalba, J. Ballester, and S. Cloude, "Polarimetric response of rice fields at C-band: Analysis and phenology retrieval," *IEEE Transaction on Geoscience an Remote Sensing*, vol. 50, no. 5, pp. 2977–2993, 2014.

[26] J. Liu, W. Paris, and H. McNairn, "Multiyear crop monitoring using Polarimetric RADARSAT-2 Data," *IEEE Transaction on Geoscience and Remote Sensing*, vol. 51, no. 4, pp. 2227–2240, 2013.

[27] X. Jiao, J. Kovacs, J. Shang, H. McNairn, D. Walters, B. Ma, and X. Geng, "Object-oriented crop mapping and monitoring using multi-temporal polarimetric RADARSAT-2 data," *ISPRS Journal of Photogrammetry and Remote Sensing*, vol. 96, pp. 38–46, 2014.

[28] L. Mascolo, J. Lopez-Sanchez, F. Vicente-Guijalba, G. Mazzarella, F. Nunziata, , and M. Migliaccio, "On the sensitivity of Polarimetric SAR observables to phenological stages of crops in Barrax, Spain: First results at C-band," *Proceedings of the IEEE GOLD Conference 2014, June 5-6, Belrin, Germany*, 2014.

[29] F. Vicente-Guijalba, T. Martinez-Marin, and J. Lopez-Sanchez, "Crop phenology estimation using a multitemporal model and a Kalman filtering strategy," *IEEE Geoscience and Remote Sensing Letters*, vol. 11, no. 6, pp. 1081–1085, 2014.

[30] F. Vicente-Guijalba, T. Martinez-Marin, and J. Lopez-Sanchez, "Dynamical approach for real-time monitoring of agricultural crops," *IEEE Transaction on Geoscience and Remote Sensing*, 2014. DOI: 10.1109/TGRS.2014.2372897.

[31] C. D. Bernardis, F. Vicente-Guijalba, T. Martinez-Marin, and J. Lopez-Sanchez, "Estimation of key dates and stages in rice crops using dual-polarization SAR time series and a particle filtering approach," *IEEE Journal of Selected Topics in Applied earth Observations and Remote Sensing*, 2014. DOI: 10.1109/JSTARS.2014.2372898.

[32] J. Cable, J. Kovacs, X. Jiao, and J. Shang, "Agricultural monitoring in Northeastern Ontario, Canada, using multi-temporal polarimetric RADARSAT-2 Data," *Remote Sensing*, vol. 6, no. 3, pp. 2343–2371, 2014.

[33] L. Mascolo, J. Lopez-Sanchez, F. Vicente-Guijalba, G. Mazzarella, F. Nunziata, , and M. Migliaccio, "Retrieval of phenological stages of onion fields during the first year of growth by means of C-band polarimetric SAR measurements," *submitted to Internationl Journal of Remote Sensing.*

[34] L. Mascolo, J. Lopez-Sanchez, F. Vicente-Guijalba, F. Nunziata, , M. Migliaccio, and G. Mazzarella, "On the retrieval of phenological stages of agricultural crops by means of C-band polarimetric SAR Data in Barrax,Spain," *Proceedings of PolinSAR 2015, January 26-30, ESA-ESRIN, Frascati, Italy*, 2015.

[35] M. Gonzáles-Sanpedro, T. L. Toan, and J. Moreno, "Multitemporal analysis of MERIS-FR Data for crop monitoring in two agricultural areas: Barrax and Tolouse," *Proceedings of the 2004 Envisat and ERS Symposium, September 6-10, Salzburg, Austria*, 2004.

[36] M. Gonzles-Sanpedro, T. L. Toan, J. Moreno, L. Kergoat, and E. Rubio, "Seasonal variations of leaf area index of agricultural fields retrieved from landsat data," *Remote Sensing of the Enviroment*, vol. 112, pp. 810–824, 2008.

[37] C. Atzbeger and K. Richter, "Spatially constrained inversion of radiative transfer models for improved LAI mapping from future Sentinel-2 Imagery," *Remote Sensing of Environment*, vol. 120, pp. 208–218, 2012.

[38] M. Moran, L. Alonso, J. Moreno, M. Mateo, D. de la Cruz, and A. Montoro, "A RADARSAT-2 quad-polarized time series for monitoring crop and soil conditions in Barrax, Spain," *IEEE Transaction on Geoscience and Remote Sensing*, vol. 50, no. 4, pp. 1057–1070, 2012.

[39] J. Sobrino, A. Franch, R. Oltra-Carrió, E. Vermote, and E. Fedele, "Evaluation of MODIS Albedo product over a heterogeneous agricultural area," *International Journal of Remote Sensing*, vol. 34, no. 15, pp. 5530–5540, 2013.

[40] P. Latorre-Carmona, Y. Knyazikhin, L. Alonso, J. Moreno, F. Pla, and Y. Yan, "On hyperspectral remote sensing of leaf biophysical constituents: Decoupling vegetation structure and leaf optics using CHRISPROBA data over crops in Barrax," *IEEE Geoscience and Remote Sensing Letters*, vol. 11, no. 9, pp. 1579–1583, 2014.

[41] L. Opara, "ONION: Post-harvest operations," *FAO*, 2003.

[42] L. Opara, "FLOWERING LOCUS T genes control onion bulb formation and flowering," *Nature Communications*, 2013. DOI: 10.1038/ncomms3884.

[43] J. Brewster, *Onions and other vegetable Alliums.* CABI, 2th ed., 2008.

[44] F. Ulaby, R. Moore, and A. Fung, *Microwave Remote Sensing: Active and Passive*, vol. 3. Artech House, Norwood, MA, 1986.

[45] J. Suttie and S. Reynolds, *FODDER OATS: a world overview.* 33, FAO, 2004.

[46] A. Larranaga, J. Alvarez-Mozos, L. Albizua, and J. Peters, "Backscattering behavior of rain-fed crops along the growing season," *IEEE Geoscience and Remote Sensing Letters*, vol. 10, no. 2, pp. 386–390, 2013.

[47] A. Freeman and S. Durden, "A three-component scattering model for polarimetric SAR data," *IEEE Transaction on Geoscience and Remote Sensing*, vol. 36, no. 3, pp. 963–973, 1998.

[48] "COSMO-SkyMed SAR system description and user guide," Online: http://www.asi.it/it/flash/osservare/cosmoskymed.

[49] F. Nunziata, M. Migliaccio, K. Li, and X. Ding, "Coastline extraction using dual-polarimetric COSMO-SkyMed PingPong mode SAR data," *IEEE Geoscience and Remote Sensing Letters*, vol. 11, no. 1, pp. 104–108, 2014.

[50] M. Pelnaver, C. Pratola, I. Fabrini, F. D. Frate, G. Schiavon, and D. Solomini, "Classification of PingPong COSMO-SkyMed imagery using supervised and unsupervised neural network algorithms," *Proceedings of IEEE International Geoscience and remote Sensing Symposium*, pp. 5888–5891, 2012.

[51] G. Satalino, D. Impedovo, A. Balenzano, and F. Mattia, "Land cover classification by using multi temporal COSMO-SkyMed data," *Proceedings of IEEE Multi-temporal Remote Sensing images International Workshop*, pp. 17–20, 2011.

[52] V. Vijaya and G. Niveditha, "Classification of COSMO-SkyMed SAR data based on coherence and backscattering coefficient," *International Journal of Computer Science and Informatics*, vol. 1, no. 4, pp. 60–63, 2012.

[53] L. Mascolo, M. Sarti, F. Nunziata, , and M. Migliaccio, "Vesuvius national park monitoring by COSMO-SkyMed PingPong data analysis," *Proceedings of PolinSAR 2013, January 28-February 1, ESA-ESRIN, Frascati*, 2013.

[54] A. Buono, F. Nunziata, L. Mascolo, and M. Migliaccio, "A multipolarization analysis of coastline extraction using X-band COSMO-SkyMed SAR data," *IEEE Journal of Selected Topics in Applied earth Observations and Remote Sensing*, vol. 7, no. 7, pp. 2811–2820, 2014.

[55] L. Mascolo, F. Nunziata, A. Fanti, G. Mazzarella, and M. Migliaccio, "On the incoherent COSMO-SkyMed PingPong mode to distinguish among sea, vegetated and urban scenarios," *Proceedings of the IEEE GOLD Conference 2014, June 5-6, Belrin, Germany*, 2014.

[56] M. Migliaccio, L. Mascolo, F. Nunziata, M. Sarti, and G. Mazzarella, "COSMO-SkyMed HH/VV PingPong mode SAR data to discriminate among sea, urban, and vegetated areas," *IEEE Journal of Selected Topics in Applied earth Observations and Remote Sensing*, vol. 7, no. 7, pp. 2880–2894, 2014.

[57] "Population action international©," Online: http://www.earth.columbia.edu/news/2006/story07-11-06.php.html.

[58] "Marine management organisation©," Online: http://www.marinemanagement.org.uk/marineplanning/.

[59] S. Dellepiane, R. D. Laurentiis, and F. Giordano, "Coastline extraction from SAR images and a method for the evaluation of the coastline precision," *Pattern Recognition Letters*, vol. 25, pp. 1461–1470, 2004.

[60] X. Descombes, M. Moctezuma, H. Maitre, and J. Rudant, "Coastline detection by a markovian segmentation on SAR images," *Signal Processing*, vol. 55, pp. 123–132, 1995.

[61] Y. Ouyang, J. Chong, and Y. Wu, "Two coastline detection methods in Synthetic Aperture Radar imagery based on level set algorithm," *International Journal of Remote Sensing*, vol. 31, no. 17, pp. 4957–4968, 2010.

[62] F. Nunziata, P. Sobieski, and M. Migliaccio, "The two-scale BPM scattering model for sea biogenic slicks contrast," *IEEE Transaction on Geoscience and Remote Sensing*, vol. 47, no. 7, pp. 1949–1955, 2009.

[63] M. Migliaccio, G. Ferrara, A. Gambardella, F. Nunziata, and A. Sorrentino, "A physically consistent speckle model for marine SLC SAR images," *IEEE Journal of Ocean Engineering*, vol. 32, no. 4, pp. 839–847, 2007.

[64] F. Ulaby, D. Long, and et. al, *Microwave Radar and Radiometric Remote Sensing.* University of Michigan Press, 2013.

[65] A. Fung, W. Liu, K. Chen, and M. Tsay, "An improved model for bistatic scattering from rough surfaces," *Journal of Electromagnetic Wave*, vol. 16, no. 5, pp. 689–702, 2002.

[66] H. Lee, J. Barter, K. Beach, C. Hindman, B. Lake, H. Rungaldier, J. Shelton, A. W. R. Yee, and H. Yuen, "X band microwave backscattering from ocean waves," *Journal of Electromagnetic Wave*, vol. 100, no. C2, pp. 2591–2611, 1995.

[67] D. Velotto, M. Migliaccio, F. Nunziata, and S. Lehner, "Dual-polarized TerraSAR-X data for oil-spill observation," *IEEE Transaction on Geoscience and Remote Sensing*, vol. 49, no. 12, pp. 4751–4762, 2011.

[68] J. Chen, Y. Chen, and J. Yang, "Ship detection using polarization cross-entropy," *IEEE Geoscience and Remote Sensing Letters*, vol. 6, no. 4, pp. 723–727, 2009.

[69] R. Touzi and F. Charbonneau, "Characterization of symmetric scattering using polarimetric SAR," *IEEE Proceedings of IGARSS, Toronto, Canada*, 2002.

[70] H. Liu and K. Jezek, "Automated extraction of coastline from satellite imagery by integrating Canny edge detection and locally adaptive thresholding methods," *International Journal of Remote Sensing*, vol. 25, no. 5, pp. 937–958, 2004.

[71] R. Maini and H. Aggarwal, "Study and comparison of various image edge detection techniques," *International Journal of Image Processing*, vol. 3, no. 1, pp. 1–12, 2009.

[72] "Weather underground©," Online: http://www.wunderground.com/history.

[73] "COSMO-SkyMed SAR products handbook," Online: http://www.asi.it/it/flash/osservare/cosmoskymed.

[74] J. Frasier and J. Camps, "Dual-beam interferometry for ocean surface current vector mapping," *IEEE Transaction on Geoscience and Remote Sensing*, vol. 39, no. 2, pp. 401–414, 2001.

[75] F. Nunziata and M. Migliaccio, "On the COSMO-SkyMed PingPong mode to observe metallic targets at sea," *IEEE Journal of Ocean Engineering*, vol. 38, no. 1, pp. 71–79, 2013.

[76] J. Inglada, J. Souyris, and C. Tison, "Incoherent SAR polarimetric analysis over point targets," *IEEE Transaction on Geoscience and Remote Sensing*, vol. 3, no. 2, pp. 246–249, 2006.

[77] "Corine land cover 2006 raster data," Online: http://www.eea.europa.eu/data-and-maps/data/corine-land-cover-2006-raster.,.

[78] G. Seber, *Multivariate Observations*. John Wiley and Sons Incorporated, Hoboken,U.S., 1984.

List of publications

Papers published on International Journals

1. M. Migliaccio, L. Mascolo, F. Nunziata, M. Sarti, and G. Mazzarella, "COSMO-SkyMed HH/VV PingPong Mode SAR Data to Discriminate Among Sea, Urban, and Vegetated Areas," *IEEE Journal of Selected Topics in Applied Earth Observation and Remote Sensing*, vol. 7, no. 7, pp. 2880-2894, 2014.
2. A. Buono, F. Nunziata, L. Mascolo, and M. Migliaccio, "A Multipolarization Analysis of Coastline Extraction Using X-Band COSMO-SkyMed SAR Data," *IEEE Journal of Selected Topics in Applied Earth Observation and Remote Sensing*, vol. 7, no. 7, pp. 2811-2820, 2014.

Submitted papers

1. L. Mascolo, J.M. Lopez-Sanchez, F. Vicente-Guijalba, G. Mazzarella, F. Nunziata, M. Migliaccio, "Retrieval of Phenological Stages of Onion Fields During the First Year of Growth by means of C-band Polarimetric SAR Measurements," *International Journal of Remote Sensing*.

Conference papers

1. L. Mascolo, J. M. Lopez-Sanchez, F. Vicente-Guijalba, F. Nunziata, M. Migliaccio, G. Mazzarella, "On the Retrieval of Phenological Stages of Agricultural Crops by means of C-band Polarimetric SAR Data in Barrax, Spain," *Proceedings of PolinSAR 2015 Workshop*, ESA-ESRIN, Frascati, Italy, January 26-30, 2015.
2. L. Mascolo, J. M. Lopez-Sanchez, G. DUrso, F. Nunziata, M. Migliaccio, G. Mazzarella, "Multipolarization and multifrequency SAR Data to observe Agricultural Crops," *Proceedings of PolinSAR 2015 Workshop*, ESA-ESRIN, Frascati, Italy, January 26-30, 2015.

3. M. Sarti, L. Mascolo, M. Migliaccio, F. Nunziata, E. Brugnoli, C. Calfapietra, "On potential Estimation of Permafrost-vegetation in Artic Area," *Proceedings of PolinSAR 2015 Workshop*, ESA-ESRIN, Frascati, Italy, January 26-30, 2015.

4. L. Mascolo, J. M. Lopez-Sanchez, F. Vicente-Guijalba, G. Mazzarella, F. Nunziata, M. Migliaccio, "On the Sensitivity of Polarimetric SAR Observables to Phenological Stages of Crops in Barrax, Spain: First Results at C-Band," *Proceedings of the IEEE G.O.L.D. Remote Sensing Conference 2014*, Berlin, Germany, June 5-6, 2014.

5. L. Mascolo, F. Nunziata, A. Fanti, G. Mazzarella, M. Migliaccio, "On the Incoherent COSMO-SkyMed PingPong Mode to Distinguish Among Sea, Vegetated and Urban Scenarios," *Proceedings of the IEEE G.O.L.D. Remote Sensing Conference 2014*, Berlin, Germany, June 5-6, 2014.

6. L. Mascolo, M. Sarti, F. Nunziata, M. Migliaccio, "Vesuvius National Park Monitoring By Cosmo-SkyMed PingPong Data Analysis," *Proceedings of PolinSAR 2013 Workshop*, ESA-ESRIN, Frascati, Italy, January 28-February 1, 2013.

7. M. Sarti, L. Mascolo, "An Investigation of Different Polarimetric Decomposition Techniques for Soil Moisture Estimation," *Proceedings of the IEEE Tyrrhenian Workshop 2012 on Advances in Radar and Remote Sensing*, Naples, Italy, September 12-14, 2012.

8. A. Montuori, M. Migliaccio, F. Nunziata, L. Mascolo, "Wind Speed Estimation in the Tyrrhenian Sea by means of X-band COSMO-SkyMed SAR Data," *Proceedings of the IEEE Tyrrhenian Workshop 2012 on Advances in Radar and Remote Sensing*, Naples, Italy, September 12-14, 2012.

9. L. Mascolo, M. Sarti, M. Migliaccio, "On The Polarimetric Decomposition for Soil Moisture Estimation," *Proceedings of the IEEE G.O.L.D. Remote Sensing Conference 2012*, Rome, Italy, June 4-5, 2012.